Performance and Improvements of the Double Chooz Inner Muon Vetos

Dissertation

der Mathematisch-Naturwissenschaftlichen Fakultät
der Eberhard Karls Universität Tübingen
zur Erlangung des Grades eines Doktors
der Naturwissenschaften
(Dr. rer. nat.)

vorgelegt von
Dipl. Phys. Markus Röhling
geboren in Ostercappeln

Tübingen
2014

Tag der mündlichen Qualifikation:	30. 1. 2015
Dekan:	Prof. Dr. Wolfgang Rosenstiel
1. Berichterstatter:	Prof. Dr. Tobias Lachenmaier
2. Berichterstatter:	Prof. Dr. Josef Jochum

Zusammenfassung — deutsch
Double Chooz ist ein Neutrinoexperiment, das das Ziel hat den Neutrinomischungswinkel θ_{13} mit hoher Präzision zu vermessen. Dazu ist eine genaue Kenntnis des Untergrundes notwendig, insbesondere der durch kosmische Myonen erzeugte. Zu diesem Zweck besitzen die Double Chooz-Detektoren ein aktives Myonenveto, gefüllt mit Flüssigszintillator und bestückt mit 78 PMTs. Dieses Veto wurde von der Universität Tübingen entworfen und aufgebaut.
In dieser Arbeit wird das Ladungsspektrum des fernen Detektors, der seit 2011 Daten nimmt, untersucht und mit Monte Carlo Simulationen verglichen. Die totale Ereignisrate im Veto wird berechnet und die Dunkelrate der verbauten PMTs bestimmt und Messungen in Tübingen gegenüber gestellt. Ferner werden Monte Carlo Simulationen präsentiert, die durchgeführt wurden, um mögliche Verbesserungen für den nahen Detektor zu prüfen. Als Resultat wurde dieser mit mehr hochreflektierender Folie VM 2000 bestückt als im fernen Detektor. Der Aufbau fand in den Jahren 2013 und 2014 statt, die dafür notwendigen Vorbereitungen und die Installation werden hier vorgestellt.
In einer weiteren Studie werden die rekonstruierten Myonenwinkelverteilungen von zwei unabhängigen Algorithmen mit Simulationen verglichen und aufgezeigt, dass die Myonen vornehmlich aus der Richtung kommen, in der sich am wenigsten Abschirmung befindet. Ebenso wird untersucht in welchem Zeitfenster Myonen Ereignisse erzeugen, die dem Neutrinosignal ähneln und deshalb von der Auswertung ausgeschlossen werden müssen. Die Stabilität der Szintillatoren wird betrachtet und mögliche Einflüsse auf diese vorgestellt. Zuletzt wird eine Monte Carlo Studie für das JUNO Experiment präsentiert, ein sich im Aufbau befindliches Neutrinoexperiment, in der die Wasserschilddicke in Bezug auf die Eindringtiefe von myoninduzierten Neutronen untersucht wird.

Contents

Introduction

Double Chooz is a reactor neutrino experiment, which aims to measure the neutrino mixing angle θ_{13} with high precision. Therefore a good knowledge of all background processes is mandatory. For this purpose the Double Chooz detectors are equipped with an active liquid scintillator based muon veto system, the Inner Veto. This veto was designed and installed by the University of Tübingen.
This thesis will begin with a short introduction to the physical aspects of the neutrino oscillations. In the following chapter several reactor neutrino experiments will be presented with the focus on the Double Chooz experiment. The Inner Veto will be discussed in the chapter IV. Results of Monte Carlo simulation testing possible improvements for the near detector will be shown as well. In chapter V the charge spectrum of the Inner Veto of the far detector will be compared to Monte Carlo simulations. The total event rate will be determine and be contrasted with the estimation of dark noise of the used PMTs and radioactive impurities.
The azimuth and polar angle distributions of muons reconstructed by two individual algorithms will be compared to Monte Carlo simulation in chapter VI. In the following chapter VII the time distribution of muon classified events before neutrino candidates will be analysed and a new veto time window after muons presented.
In chapter VIII the time stability of scintillators in the far detector will be investigate and possible influences to it tested. At the end in chapter IX the reactor neutrino experiment JUNO will be presented and the results of a performed Monte Carlo simulation shown in which the dimensions of the JUNO-water shielding was varied to minimise the amount of muon induced neutron captures in the target region.

II

Physical Aspects

In this chapter the physical aspects necessary for this thesis will be discussed. First a short introduction to the Standard Model of Particle Physics will be given and then the focus will be moved to neutrino physics and the weak interaction. Finally some aspects of cosmic rays and their accompanying cosmic muons will be presented.

1 The Standard Model

The Standard Model (**SM**) is a compilation of physical theories to describe the smallest detectable particles of nature and their interactions. It is predicting three sectors of particles: Two of them, the quarks and leptons[1] are fermions. The third sector are the gauge bosons, which are transmitting forces.
The hadronic sector consists of doublets of quarks - particles, which can interact via all four known forces, namely strong, weak, electromagnetic and gravitational interaction. These two types of quarks are only separated by their electrical charge - one with $+\frac{2}{3}$ of the elementary charge, the other with $-\frac{1}{3}$. In total three doublets exist. In addition quarks carry colour, which can be red, green and blue or the respective anti-colour. Due to experimental evidences the SM requests that every free particle is colourless, what leads to the restriction that free quarks can not exist on their own, but have to be bound to other quarks. Either two quarks of colour and the same anti-colour form a so called meson, like a pion π^+, π^- or π^0, or three quarks with different colours are combined in a baryon, like proton or neutron.
The second sector, the leptons, consists of doublets as well: One of these is negative elec-

[1] From Greek $\alpha\delta\rho o\sigma$ "stout, thick" and $\lambda\epsilon\pi\tau o\sigma$ "thin, small" as the hadrons are in most cases heavier than the leptons.

trical charged and carries a mass, the other, the neutrino, is neutral and, at least in the original Standard Model, massless. The observation of neutrino oscillations leads to the conclusion that neutrinos must have a mass (see section 2.2). The heavy charged leptons can react via electromagnetic, weak and gravitational interactions, while the neutrino only interacts weakly and gravitationally.
In these two sectors, each with two particles, three generations or flavours exist. Hereby the massive charged leptons, electron, muon and tau, have the same properties except for the value of their mass.
The third sector consists of a group of bosons, which are the carrier of the fundamental forces. These are eight gluons for the strong interaction, the W^+, W^-, and Z^0 bosons for the weak interaction and the γ for the electromagnetic interaction.
In figure II.1 a graphical overview of the elementary particles of the Standard Model is given.

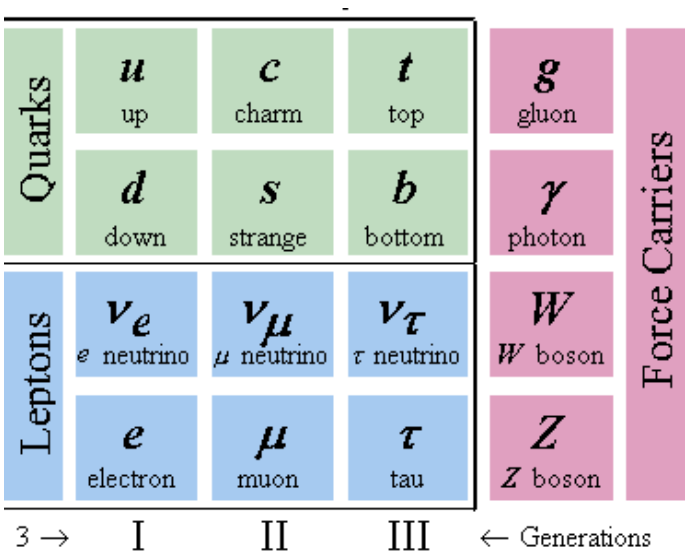

Figure II.1: The elementary particles of the Standard Model of Particle Physics. On the top left the six types of quarks, on the lower left the six leptons and on the right the gauge bosons are shown[D0]

1.1 Weak Interaction

As this work focuses on a neutrino experiment a view into the principles of the weak interaction is necessary. The name weak interaction derives from its relative small cross section due to the high masses of the exchange bosons, which corresponds to a short range of interaction.

The weak interaction takes place via the exchange of one of three particles. An exchange of the charged W^+ and W^- is called charged current, while an exchange of the uncharged Z^0 is named neutral current. Emitting a W-boson, a particle can transform into another, for example in the classical β^--decay of a neutron. Here a d-quark of the neutron emits a W^- and changes into an u-quark and therefore the neutron converts into a proton.
The weak force is described by the so called GSW[2] theory. This theory unifies the electromagnetic and the weak interaction to the electroweak interaction. Both interactions result out of the electroweak theory by spontaneous symmetry breaking at lower energies than immediately after the big bang. It requests four gauge bosons, the massless γ and the massive $W^\pm$ and Z^0, from whom at the first publication of the theory only the γ was known. The $W^\pm$ bosons have a mass of 80 GeV, the Z^0 of 91 GeV.
Because the GSW theory as a gauge theory requires massless gauge bosons, a scalar field is introduced, the so called Higgs[3] Field. This field has the property that an interaction of a particle with it leads to the mass of that particle. The field and the accompanying Higgs particle were long time only a prediction, but in 2012 experiments at the Large Hadron Collider (**LHC**) in Geneva found evidences for their existence[Atl12, CMS12].

1.1.1 CKM-Matrix

In the quark sector charged current transitions mostly happen in the same family, but there is a nonzero probability that the particle changes into another family. In the CKM-Matrix[4] these probabilities are mathematically described as[PDG12]

$$V_{CKM} = \begin{pmatrix} V_{ud} & V_{us} & V_{ub} \\ V_{cd} & V_{cs} & V_{cb} \\ V_{td} & V_{ts} & V_{tb} \end{pmatrix} \approx \begin{pmatrix} 0.974 & 0.225 & 0.004 \\ 0.225 & 0.973 & 0.04 \\ 0.009 & 0.04 & 0.999 \end{pmatrix}.$$

The element V_{ud} is related to the probability, that an u-quark changes into a d-quark.If the CKM-Matrix was an identity matrix, transitions between the families would not occur and all quarks would be stable.
Due to the small values of the non-diagonal elements of the matrix, a transition between the families is suppressed. Therefore the lightest quarks of the heavier families, the s and the b quark, have a longer lifetime than expected from their mass only.
There is a corresponding matrix for the leptons, the PMNS matrix, which will be described in detail in section 2.2.2.

[2]Named after its developers Sheldon Lee Glashow, *1932, Abdus Salam, 1926-1996, and Steven Weinberg, *1932, who received the Nobel Prize for their work in 1979.
[3]Peter Higgs, *1929, British physicist, received the Nobel Prize in 2013.
[4]Named after Nicola Cabbibo, 1935-2010, Makoto Kobayashi, *1944 and Toshihide Maskawa, *1940, from whom the last two received the Nobel Prize in 2008.

2 Neutrinos

Neutrinos are neutral particles and belong to the leptons. They are the doublet partner to the electron-like particles e, μ and τ. As in the hadronic sector the leptons can be grouped in three families.

2.1 Historical aspects

Neutrinos were first postulated by Wolfgang Pauli[5] in 1930 in his famous letter to the 'Gauvereinstagung' in Tübingen[Pau77]. He introduced a neutral particle to explain the continuous β^--decay spectrum in order to preserve the energy conservation.
Two years later, a neutral particle was found, today known as neutron, but very soon it was obvious, that this particle could not be the particle postulated by Pauli. Enrico Fermi[6] named the Pauli-particle *neutrino*, Italian for *little neutron*.
After the discovery of the nuclear fission and the installation of nuclear power plants, bigger neutrino sources were available as $\bar{\nu}_e$ are emitted in the *beta*-decay of neutron-rich fission isotopes. In 1953, more than twenty years after the postulation, Cowan and Reines[7] could experimentally prove the existence of neutrinos[Cow56].
Experimental evidence for a second neutrino family, today known as muon neutrinos, was given by Steinberger, Schwartz and Lederman[8] in 1962. After the discovery of the τ in 1975, the existence of the ν_τ was expected, but it took until 1997 when the DONUT[9] experiment was able to detect it[Don00].
Experiments were done to look for a forth neutrino family. With the Large Electron Positron collider (**LEP**) the decay of the Z^0 was studied very precisely. The partial decay widths into quarks ($\Gamma_{q\bar{q}}$) and charged leptons ($\Gamma_{l\bar{l}}$) can be subtracted from the the total measured decay width of the Z^0 (Γ_Z). It remains the decay width into neutrinos $\Gamma_{\nu\bar{\nu}}$.

$$\Gamma_Z = \Gamma_{l\bar{l}} + \Gamma_{q\bar{q}} + \Gamma_{\nu\bar{\nu}}$$

In figure II.2 the result is shown with the comparison to the decay width expectation for two, three and four neutrino generations.
The curve for three neutrino generations matches the data best. LEP can exclude the existence of more light active generations than the three known ones. If more neutrinos exist, they must be either sterile or heavier than the half of the Z^0 mass[LEP05].

[5] Wolfgang Pauli, 1900-1958, Austrian physicist, received the Nobel Prize in 1945.
[6] Enrico Fermi, 1901-1954, Italian physicist, received the Nobel Prize in 1938.
[7] Clyde Cowan, 1919-1974, and Frederick Reines, 1918-1998, US-American physicists, from whom the latter received the Nobel Prize in 1995.
[8] Jack Steinberger, *1921, Melvin Schwartz, 1932-2006, Leon Max Lederman, *1922, US-American physicists, received the Nobel Prize in 1988.
[9] **D**irect **O**bservation of the **NU** **T**au, former neutrino experiment in the USA.

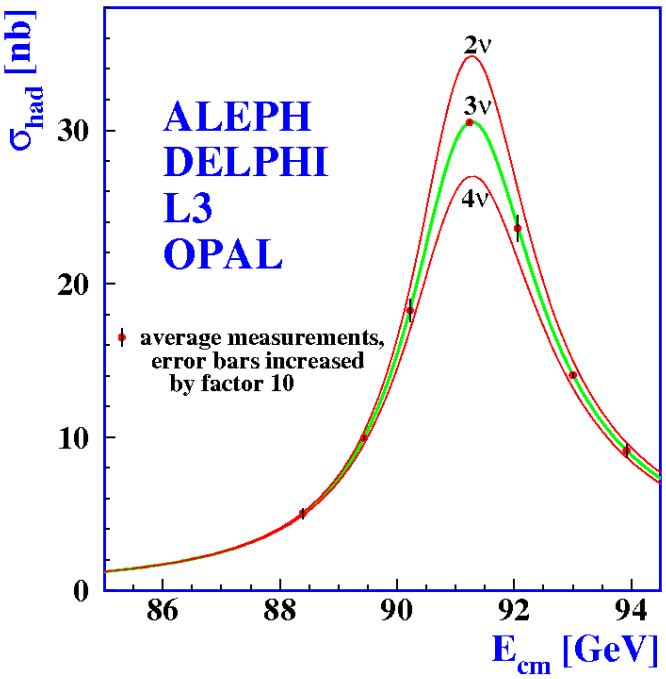

Figure II.2: Cross section of the Z^0 in hadrons measured with LEP. The expected cross sections for the assumption of two, three and four neutrino generations are plotted as well[LEP05].

2.2 Neutrino oscillations

Neutrino oscillations describe the transitions of neutrinos from one flavour into another. Their frequency depends on the energy of the neutrino and the distance between source and detection of the neutrino.

2.2.1 Experimental evidences

The first hints for neutrino oscillations occurred in the 1970s, when Raymond Davis Jr.[10] measured the flux of electron neutrinos emitted by the sun. He detected only roughly a third of what was expected by the Standard Solar Model, a model which describes the fusion processes in the sun and therefore the amount of emitted neutrinos. Later experiments like Gallex[11] and SAGE[12] could confirm this result. It was the SNO experiment[13], which was sensitive to all neutrino flavours (due to its energy threshold only for the neutrinos emitted in the ^{8}B-branch) and could proof the Standard Solar Model. The original ν_e were transformed into ν_μ and ν_τ.
For neutrinos, which were produced in the atmosphere by the decay of cosmic muons, the Super-Kamiokande[14] experiment could show, that an oscillation takes place there as well. As Super-Kamiokande is able to detect the direction of the neutrino, it could demonstrate, that there are less up going ν_μ than expected for the no-oscillation scenario[Sup98].
Also for reactor neutrinos an oscillation has been observed. The KamLAND experiment (see section 5 in chapter III) monitored the anti-neutrino flux of the surrounding reactors and measured less neutrinos than expected[Kam08].

2.2.2 Formal description

Neutrinos are produced and detected as weak eigenstates $|\nu_\alpha\rangle$ with $\alpha = e, \mu, \tau$. But their propagation happens as mass eigenstates $|\nu_i\rangle$ with $i = 1, 2, 3$. These two are connected via the matrix U:

$$|\nu_i\rangle = \sum_\alpha U_{\alpha i}|\nu_\alpha\rangle \qquad \text{respectively} \qquad |\nu_\alpha\rangle = \sum_i U^*_{\alpha i}|\nu_i\rangle.$$

The matrix $U_{\alpha i}$ is an unitary matrix, $U^*_{\alpha i}$ is its complex conjugated. If $U_{\alpha i}$ would be a diagonal matrix, each flavour had a specific mass and no neutrino oscillations were possible. Many experiments showed that this is not the case (see last section) and therefore each flavour state corresponds to a mixture of mass eigenstates.
The matrix $U_{\alpha i}$ is called the PMNS-matrix[15]. It is the analogon to the CKM-matrix

[10] Raymond Davis Junior, 1914-2006, US-American chemist, received the Nobel Prize in physics in 2002.
[11] **Gall**ium **Ex**periment, 1991 - 1997 in Italy.
[12] Soviet–American Gallium Experiment, 1990 - 2000 in Russia.
[13] **S**udbury **N**eutrino **O**bservatory, 1999 - 2006 in Canada.
[14] **Super Kamioka n**ucleon **d**ecay **e**xperiment, since 1996 in Japan.
[15] Named after Bruno Pontecorvo, 1913-1993, Italian physicist, Ziro Maki, Masami Nakagawa and Shoichi Sakata, 1911-1970, Japanese physicists.

(see 1.1.1) in the neutrino sector.
It contains six unknown parameters. It is possible to factorize the matrix into four matrices to separate these parameters:

$$\begin{aligned} U &= \begin{pmatrix} U_{e1} & U_{e2} & U_{e3} \\ U_{\mu 1} & U_{\mu 2} & U_{\mu 3} \\ U_{\tau 1} & U_{\tau 2} & U_{\tau 3} \end{pmatrix} \\ &= \begin{pmatrix} 1 & 0 & 0 \\ 0 & \cos(\theta_{23}) & \sin(\theta_{23}) \\ 0 & -\sin(\theta_{23}) & \cos(\theta_{23}) \end{pmatrix} \begin{pmatrix} \cos(\theta_{13}) & 0 & \sin(\theta_{13})e^{-i\delta} \\ 0 & 1 & 0 \\ -\sin(\theta_{13})e^{-i\delta} & 0 & \cos(\theta_{13}) \end{pmatrix} \\ &\quad \cdot \begin{pmatrix} \cos(\theta_{12}) & \sin(\theta_{12}) & 0 \\ -\sin(\theta_{12}) & \cos(\theta_{12}) & 0 \\ 0 & 0 & 1 \end{pmatrix} \begin{pmatrix} 1 & 0 & 0 \\ 0 & e^{i\alpha} & 0 \\ 0 & 0 & e^{i\beta} \end{pmatrix} \end{aligned}$$

θ_{ij} are rotation angles, often called mixing angles. The phase factor δ stands for a possible CP violation in the neutrino oscillations. A CP violation can only exist if all the mixing angles are non-zero.
The last matrix is only relevant if the neutrinos are Majorana[16] particles, so they would be their own anti particles. This characteristic of the neutrinos is currently under investigation. If neutrinos are Dirac[17] particles instead, α and β are zero and the matrix becomes an identity matrix.
The propagation of mass eigenstates can be written in natural units as the propagation of a plain wave as:

$$|\nu_i(t)\rangle = e^{-iE_i t}|\nu_i\rangle,$$

where E_i is the energy of the mass eigenstate i.
As the mass of the neutrinos is mostly much smaller than its momentum, so $p \gg m_i$ the following approximation can be made:

$$E_i = \sqrt{p^2 + m_i^2} \simeq p + \frac{m_i^2}{2p} \approx E + \frac{m_i^2}{2E},$$

with $E \simeq p$ as neutrino energy. A pure flavour state $|\nu_\alpha\rangle = \sum_i U_{\alpha i}|\nu_i\rangle$ at $t = 0$ will evolve with t to

$$|\nu(t)\rangle = \sum_i U_{\alpha i} e^{-iE_i t}|\nu_i\rangle = \sum_{i,t} U_{\alpha i} U^*_{\beta i} e^{-iE_i t}|\nu_\beta\rangle$$

The probability P, that ν_α becomes ν_β after the time t with $\alpha, \beta = e, \mu, \tau$, is therefore

$$P_{\alpha\to\beta} = |\langle\nu_\beta|\nu(t)\rangle|^2 = |\sum_i U^*_{\beta i} U_{\alpha i} e^{-iE_i t}|^2.$$

[16] Ettore Majorana, 1906 - presumed dead in 1938, Italian physicist.
[17] Paul Dirac, 1902 - 1984 British physicist, received the Nobel Prize in 1933.

This can be expanded to

$$\begin{aligned} P_{\alpha\to\beta} &= \sum_{i,j} U_{\alpha i}U^*_{\alpha j}U^*_{\beta i}U_{\beta j}e^{-i(E_i-E_j)t} \\ &= \sum_i |U_{\alpha i}U^*_{\beta i}|^2 + 2\Re\sum_{j>i} U_{\alpha i}U^*_{\alpha j}U^*_{\beta i}U_{\beta j}e^{-i\Delta_{ij}} \end{aligned}$$

with

$$\Delta_{ij} = (E_i - E_j)t = \frac{\Delta m^2_{ij}}{2}\cdot\frac{L}{E} \text{ and } \Delta m^2_{ij} = m^2_i - m^2_j.$$

Ignoring a possible CP violation, which means all $U_{\alpha i}$ are real, the equation can be written as

$$\begin{aligned} P_{\alpha\to\beta} &= \sum_i U^2_{\alpha i}U^2_{\beta i} + 2\sum_{j>i} U_{\alpha i}U_{\alpha j}U_{\beta i}U_{\beta j}\cos\left(\frac{\Delta m^2_{ij}}{2}\frac{L}{E}\right) \\ &= \delta_{\alpha\beta} - 4\sum_{j>i} U_{\alpha i}U_{\alpha j}U_{\beta i}U_{\beta j}\sin^2\left(\frac{\Delta m^2_{ij}}{4}\frac{L}{E}\right). \end{aligned} \tag{II.1}$$

From equation II.1 it is visible that at least two of the mass eigenstates have to be non-zero as otherwise the Δm_{ij} would be zero and no oscillations were possible[Sch97, Zub12].

2.3 Mass hierarchy

The mass difference Δm^2_{21} was first measured by the solar neutrino oscillations experiments and is therefore known as Δm^2_{sol}. These experiments could show as well that the mass eigenstate with the highest ν_e content m_1 is lighter than m_2.
Experiments, which study neutrinos from the atmosphere, demonstrated, that $\Delta m^2_{atm} := \Delta m^2_{32}$ is higher than Δm^2_{sol} by a factor of 30. As these experiments are only sensitive to the absolute value of Δm^2_{atm}, the obtained relation is $|\Delta m^2_{atm}| > |\Delta m^2_{sol}|$.
This leads to the neutrino mass hierarchy question: It is not known whether the neutrino masses have a normal hierarchy, so $m_3 > m_2 > m_1$ or an inverted hierarchy, which means $m_2 > m_1 > m_3$ (see figure II.3)[Cah13].
To solve this hierarchy problem many experiments are proposed. The JUNO experiment, which is described in chapter IX, is one of these. Proposed extensions of currently running or under construction neutrino experiments like PINGU for IceCube[18] and ORCA for KM3NeT[19] can also help to solve the neutrino mass hierarchy question.

3 Cosmic rays

The earth is under a permanent bombardment of particles from outer space. These particles are mostly protons and have a broad energy distribution, beginning with a few MeV

[18]Neutrino experiment, 2010 - , located at the south pole
[19]Planned neutrino experiment, located in the Mediterranean Sea

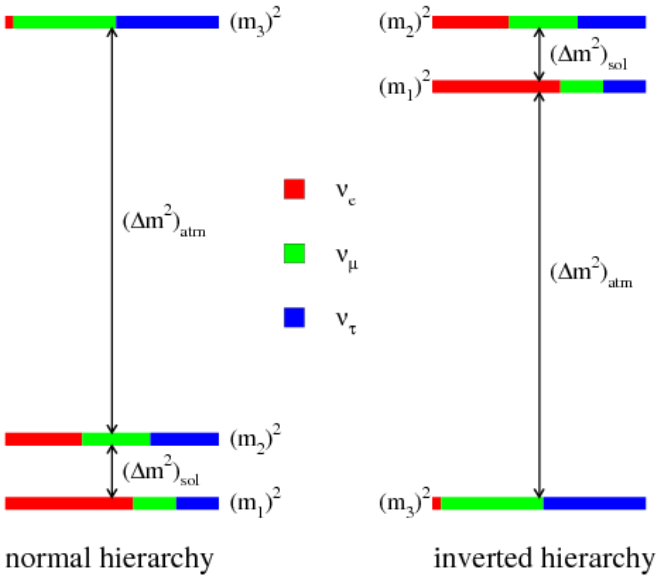

Figure II.3: Shown are the two possible neutrino mass hierarchies. The colours symbolize the amount of e, μ and τ in the different mass eigenstates[Cah13]

.

up to particles with 10^{20} MeV. Their flux follows a power law with 100 particles per cm^2 and second for the lower energies and ends with one particle per km^2 and century for the highest energies. For the lower energies the majority of particles is coming from our sun, while for the end of the spectrum sources are still unknown, there are only assumptions for them.

The particles arriving at the earth's atmosphere are called primary cosmic rays. While they are travelling through the atmosphere they will interact with the atoms in it. Hereby they lose parts of their energy and produce new particles. These are mostly unstable and decay into other particles. A particle shower occurs, which normally stops, when the particles have not enough energy to generate new particles. All particles generated that way are the so called secondary cosmic rays.

In most of the showers muons are generated. Muons have the characteristic, that they have a relative long life time. As they have mostly an ultra-relativistic velocity, they can reach the earth surface due to the relativistic time dilatation. They are the major part of the cosmic rays on ground.

Like the primary cosmic rays the energy spectrum of the muons on ground is broad. The mean energy is ≈ 4 GeV. For energies below 1 GeV the spectrum is almost flat and then drops very steeply like the primary cosmic rays.

The muon angular distribution of the polar angle θ goes almost with $\cos^2(\theta)$, so that the majority of them comes from zenith. The azimuth angle φ is uniformly distributed[PDG12].

4 Neutrons

The neutron is a baryon and consists of three quarks: two d and one u-quark. As the name implies it is electrical neutral. It has almost the same mass as a proton. If it is not bound in an atomic nucleus, it is unstable and decays into a proton via the emission of an electron and an anti-electron-neutrino with a mean lifetime of 880 s.
Due to its missing charge it does not interact via the electromagnetic interaction. Therefore it is impossible to guide them with electrical or magnetic fields. As they are hadrons they interact strongly with other particles or atomic nuclei.
Neutrons have a chance to be captured by an atomic nucleus and get integrated into it. This probability depends on the specific nuclei and the energy of the neutron. There is the general trend that the neutron capture probability increases with decreasing neutron energy. Some nuclei are exceptional as for small neutron energy bands the caption cross section is very high.

III

Reactor neutrino experiments

In this chapter the reactor neutrino experiments CHOOZ, KamLAND, Double Chooz, Reno and Daya Bay will be presented. The focus will lie on the Double Chooz experiment. First, a general motivation for reactor neutrino experiments will be given, then two important predecessors are presented. After a description of the Double Chooz experiment its competitors will be introduced.

1 Motivation for reactor neutrino experiments

Nuclear reactors are a very intense source of neutrinos. During the fission processes unstable isotopes are produced, which decay afterwards. In these decays neutrinos are emitted. Typical energies of reactor neutrinos are in a range of a few MeV. As the controlled fission is a delicate issue much research has been made and it seems to be well understood. Therefore it is possible to simulate precisely the emitted neutrino spectrum of a reactor with known fuel assembly and burn-up.
Due to these facts reactors are a very common source for neutrino experiments. Neutrinos were discovered by a reactor neutrino experiment by Cowan and Reines (see section 2.1 in chapter II). Nowadays they are used to study the effect of the neutrino oscillations. As it can be seen in the equations II.1 and III.1 and in figure III.1, the optimal distance from the neutrino source to the experiment depends on the particular Δm^2_{ij}, which will be investigated and the neutrino energy. Due to the energy range of reactor neutrinos of a few MeV, this distance corresponds to a few hundred meters for Δm^2_{31} up to hundred kilometres for Δm^2_{21}.

2 Neutrino detection principles

All of the reactor neutrino experiments presented in this section share the same neutrino detection method and general detector composition. As all reactor neutrinos are anti-electron neutrinos $\bar{\nu}_e$, they can interact with protons in the scintillators via the inverse beta decay (**IBD**)

$$\bar{\nu}_e + p \rightarrow n + e^+,$$

so a anti-neutrino produces a positron and a neutron. This process has a threshold energy of around 1.8 MeV, which consists of the mass difference between neutron and proton and the mass of the positron.
The positron will carry most of the remaining kinetic energy of the neutrino. It will lose it and annihilate quasi instantly. The neutron will thermalise and be captured. The time between positron annihilation and neutron capture and the released neutron capture energy are depending on the used scintillator and its components.
Thus an inverse beta decay will be noticeable by two signals with a certain mean delay between them: First the annihilation of the positron, which deposits the remaining kinetic energy of the original neutrino plus the annihilation energy. Second the capture energy of the neutron with a characteristic delay.
All experiments mentioned here are liquid scintillator[1] based, which are mostly made out of certain hydrocarbons. Scintillators have the property, that they emit optical photons, when particles deposit energy in them. As the scintillator are not transparent for the wavelength of their emitted light due to self-absorption, a wavelength shifter is added, which absorbs the photons and reemits them with a higher wavelength.
To detect this light photo multiplier tubes (**PMT**) are used. PMTs have a light sensitive area, the photo cathode, which absorbs incoming photons. With a wavelength specific probability, the quantum efficiency, an electron will be emitted, the photo electron (PE). With the help of applied high voltage an avalanche is generated, which results in an easily detectable current pulse.
Many experiments use Gadolinium-doped scintillator. Gadolinium is a chemical element of the lanthanide series, so a rare-earth. It has the characteristic, that it has a very high neutron capture cross section. The energy emitted in this process lies with roughly 8 MeV far above the background of natural radioactivity.

3 Oscillations of reactor neutrinos

The energy of the reactor neutrinos is too less to allow an appearance experiment ($\bar{\nu}_e \rightarrow \bar{\nu}_{\mu/\tau}$). Therefore only the survival probability of the anti-electron-neutrinos $P_{\bar{\nu}_e \rightarrow \bar{\nu}_e}$ can be studied. The general probability $P_{\alpha \rightarrow \beta}$, that a neutrino with the energy E and the flavour α can be detected after a distance L with the flavour β was descried in equation II.1.

[1] Latin *scintillare* - to sparkle, to flicker

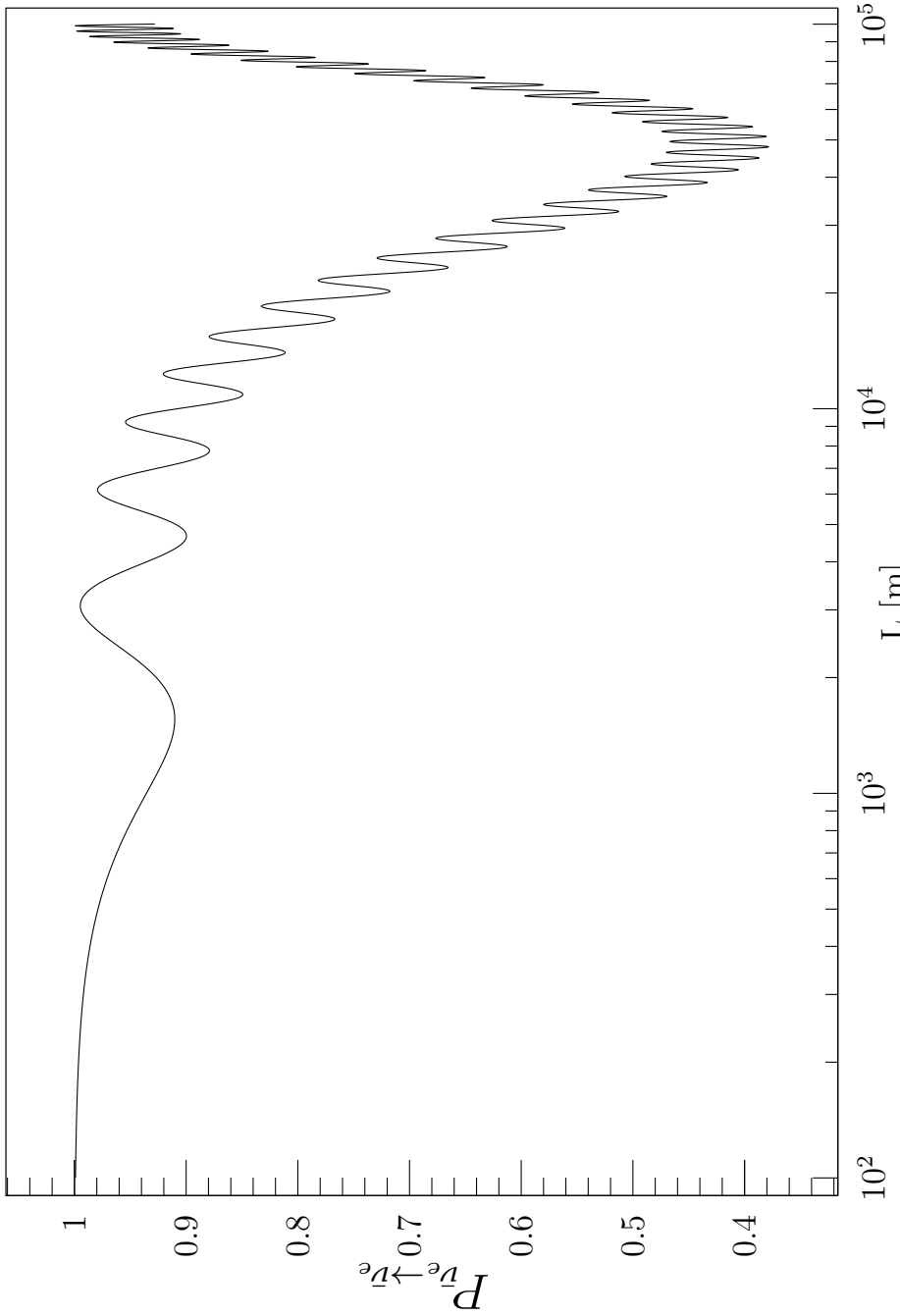

Figure III.1: Reactor neutrino oscillations for neutrinos with $E = 3\,\mathrm{MeV}$, the used values $\theta_{13} = 8.7^\circ$, $\theta_{12} = 24.2^\circ$ $\Delta m^2_{31} = 2.4 \cdot 10^{-3}\,\mathrm{eV}^2$ and $\Delta m^2_{21} = 7,58 \cdot 10^{-5}\,\mathrm{eV}^2$ were taken from [DCC14] and [Kam08].

Following this equation the probability can be written as

$$\begin{aligned} P_{\bar{\nu}_e \to \bar{\nu}_e} &= 1 \quad - \cos^2(\theta_{12}) \sin^2(2\theta_{13}) \cos^2(\theta_{13}) \sin^2\left(\frac{\Delta m^2_{31} L}{4E}\right) \\ &\quad - \sin^2(\theta_{12}) \sin^2(2\theta_{13}) \cos^2(\theta_{13}) \sin^2\left(\frac{\Delta m^2_{32} L}{4E}\right) \\ &\quad - cos^4(\theta_{13}) \sin^2(2\theta_{12}) \sin^2\left(\frac{\Delta m^2_{21} L}{4E}\right) \end{aligned}$$

As $|\Delta m^2_{31}| \sim |\Delta m^2_{32}|$ (see section 2.3 in chapter II) the equation can be simplified to

$$\begin{aligned} P_{\bar{\nu}_e \to \bar{\nu}_e} &= 1 \quad - 2 \sin^2(2\theta_{13}) \sin^2\left(\frac{\Delta m^2_{31} L}{4E}\right) \\ &\quad - \cos^4(\theta_{13}) \sin^2(2\theta_{12}) \sin^2\left(\frac{\Delta m^2_{21} L}{4E}\right). \end{aligned} \tag{III.1}$$

Equation III.1 shows, that two terms account for the oscillations. For the first term the frequency depends on Δm_{31} and the amplitude on the sine of $2\theta_{13}$, while the second term depends on Δm_{21} and the sine of $2\theta_{12}$ for frequency and amplitude. Also visible is the fact, that for vanishing mixing angle θ_{13} the first oscillation disappears.
Figure III.1 shows the result of equation III.1 graphically for 3 MeV neutrinos and the results from [DCC14] and [Kam08]. The first oscillation has its first maximum at around one kilometre, while for the second oscillation the first maximum lies at around 50 km, but with a much higher amplitude.
Thus, experiments which want to study θ_{13} should be placed in a distance of around one kilometre away from a reactor, while experiments aiming for θ_{12} are well located around 50 km away from a reactor.

4 The CHOOZ experiment

CHOOZ was a former reactor neutrino experiment. It is the predecessor of the Double Chooz experiment and similar in its detector design. It was originally intended to investigate the results of the Super-Kamiokande experiment (see section 2.2.1 in chapter II). It was unclear whether the missing atmospheric neutrinos were oscillated into tauons or electrons. In the case of electrons the reverse reaction would occur for reactor neutrinos leading to large absence of electrons. This measurement was not successful, but a limit on θ_{13} could be set. The experiment was named after the village Chooz, which is located at the Meuse river in the French Ardennes near the border to Belgium. Nearby Chooz is a nuclear power station. It consists of two pressurized water reactors of the type N4 and is run by EDF[2]. These reactors (Chooz B1/B2) have 4.25 GW thermal power each and hence both an electric net performance of 1.5 GW. In the 1960s a smaller reactor (Chooz A) was

[2]Électricité de France, French power company

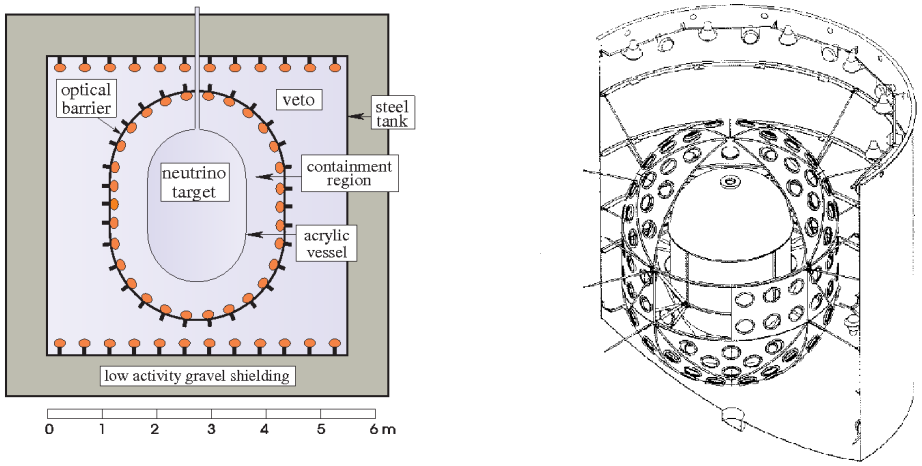

(a) (b)

Figure III.2: Two sketches the CHOOZ experiment. The left picture shows a schematic view of the detector with its volumes, while the right is a technical drawing of the steel vessel containing the scintillators embedded in the muon veto volume[Cho03].

used, which was installed in the surrounding hills, stopped in 1991 and dismantled. One hall of its supply tunnels was used as location for the CHOOZ experiment. This laboratory is around 1000 m away from both reactor cores and has an overburden of 300 m water equivalent(mwe).
The CHOOZ detector consisted of 5 tons of liquid scintillator. This scintillator was doped with a gadolinium complex. Around this doped scintillator an undoped scintillator of 17 tons mass was located. They were separated by a transparent acrylic container. The second, undoped scintillator had the purpose to detect gamma photons, which were produced in the capture process of the neutron on gadolinium and left the inner scintillator. 192 eight inch PMTs were installed on the walls of a steel vessel, which contained both scintillators. Around the vessel an active muon veto of 90 tons mass was built, equipped with 24 eight inch PMTs. This is contained in a steel tank as well. The tank was then surrounded by low radioactive gravel. Sketches of the detector can be seen in figure III.2.
The CHOOZ experiment took data from April 1997 to July 1998. It stopped data taking as the scintillator showed a degradation in its transparency resulting in a decrease of the photo electron yield. Additionally at this moment it became clear that both reactors would not run with full power for more than one year due to cooling problems. The Chooz collaboration found no evidence for neutrino oscillations in a kilometre distance and could set a limit on θ_{13} to [Cho03]

$$\sin^2(2\theta_{13}) < 0.10 \text{ (90 \% confidence level for large } \Delta m^2_{31} \ (> 2 \cdot 10^{-2}\,\mathrm{eV}^2)).$$

5 KamLAND

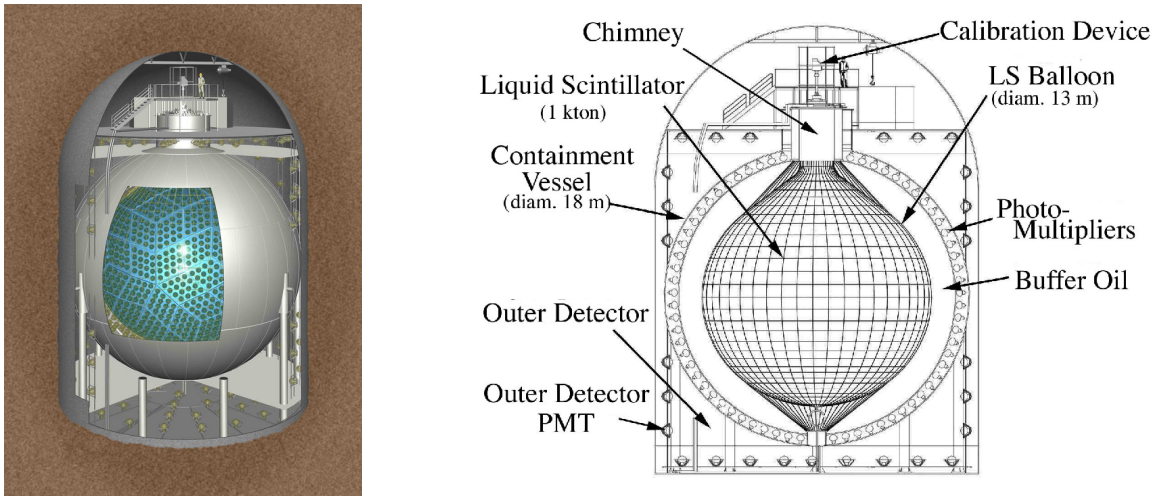

(a) Detector illustration[KamL] (b) Sketch of the detector components[Kam08]

Figure III.3: The KamLAND detector. The left picture is an illustration of the detector. The right picture shows the used components.

KamLAND stands for Kamioka Liquid scintillator Neutrino Detector. It was the first experiment that could prove neutrino oscillations in the reactor neutrino sector.
KamLAND is located in a mine in the Kamioka village in the Japanese Alps. It is installed in an old mine, where also the Kamiokande experiment was placed and the Super-Kamiokande experiment (see section 2.2.1 in chapter II) is located. The mine has an overburden of ∼2700 mwe.
The detector consists of 1 kton of liquid scintillator. This liquid is contained in a nylon balloon, which is surrounded by mineral oil. Both volumes are included in a stainless steel sphere, whose inner wall is equipped with 1879 PMTs with a photo cathode of 50 cm diameter. Around the sphere an outer detector filled with water is built, which is instrumented with PMTs as well and acts as a shielding and active muon veto. In figure III.3 the KamLAND detector is sketched.
The detector can detect neutrinos via the inverse beta decay as described in section 2. In KamLAND the neutrons are captured on hydrogen resulting in a emission of 2.2 MeV photons after a typical life time of 200 µs.
Around the experiment 55 Japanese nuclear reactors are located. They all provided their fuel composition and the current reactor power to the KamLAND collaboration[Kam08]. Based on this information and an estimation of the reactors used worldwide the neutrino flux at the experiment can be simulated.
In five years of measuring time 1609 neutrino like events were detected[Kam08]. In figure III.4 the energy and the L/E distribution of these events are plotted. The energy spectrum matches well with the oscillation expectation, while the non-oscillation case is

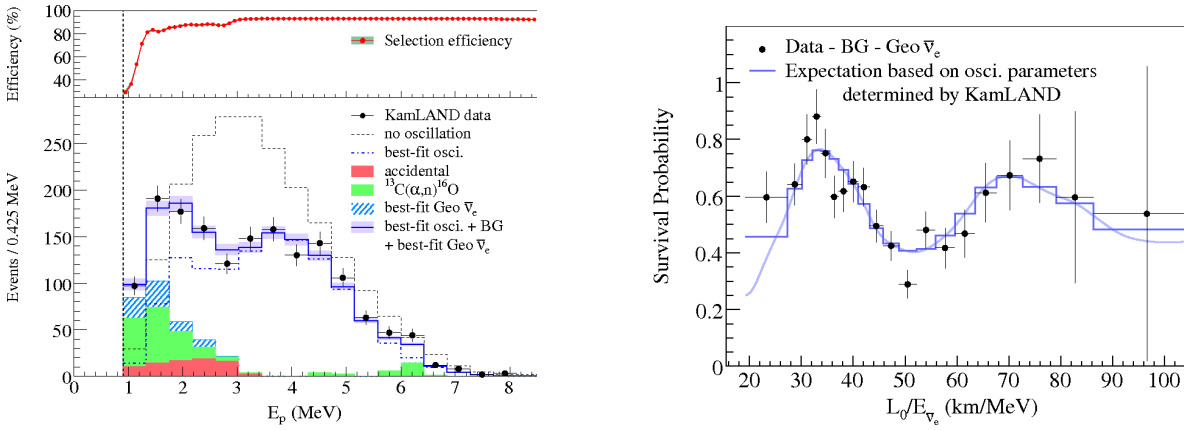

(a) Neutrino energy spectrum (b) Survival probability

Figure III.4: Neutrino energy spectrum and survival probability of the neutrinos measured by KamLAND. The energy spectrum shows an oscillating behaviour, whereas the unoscillated case is disfavoured. For the survival probability a flux-weighted average baseline L_0 was calculated. While for no-oscillation case the survival probability of the reactor neutrinos would be one, the data show an oscillation[Kam08].

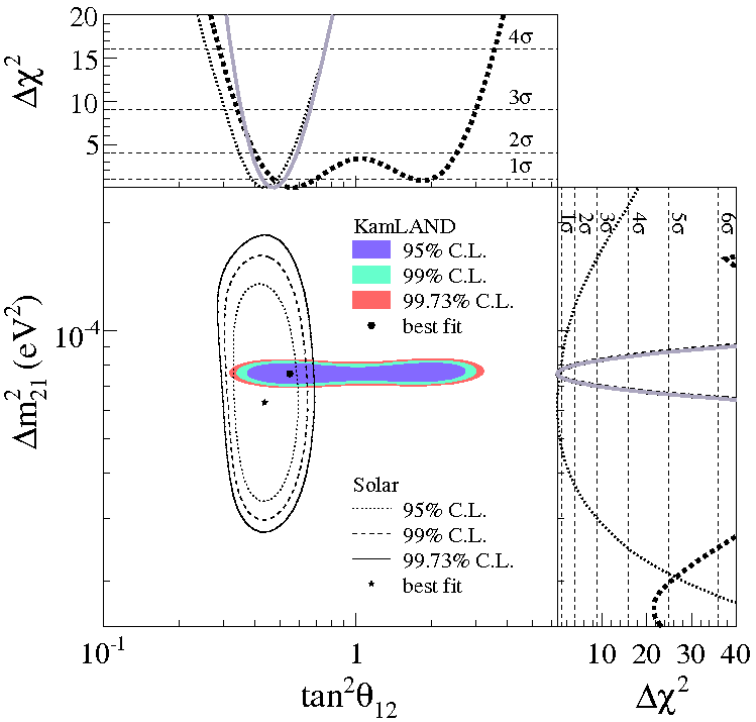

Figure III.5: Graphical combination of the KamLAND results with the ones of the solar neutrino experiments[Kam08].

disfavoured. Combining this spectrum with the reactor simulations an L_0/E distribution of the neutrinos can be made. L_0 is the flux-weighted average baseline ($\sim 180\,\mathrm{km}$). (See right plot of figure III.4). Here an oscillation behaviour of the spectrum is visible like it is expected (see figure III.1 for comparison).
A fit to the energy distribution yields values for θ_{12} and Δm^2_{12}. If these values are combined with the results of solar neutrino experiments like SNO (see see 2.2.1 in chapter II), the KamLAND experiment results in [Kam08]:

$$\Delta m^2_{12} = 7.58^{+0.14}_{-0.13}(\mathrm{stat})^{+0.15}_{-0.15}(\mathrm{syst}) \times 10^{-5}\,\mathrm{eV}^2 \quad \text{(III.2)}$$

$$\theta_{12} = 0.56^{+0.10}_{-0.07}(\mathrm{stat})^{+0.10}_{-0.06}(\mathrm{syst}) \quad \text{(III.3)}$$

This also shown graphically in figure III.5.
Many other experiments measured the flux of reactor neutrinos before CHOOZ and KamLAND. Their results are plotted in figure III.6. Additionally the current flux calculation is shown in red. It is noticeable that almost all experiments measured a reactor rate below this calculation. To explain this a sterile neutrino can be postulated. The blue line shows a corresponding reactor neutrino flux. Details on sterile neutrinos can be found in [Aba12] and will not be discussed further in this work.

6 The Double Chooz experiment

Double Chooz is a reactor neutrino experiment, which is run by an international collaboration with institutes from six nations. It is the successor of the CHOOZ experiment and reuses the old laboratory of the CHOOZ experiment, where a new detector was installed. Additionally a second detector belongs to the experiment, therefore it is named Double Chooz. The two detectors have different distances to the two reactor cores of the nuclear power plant in Chooz: The far detector (**FD**) in the old CHOOZ laboratory is on average 1050 m away from the reactors with an overburden of 300 mwe. It is called the far detector (**FD**). The near detector (**ND**) has an average distance to the two reactors of 400 m. Its overburden is 150 mwe. The far detector is taking data since April 2011 - the near detector is currently in the commissioning phase and will start data taking at the end of the year 2014.

6.1 Motivation and detection principles

When Double Chooz was planned, θ_{13} was the last unknown neutrino mixing angle, only an upper limit on its value was existing. The most precise value came from the precursor of Double Chooz, the CHOOZ experiment (see section 4). A precise knowledge of θ_{13} is necessary for the further investigation of a possible CP-violation in the neutrino sector, because a vanishing or very small θ_{13} will make a CP-violation measurement very challenging or impossible (see section 2.2.2 in chapter II).
As it can be seen in figure III.1 an optimal position to measure the mixing angle θ_{13} is roughly a kilometre away from a reactor. This is exactly the distance from the old CHOOZ

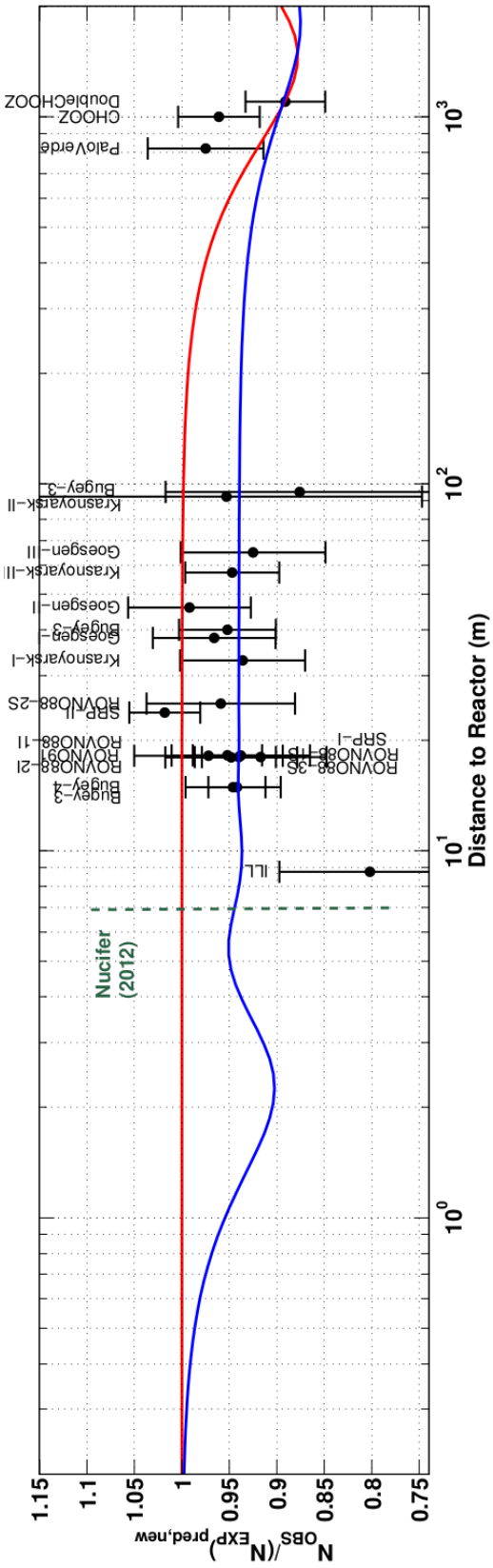

Figure III.6: Results of reactor neutrino experiments. The red line shows the calculated reactor neutrino flux from [Mül11], while the blue line is the reactor neutrino flux minus the possible oscillation in sterile neutrinos[Aba12].

laboratory to the Chooz reactors. To have a precise knowledge of the neutrino flux a second detector is needed. If this detector is identical to the first one, all possible detector effects will cancel out each other. Thus the systematic error on the normalization between the detectors can be reduced by a factor of three from 1.5 % for the CHOOZ experiment to 0.5 %. Placed near the reactors, the near detector will measure the neutrino flux without oscillation effects. The difference in the amount of detected neutrinos in both detectors is, beside the decrease due to the longer distance for the far detector, directly dependent from the oscillation.
Double Chooz uses liquid scintillator as target material and detects neutrinos via the inverse beta decay. The scintillator is doped with gadolinium. To solve it in scintillators it has to be chemically bound in a complex. Gadolinium complexes are unstable in contact with scintillators and the scintillator can get less transparent like it happened in the CHOOZ experiment. It was one of the major efforts for the Double Chooz experiment to develop a gadolinium complex, which is stable for years in liquid scintillators.

6.1.1 Backgrounds

For a precise measurement of θ_{13} a knowledge of all background processes on sub-percent level is necessary. Therefore much effort is spent to understand them.
Although the neutrino detection principle with two correlated events in a certain energy band eliminates the majority of background, it does not prevent all. It is possible to separate these in two types: correlated and uncorrelated background.

6.1.1.1 Uncorrelated background If two uncorrelated events with particular energies occur by chance in the time interval Δt used in the neutrino search, they are indistinguishable from a neutrino. A typical example is the consideration of a radioactive decay with the emission of a gamma or an electron of a few MeV and a capture of neutron, which penetrated into the detector. The rate of uncorrelated background R_{ub} can be estimated with the known rate of single events in the detector R_S and the rate of neutrons R_n in the central detector by $R_{ub} = R_S \cdot R_n \cdot \Delta t$.

6.1.1.2 Correlated background There are physical processes which can mimic an inverse beta decay. A high energetic neutron, for example, produced in the detector surrounding by an unseen muon can deposit several MeV in the detector and gets captured afterwards.
Due to spallation of carbon atoms by muons radioisotopes can be produced. Some of them can decay by neutron emission, and have additionally lifetimes in the dimension of 100 ms. thus a veto after each muon results in a infinite dead time. ^{9}Li and ^{8}He show this behaviour. ^{9}Li decays in around 50 % with $^9\mathrm{Li} \rightarrow {}^8\mathrm{Be} + e^- + n$. The emitted electron has an endpoint energy of 13 MeV, so it lies in a very similar energy interval as the positrons produced in inverse beta decays.
Muons which enter the ID unseen through the chimney and decay in the upper part of the Gamma Catcher are a dangerous background as well.

6.2 The two detectors

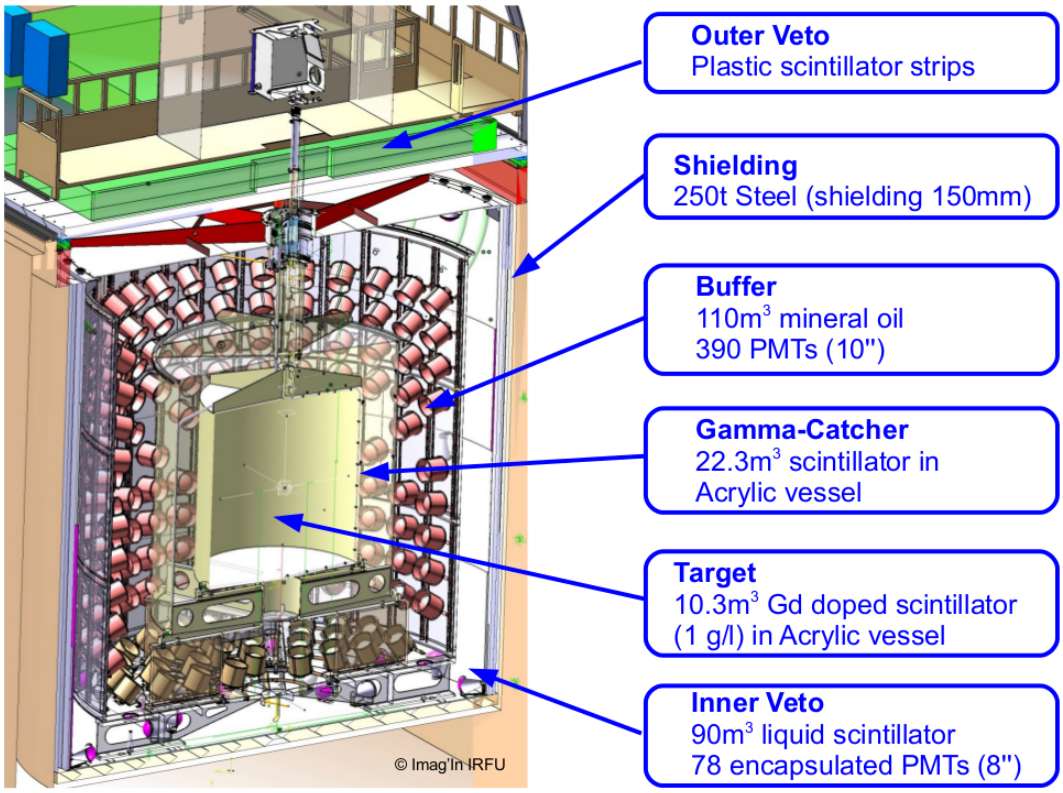

Figure III.7: Schematic overview of the Double Chooz detectors[Die12].

The two Double Chooz detectors are almost identical and differ only in very few details. They are installed in a pit in laboratories. In figure III.7 the far detector is sketched. This section will give an overview on the detector, beginning with the innermost volume going to the outside step by step.

6.2.1 Inner Detector

The central part of the detector is called the Inner Detector (**ID**). It consists of three sub-volumes: The neutrino target, the gamma-catcher and the buffer.
The innermost region is the neutrino target. It has a volume of 10.3 m^3 and is filled with a gadolinium-doped scintillator. It is contained in an acrylic vessel. The used acrylic has the property, that it is transparent for optical and UV-light. Around the target the so-called gamma-catcher is located. It has a volume of 22.3 m^3 and is filled with undoped liquid scintillator. Its main purpose is to detect gamma photons, which are produced near the walls of the target and leave it undetected. The gamma-catcher is contained in an acrylic vessel as well. Both volumes are surrounded by the buffer. Its 110 m^3 volume is filled with mineral oil. It is contained in a stainless steel vessel, whose inner walls are covered by 390 PMTs. The PMTs are of 10 inch diameter and from the type R7081 produced by

Hamamatsu. Each PMT is individually aligned to look into the centre of the detector. The main function of the buffer is to shield the target and the gamma-catcher from radioactivity coming from the PMTs and from outside of the detector.
All volumes have a chimney. These chimneys are installed in the middle on top of the volumes and connect the volumes with the outside. They are nested and form one big chimney. They are necessary for filling the volumes and to insert calibration sources.

6.2.2 Muon Veto systems

Two active systems are installed to identify passing muons very efficiently: The Inner Veto, which surrounds the Inner Detector and the Outer Veto on top of the detector.

6.2.2.1 Inner Veto Optical separated from the ID the Inner Veto (**IV**) surrounds the buffer vessel. It has a volume of 90 m^3 and is filled with liquid scintillator. It is contained in a vessel, which is made out of steel for the far detector and of stainless steel for the near detector. On the inner walls of this vessel 78 PMTs of 8 inch diameter are installed. For a higher reflectivity and photo detection efficiency the walls of the buffer vessel are covered with the high reflective foil VM 2000 made by 3M. For the same reason the inner IV-vessel wall is painted with a high reflective white paint in case of the far detector and also covered with VM 2000 for the near detector.
Besides the tagging of passing muons, it is another shielding for outside radioactivity and is able to detect incoming neutrons, produced in spallation by nearby passing muons trough the surrounding rocks. The IV has a chimney as well. For more details on the Inner Veto see chapter IV.
The Inner Veto is surrounded by a shielding, which consists of 15 cm steel for the far detector and one meter of water for the near detector.

6.2.2.2 Outer Veto On top of the detector four layers of modules of plastic scintillator stripes are installed, the so-called Outer Veto (**OV**). The modules consist of several stripes which are equipped with a PMT, which can be readout individually. The layers are rotated in 90 ° to the upper/lower to allow an x-y reconstruction.
The Outer Veto has the dimension of 13 x 7 m^2 above the pit, in which the detector is installed. A hole has to be left for the chimneys. These are connected to a glove box for inserting calibration sources into the detector. To cover this hole as well, another part of the OV is installed directly above the box.

6.3 Detector readout

The detector is readout by the data acquisition system (**DAQ**). A single cable for each PMT provides the high voltage to operate the PMT as well as the signal output. All cables are connected to splitter boxes, where signal and high voltage are separated. The signal information is lead to the Front-End boards. These distribute the signal to the triggering system and to flash analog digital converters (**FADC**). The signal is amplified to match the

full range of the FADCs, which digitize the waveform of the signal. The FADCs are of the type V1721 manufactured by CAEN©. They have a 8-bit resolution and a sampling rate of 500 MHz. The time interval of 256 ns was chosen to be digitized. The FADCs are readout every time there is a trigger given by the triggering system. For each trigger ID and IV are readout and for each event all waveforms are saved. They are stored in ROOT-files (see section 6.4 for details), which typically contain the information of one hour.

6.3.1 Trigger system

The triggering system consists of four trigger boards. Two boards for the Inner Detector, one for the Inner Veto and a trigger master board. The signals coming from the Front-End modules are led to three trigger boards. Here the PMTs are grouped and the group signal is processed. The criteria of the grouping of the ID-PMTs was an equally distribution of the PMTs on both trigger boards. The IV-PMTs are grouped geometrically: The IV is separated in several regions and the relative PMTs grouped respectively.
The several trigger boards are collecting the information about the amount of deposited light and lead it to the master board. If the sum signal of all PMTs in ID or IV or the sum signal of a IV-group are over certain thresholds, the detector will be readout. Additionally the master board has inputs for external triggers necessary for certain calibration methods[Rei09].
The thresholds depend on the trigger type. There are the following types:

- **Physics trigger:** The standard trigger. When the signal is above its threshold, the whole detector will be readout.
- **Prescaled trigger:** This trigger has a threshold below the Physics trigger. Its threshold is adjusted to be around 1000 events per second. As only each thousandth event is actually readout, it will trigger with the rate of one event per second. It is used to study physics below the trigger threshold especially for trigger inefficiencies.
- **External trigger:** The trigger system provides the opportunity to readout the detector by an external signal. The main reasons will be mentioned here.
  - **Calibration:** There are two calibration systems installed in the Double Chooz detector, one for the ID, one for the IV. These systems send light pulses into the detector to calibrate the PMTs. Therefore it is mandatory to readout the detector each time a pulse is sent.
  - **Fixed Rate:** To detect possible trigger inefficiencies below the threshold of the prescaled trigger, there is the so-called Fixed Rate trigger. It readouts the detector every second independently from all thresholds.
  - **Dead Time Monitor:** The Dead Time Monitor works in a very similar way as the Fixed Rate trigger. The difference is the underlying clock. While the Fixed Rate clock is generated in the trigger board, the one for the Dead Time Monitor is produced in a separated module outside the trigger system[Stü13].

The OV has an independent trigger system, which will not be discussed here.

6.4 Data processing and reconstruction

The data of the Double Chooz experiment is saved in ROOT format. This is a program for data analysis with a data format developed by a collaboration at CERN in Geneva in Switzerland. It was designed to handle the request of data analysis in particle physics. ROOT has an integrated C++ interpreter and can also be used as a class in C++ code. It provides special data analysis tools like histograms, functions and a fit-routine as well[ROOT].
A special analysis code was written by the collaboration based on the program ROOT. It is called Double Chooz Online Group Software (**DOGS**) and provides an easy data access and handling.
The raw data coming from the detectors is processed and reconstruction algorithms are applied. The first instance is the PMT-pulse reconstruction from the recorded waveforms. Here the charge deposition by the PMTs is reconstructed. For this purpose the baselines of the PMTs are mandatory. It can be reconstructed with the fixed rate trigger data. In most cases this trigger readouts an uneventful detector. With its information a mean baseline can be determined and the root-mean-square deviation of it calculated. In the physics trigger data pulses are found if the charge drops below the baseline and its fluctuation. The integrated charge is the sum of ADC-counts in the data taking time window after subtracting the baseline, its unit is *Digital Units of charge (Q)*, DUQ.
Another reconstruction algorithm leads to the spatial position of the event inside the detector. Here the time and charge information are compared with a point like source using a likelihood function. By maximising this function the most probable location of the event can be obtained. Also a merit factor from this maximisation is saved.
Calibration sources like Cf-252 and Ge-68 are used as well as neutron captures on hydrogen. Theses captures can be detected in the target and gamma-catcher. With the information from the spatial reconstruction and the reconstructed charge differences between the events a correction map is obtained.
There are reconstruction algorithms for possible muon tracks as well. These will be discussed in section 1 in chapter VI).

6.5 Simulations

For a good detector knowledge simulations are mandatory. With simulations it is possible to generate samples of pure signal and background events. Moreover simulations allow to test selection criteria and reconstruction methods.
For simulations regarding the Double Chooz experiment the Geant4 toolkit is used. Just as the ROOT program, Geant4 is developed by a collaboration settled at CERN. It is based on C++ as well.
Geant4 includes several geometrical objects like tubes or cuboid, which can be conjunct,

subtracted, etc. Materials are include and can be allocate to the objects. This allows the user to design a detector. Special material properties like a wavelength-depending reflectivity can be included as well.
Physical processes are implemented in separated models. Each model has a specific energy range where it is valid and was tested on data. Major part of each simulation is the physics list, where all physical processes used in the simulation can be switch on or off separately.

6.6 First results

The Double Chooz experiment published its results on θ_{13} in [DCC11, DCC12, DCC13, DCC14]. The resent publication[DCC14], where in total 467.9 live days of data were analysed, will be discussed here.

Single event selection As first steps in the neutrino candidate search muons and events in a certain time after are rejected as well as events which are not related with an energy deposition, but are due to discharges in the bases of the ID-PMTs.
Muons are identified as events which deposit 20 MeV or more visible energy in the Inner Detector or 30 kDUQ or more in the Inner Veto. Additionally all events following a muon in a time window of 1 ms are rejected as they include muon related events like captures of spallation neutrons or decays of unstable isotopes. A study to improve these cuts is presented in chapter VII.
Due to discharges in the bases of the ID-PMTs, light is emitted and recorded by the trigger system. These light noise events are rejected by a examination of the merit function of the spatial reconstruction presented in section 6.4. For the light noise events the reconstruction yields a less good merit factor as for energy depositions in the scintillator and thus light noise events can be separated with this factor.

Inverse beta decay candidate selection The following cuts were used to find inverse beta decay candidates:

- The prompt energy is between 0.5 and 20.0 MeV.
- The energy of the delayed event is between 4.0 and 10.0 MeV.
- The spatial distance between prompt and delayed event is smaller than 100 cm.
- The time difference between prompt and delayed event is in the range between 0.5 and 150 µs.
- There is no additional event 200 µs before and 600 µs after the prompt event except the delayed.

Background reduction

After applying the neutrino search cuts above the remaining background consists of unstable isotopes, spallation neutrons and stopping muons as mentioned in section 6.1.1. A pure reactor off sample was taken during seven days of the measuring time when both reactors were switched off. The data improved the understanding of the background that is intrinsic to the detector.
To suppress the backgrounds the following cuts are used:
Stopping muon veto: Similar to the light noise the spatial reconstruction of stopping muons deliver less good merit factors as point like events like a neutron capture. Therefore it is used to reject stopping muons from the delayed events.
IV veto: If the prompt event is coincident with a signal in the Inner Veto, which is higher than 400 DUQ, at least two PMTs saw a signal and the reconstructed distance between ID and IV signal is smaller than 3.7 m in the time interval of 50 ns, the event is rejected. With the mean gain in the IV of 136 DUQ/PE (see figure VIII.3 in chapter VIII) the 400 DUQ correspond to nearly 3 PE.
OV veto: If the prompt event is coincident with a signal in the Outer Veto in a time interval of 224 ns the event is rejected.
Li+He veto: For each inverse beta decay pair the preceding muons within 700 ms are studied. If one of the muons passed near the candidate and produced many spallation neutrons as well, the candidate is most likely a decaying Li-9/He-8.

Table III.1: Detected inverse beta decay candidates and background. The amount of predicted unoscillated reactor neutrino events and background events are listed[DCC14].

	Reactor On	Reactor off
Live-time [d]	460.67	7.24
IBD candidates	17351	7
Reactor $\bar{\nu}_e$	17540±320	1.57±0.47
^{9}Li/^{8}He	447^{+189}_{-74}	$7.0^{+3.0}_{-1.2}$
Spallation n + stop-μ	278±23	3.83±0.64
Accidental events	32.3±	0.508±0.019
Total prediction	18300^{+370}_{-330}	$12.9^{+3.1}_{-1.4}$

Result Table III.1 lists the found inverse beta decay candidates and their distribution in reactor neutrinos and background as well as the prediction of reactor neutrinos and background for the no-oscillation case ($\theta_{13} = 0$). They are input for a fit to the neutrino spectrum.
The resulting energy spectrum of the reactor neutrinos and the background is plotted in

figure III.8(a). The fit to the neutrino spectrum yields

$$\sin^2(2\theta_{13}) = 0.090^{+0.032}_{-0.029}.$$

The no-oscillation case can be excluded with 3.2 σ.
The table III.2 lists the uncertainties of the result separated by the sources.

Table III.2: Uncertainties of the oscillation result[DCC14].

Source	Uncertainty [%]
Reactor flux	1.73
Detection efficiency	0.63
^{9}Li + ^{8}He BG	+1.08 / -0.42
Fast-n + stop-μ BG	0.13
Statistics	0.77
Total	+2.27 / - 2.04

In figure III.8(b) the ratio of detected reactor neutrinos and predicted neutrinos for the no-oscillation case is plotted. Between 4 to 6 MeV the measured data points are significant above the best fit values. The origin of this excess is not known yet and currently under investigation. It can be shown that the amplitude of the excess scales with the reactor power[DCC14].

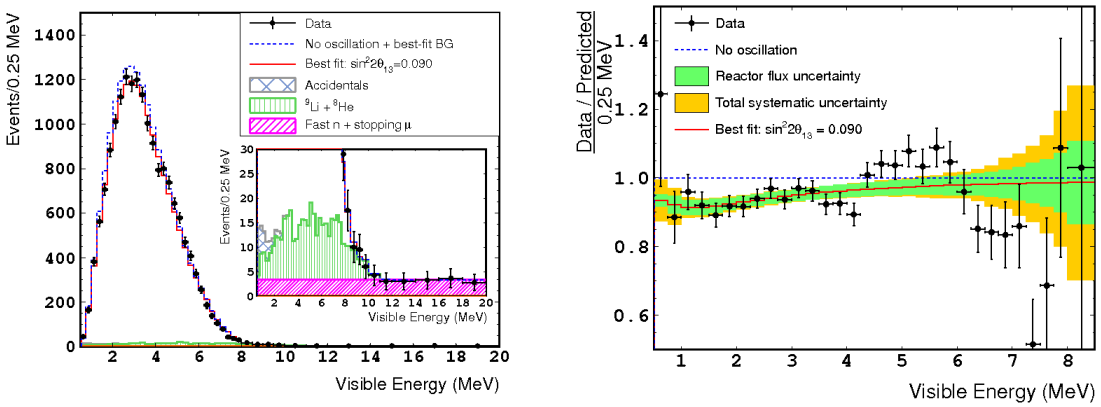

(a) Energy spectrum of IBD candidates

(b) Ratio data/prediction

Figure III.8: In the left the detected reactor neutrino energy spectrum and background events is shown. The right figure plots the ratio of detected neutrinos and prediction for the unoscillated case.[DCC14].

7 Daya Bay

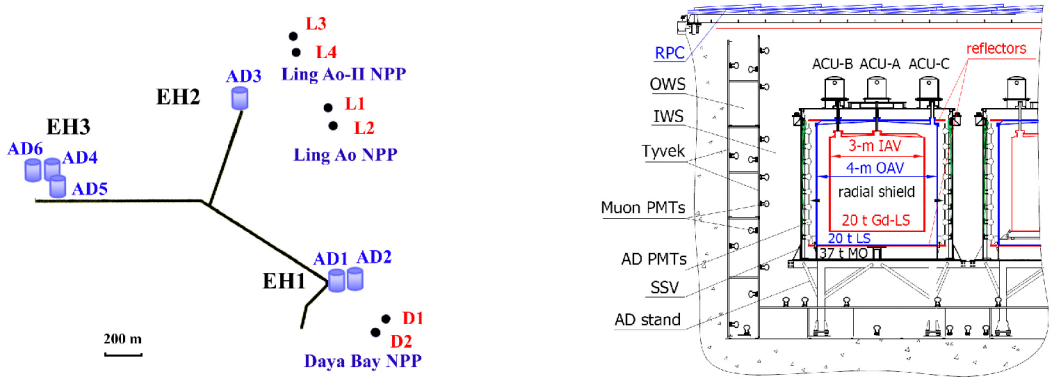

(a) Plan of the Daya Bay side

(b) Sketch of one Daya Bay detector

Figure III.9: In the left a sketch of the Daya Bay site with marked experimental halls (EH), detectors (AD) and reactor cores (L/D). The right picture shows a sketch of one exemplary Daya Bay detector. It consists of a inner and outer acrylic vessel (IAV/OAV) filled with Gd-doped and undoped scintillator surrounded by mineral oil (MO) in a stainless steel vessel (SSV). Each detector is equipped with three automatic calibration units (ACU). The detectors are installed in a water pool which is separated into an inner and an outer water shielding (IWS/OWS)[DAY12].

The Daya Bay experiment is situated in China 50 km north-east from Hong Kong in the hilly surrounding of the naming bay of the South China Sea. Six reactor cores are located near the detector site. Like the Double Chooz experiment Daya Bay measures the reactor neutrino flux near and far from the reactor cores. Due to the distribution of the six cores two near experimental halls are necessary. In figure III.9(a) a sketch of the site is plotted. The two near halls are marked with EH1 and EH2, the far is EH3. These halls offer space for multiple detectors. For the data of [DAY12] one detector was used in EH1, two detectors in EH2 and three in EH3 (the detectors are marked with AD (anti-neutrino detector) in the sketch).
Figure III.9(b) shows a sketch of one Daya Bay detector exemplary. The Daya Bay detectors are very similar to the Double Chooz detectors. Both consists of a target, a gamma catcher and a buffer region, but their sizes are different. The target mass for Daya Bay is 20 t, the buffer contains 20 t of liquid scintillator and the buffer is filled 37 t of mineral oil. Around the buffer cylinder wall 192 PMTs are mounted which are not tilted to the centre of the detector like in Double Chooz.
The veto system is the biggest difference to the Double Chooz detectors. Each experiment hall has a big water pool which offers place for up to four detectors. The water pools are instrumented with PMTs to detect crossing muons.
In [DAY12] the collaboration published a result on θ_{13} with

$$\sin^2(2\theta_{13}) = 0.092 \pm 0.016\,(\text{stat.}) \pm 0.005\,(\text{syst.}).$$

It is interesting to note that in the Daya Bay data a excess for neutrino events with 4 to 6 MeV occur as well[Pen14].

8 RENO

The RENO experiment (Reactor Experiment for Neutrino Oscillation) is situated in the south-west in the South Jeolla Province of South Korea near the coast of the Yellow Sea. Here the Hanbit nuclear power plant with its six reactors is located.
The RENO collaboration operates two detectors in two experimental halls: One near with 294 m and one far with 1383 m away from the centre of the reactor array. They have an overburden of 450 mwe for the far and 120 mwe for the near detector.
The RENO detectors are very similar to the Double Chooz and Daya Bay detectors. They share the same neutrino detection mechanism and the same composition with a Gadolinium-loaded scintillator in the centre, surrounded by an unloaded scintillator and a non-scintillating buffer volume. For the RENO detector, the target has a mass of 16.5 tons, the gamma-catcher of 30 tons and the buffer volume of 65 tons. To detect the scintillation light 354 PMTs of 10 inch diameter are operated which are mounted to the buffer vessel wall and are not tilted to the detector centre like in the Double Chooz experiment.
Like in Daya Bay the RENO detectors are situated in a water tank. This tank shields the detector against neutrons and is equipped with 67 PMTs to detect passing muons.
A result on θ_{13} was published in [Ren12]. It amounts to

$$\sin^2(2\theta_{13}) = 0.113 \pm 0.013\,(\text{stat.}) \pm 0.019\,(\text{syst.}).$$

Like Double Chooz and Daya Bay an excess for neutrino events with 4 to 6 MeV is visible in the RENO data as well[Seo14].

IV
The Inner Veto

Muons can produce events which may mimic the signal of an inverse beta decay. Thus they might be mistaken as a neutrino interaction. To discriminate against false-positive signals a high efficient muon detection in the detectors is crucial. Therefore both detectors are equipped with an active liquid scintillator based muon veto, which is called Inner Veto (**IV**) in contrast to the plastic scintillator panel based Outer Veto (**OV**) on top of the detectors.
In this chapter a general overview about the Inner Veto layout will be given. After that some possible modifications for the near detector Inner Veto will be discussed and the performed installation of the veto presented.

1 General information

The Inner Veto should detect muons, which enter the detector with high efficiency. It should also shield the inner detector volumes from radioactivity from the surrounding rock and from fast neutrons produced by undetected nearby passing muons. It is filled with liquid scintillator and equipped with PMTs to detect the scintillation light.
The Inner Veto is the outermost part of the Double Chooz detector expect for the steel/water shielding. The IV vessel is cylindrical shaped, 6810 mm high, has a radius of 3240 mm and is 10 mm thick. As the buffer vessel is enclosed by the veto the distance between both vessels is 482 mm on the sides and 557.5 mm on top and bottom. In total 90 m^3 of liquid scintillator are contained in the volume.
The Inner Veto was designed and is maintained by several groups inside the Double Chooz collaboration. The PMTs were provided by the Drexel group, tested by the University of Tennessee and encapsulated and installed by the Tübingen group. The scintillator was

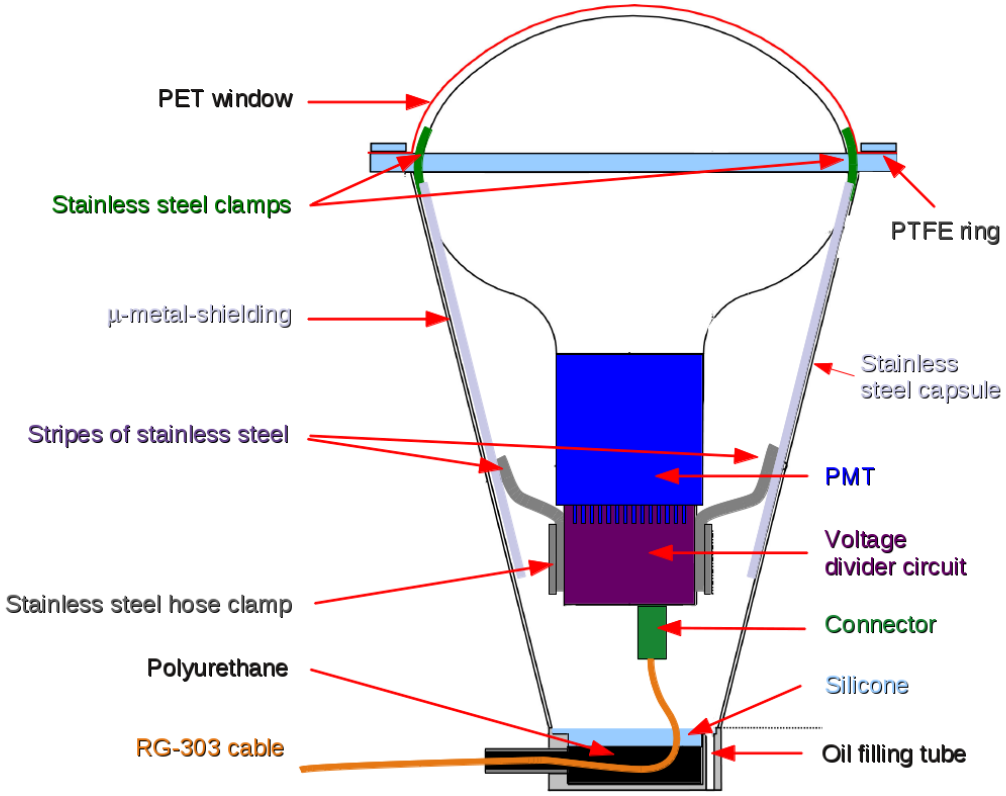

Figure IV.1: The PMTs used in the Inner Veto are encapsulated in a stainless steel capsule. A voltage divider circuit deliver the dynodes of the PMT with high voltage. This circuit is connected to a high voltage cable of the type RG-303 which leaves the capsule through a feedthrough. On top of the capsule a transparent PET window is flanged to it. The PMT is kept in place by stainless steel clamps near the flange and stainless steel stripes in the lower part. The latter a connected to the voltage divider circuit by a stainless steel hose clap. A µ-metal shields the PMT from magnetic fields. The capsule is filled with spectroscopy oil, which can be filled in by two oil filling tubes (one is sketched) and which are closed by a stainless steel screw. A PTFE ring at the flange and a layer of polyurethane at the cable feedthrough sealed the capsule. The polyurethane itself is isolated by silicon from the spectroscopy oil[Gre14].

developed, tested and provided by the Munich group, while the Strasbourg group built and installed the calibration system.

1.1 PMTs and their arrangement

The Veto PMTs have eight inch in diameter and are of the type R1408 produced by Hamamatsu. Some of these PMTs were reused from the decommissioned IMB[1] experiment.

[1]**I**rvine–**M**ichigan–**B**rookhaven experiment, data taking from 1981 since 1991. It was primarily built to search for a possible proton decay which was not observed. However it detected eight neutrinos from the

Table IV.1: Composition of the veto scintillator[Pfa12].

	Composition	Amount
LAB	50 $\%_{vol}$	45 m^3
n-paraffin	50 $\%_{vol}$	46 m^3
PPO	2 g/l	180 kg
BisMSB	20 mg/l	1.8 kg

The PMTs are encapsulated in a stainless steel capsule with a transparent PET window on top. This window is mounted to the capsule with a flange. Also a high voltage cable of the type RG-303 is fed into the capsule to provide the high voltage to operate the PMT. It is used to transport the PMT-signal as well. The cable is connected to a voltage divider circuit, where the high voltage is distributed to the individual dynodes of the PMT and the signal is readout. The capsule is sealed by a layer of polyurethane at the cable feed through and a PTFE ring at the flange. A spectroscopy oil is filled into the capsule which provides a similar refraction index than the scintillator. To fill the capsule it has two oil filling tubes, which are closed by screws. Figure IV.1 shows a sketch of the veto PMT capsule.
Several options for the number and the arrangement of the veto PMTs were tested. Options with 60, 72, 78 or 108 PMTs were studied[Die12]. The one with 78 PMTs had the best light collection characteristics and was chosen for the far detector.
The PMTs are arranged in three sections (see figure IV.2 for details): On the top of the veto there are two rings of twelve PMTs each. The inner of this two ring is mounted on the upper lid of the buffer vessel with the PMTs in alternating order. The PMTs of the outer ring are facing alternatingly into the top region and down into the space between buffer and veto vessel.
In half distance to the floor there is another ring of twelve PMTs: the middle ring. Here the PMTs are looking alternatingly up or down into the space between buffer and veto vessel as well.
On the floor, two rings with a total of 42 PMTs are situated. The outer ring with 24 PMTs is mounted on the veto wall and floor and facing alternatingly upwards and sidewards. The 18 PMTs of the inner ring are grouped in sets of three each in one of the six spaces between the buffer feet. Again, they are facing alternatingly in- and outwards.

1.2 The veto scintillator

The main components of the 90 m^3 of scintillator are linear alkylbenzene (**LAB**) and n-paraffin, a mixture of hydrocarbons with carbon chain length from 10 to 13. Their ratio was chosen to match the density of the Inner Detector liquids of 0.8 kg/l. Crossing particles will deposit energy in the scintillator, i.e. excite the LAB molecule. As LAB deexcite radiationlessly by itself, 2,5-Diphenyloxazole (**PPO**) is added to produce photons. As this light

supernova 1987A[IMB].

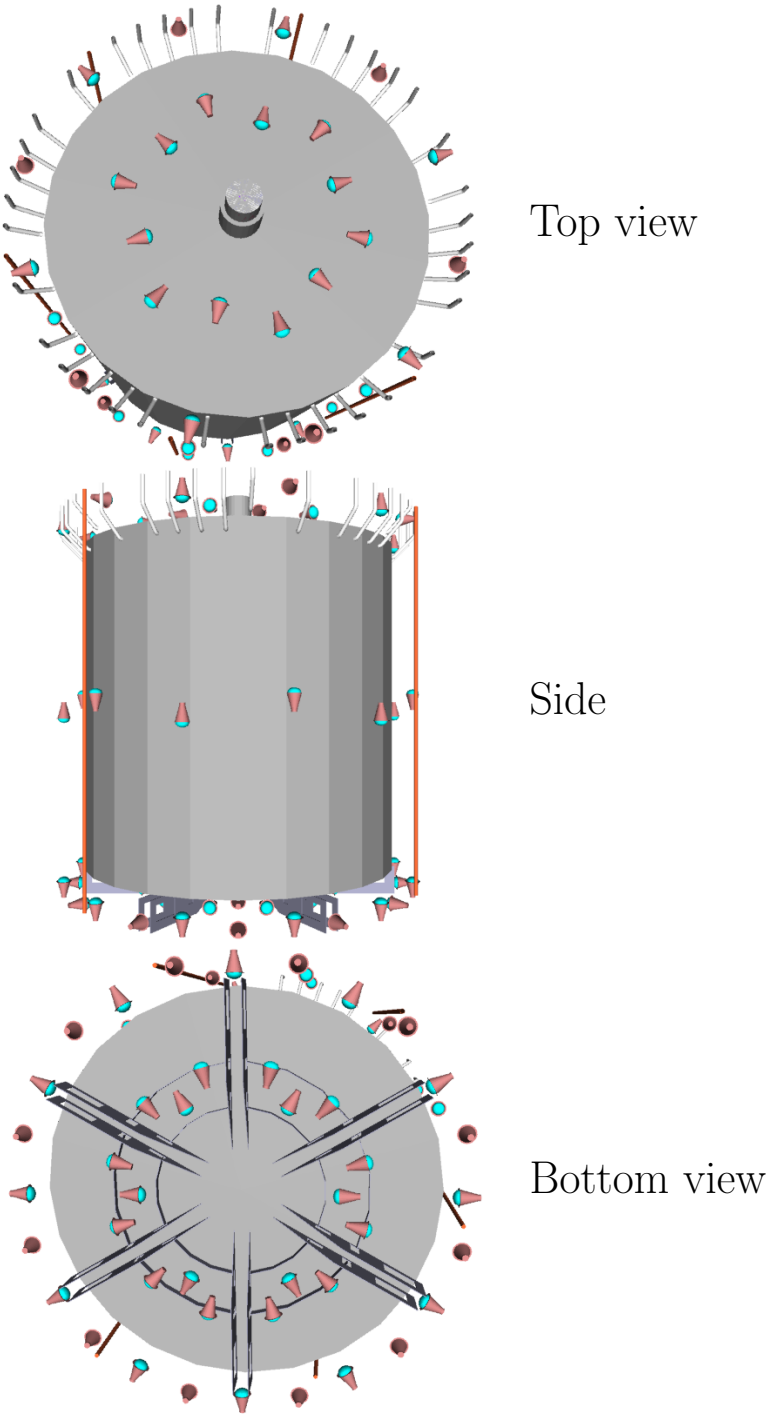

Figure IV.2: View of the outside of the buffer vessel which is the inner wall of the Inner Veto. The PMT positions are marked. The upper picture shows the top Inner Veto part with 24 PMTs, in the middle the 12 side PMTs are sketched and on the lower figure the bottom part with 48 PMTs is drawn[Die12].

would be reabsorbed to a large extend, a wavelength shifter 1,4-Bis(2-methylstyryl)benzene (**BisMSB**) is used to shift the scintillation light in the optical region, where the liquids are transparent and the PMTs are most sensitive[Pfa12].
In table IV.1 the veto scintillator components are listed as well.

1.3 Calibration system

To monitor the stability and response of the PMTs and the scintillator in situ without opening the detector or taking samples, each PMT in the veto is equipped with a glass fibre (some have an additional one for UV light). These fibres are connected to LEDs outside the detector, so that each PMT can be checked individually.
The glass fibres are mounted lateral to the capsule. Moreover the fibres are prepared in a way, that half of the light is emitted in the direction of the PMT, the other half inside the detector volume. With the knowledge of the distances of the PMTs to each other the light propagation in the veto can be studied and the attenuation length be measured. With the special UV LEDs the scintillation properties of the liquids can be checked as well.
But the main use of the fibres is to determine the gain and the temporal characteristics of the PMTs. For the gain measurement the LED is pulsed and the PMTs spectrum is recorded. From these results the gain can be calculated. For the PMT timing measurement the starting time of the PMT signal is compared to that of special reference PMT located outside.

2 Studies for the near detector's Inner Veto

As Double Chooz is performing a relative measurement between two detectors, the near and far detector should be as similar in design as possible. However this is only required for the Inner Detector part. Concerning the other detector components modifications are possible to see if improvements can be made.
In this thesis two possible modifications of the IV are presented which were made using Monte Carlo methods. The first modification is to increase the amount of PMTs in the veto for a better light collection. As a second modification a change of the surface coating of the veto vessel will be discussed.

2.1 Increasing the amount of PMTs

An increase of the amount of PMTs results in more active surface to detect scintillation light and in smaller distances between the PMTs, thus that light has smaller travel lengths before its detection. Contrarily as the PMTs are directly in the veto and not for example embedded in the veto vessel shadowing effects can occur. Therefore for this work a Geant4 simulation with 90 PMTs was performed to study the mentioned effects and will be compared to an identical simulation with the original 78 PMTs.
Unlike the version with 108 PMTs in [Die12] with PMTs facing the buffer walls and looking

in the direction of the Inner Detector the option with 90 PMTs studied here is similar to the 78 PMT version, except for a second middle ring of 12 PMTs. Therefore it contains four rings of PMTs equally spaced (bottom region with 42, lower middle ring with 12, upper middle ring with 12 and top region with 24 PMTs).
In order to test for typical low energetic events 100,000 electrons with 1 MeV were generated at randomly chosen positions in the veto and the photo electrons (**PE**) observed by the PMTs were compared. Like in [Die12] events with 10 PE or less were considered as not detectable. This is a conservative estimation as for the setting of the veto flag from the IV used in [DCC14] an amount is required which is comparable to 3 PE (see section 6.6 in chapter III.

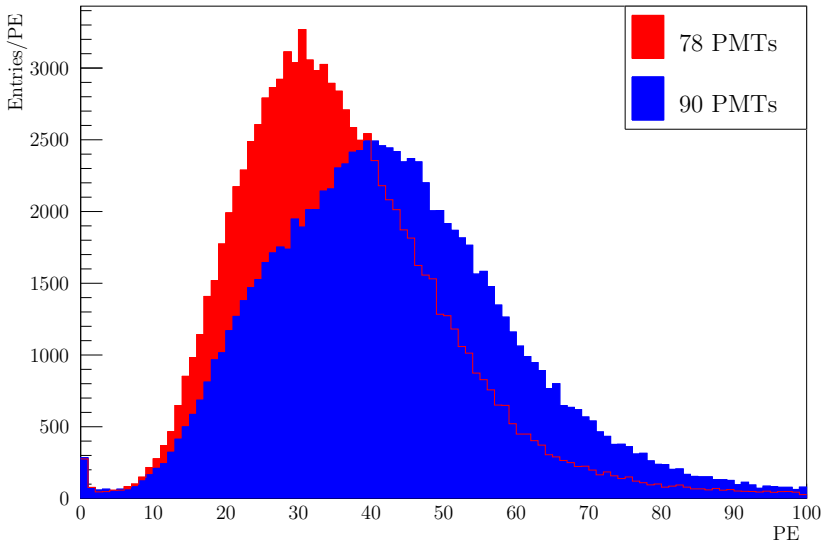

Figure IV.3: Simulated distribution of photo electrons of 100,000 electrons of 1 MeV, generated at randomly chosen positions in the Inner Veto for arrangements of 78 and 90 PMTs.

Figure IV.3 shows the results of these simulations: As expected 90 PMTs in general provide a better light collection. The amount of events with ten or less photo electrons for both solutions small.

Table IV.2: Mean PE and events with ≤ 10 PE for 78 and 90 PMTs.

	78 PMTs	90 PMTs
Mean PE	38.19	45.54
events with ≤ 10 PE	1.38 %	1.24 %
events with ≤ 5 PE	0.56 %	0.60 %

Table IV.2 expresses this quantitatively. The mean amount of photo electrons is increasing by 19 % while the amount of events with 10 ore less PE decreases by 11 %, yet for events

with 5 or less PE there is even an increase of 6 %. Like in [Die12] this could occur due to shadowing effects of the new PMTs.
To prove this estimation the starting positions of the events with 5 or less PE are plotted in figure IV.4. For both PMT arrangements these events are located at nearly the same places. In the top region three rings occur which can be assigned to the chimney, the veto vessel and the inner PMT ring. As the chimney is not instrumented with PMTs it is not remarkable that many of the low-PE events started here. The accumulation near the inner PMT ring is a hint, that shadowing effects could occur, if the events were started directly next to a PMT capsule, but not in front of its light entrance window. Another accumulation can be seen near the outer wall, where also PMTs are mounted, which can cover events happening here. Very similar to the top is the bottom region. The starting points of events with 5 or less PE accumulate near the outer wall and the inner PMT ring as well. In the side region an accumulation near the PMT ring is visible, but most of the low-PE events occur here at other positions: First, in the side top region, where the buffer lid is extended into the veto and the tubes are located, which transfer the PMT cables through the veto to the outside. The second position is along the tubes of the thermal control system, which consists of six tubes going vertically through the veto.
As the amount of events with low PE numbers is not decreasing with a higher amount of PMTs, it was decided not to implement the new design.

2.2 Veto surface

Due to more available space in the near laboratory and the lower costs the near detector will have a water shield instead of a steel shielding around the Inner Veto vessel. Therefore stainless steel was chosen as the material of the IV vessel. The far detector's IV vessel was built out of steel. Also due to cleanliness requirements in the laboratory no sandblasting of the inner surface of the IV vessel was possible. Hence a painting of the vessel like it was done for the far detector was not feasible as a roughening will ensure the permanency of the paint.
To ensure a high reflectivity nevertheless, several options were contemplated. As the scintillator is chemically a solvent the surface must be resistant to it. Any solved material can attenuate the light propagation in the scintillator and therefore reduce the absorption length. Three options were considered: Polishing the stainless steel, white painted stainless steel tiles and sheets of VM 2000 foils.

Polished stainless steel

The stainless steel parts from which the veto vessel is assembled are polished to give its surface a higher reflectivity. This is the easiest solution, because no additional and potentially dirt-introducing work is necessary, except for the polishing, which can take place at the manufactures site.

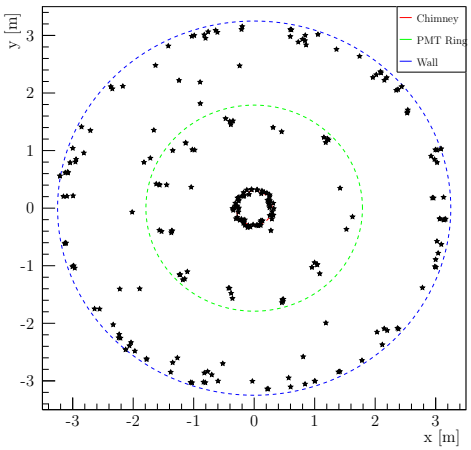

(a) 78 PMTs - Top

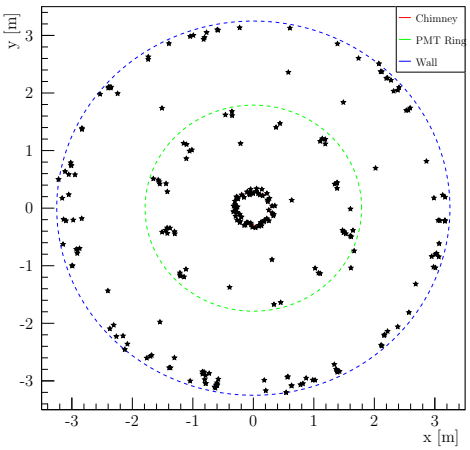

(b) 90 PMTs - Top

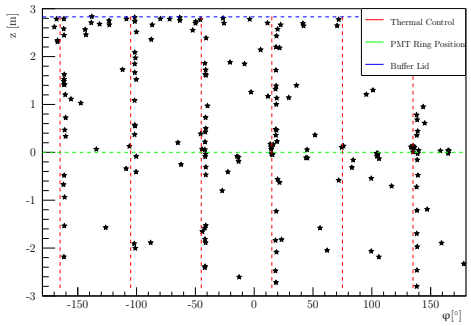

(c) 78 PMTs - Side

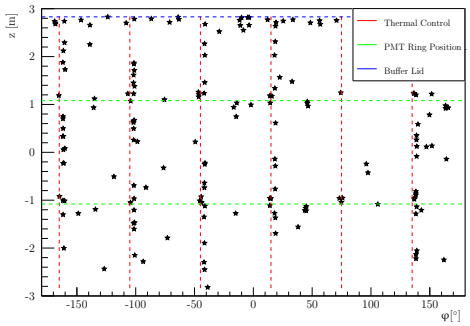

(d) 90 PMTs - Side

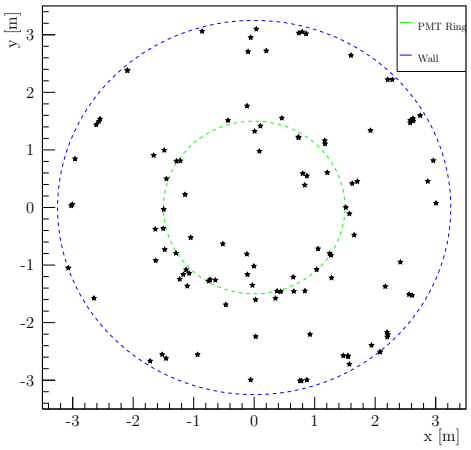

(e) 78 PMTs - Bottom

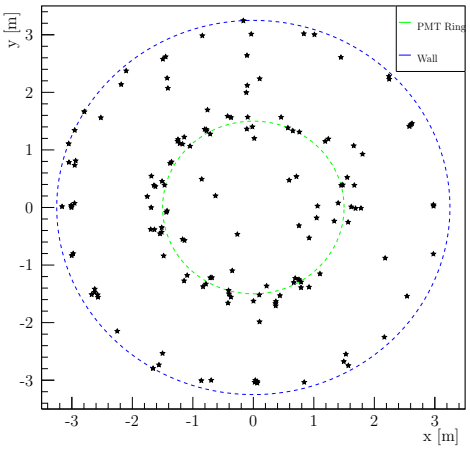

(f) 90 PMTs - Bottom

Figure IV.4: Starting positions of events with 5 or less PE for simulations with 78 and 90 PMTs. Also marked are elements in the veto, which can introduce shadows.

White painted stainless steel tiles

To make the two vetos as similar as possible under the given conditions white painted stainless steel tiles were proposed. The paint is the same as it was used in the far detector. The tiles are curved, cover the walls of the veto and are mounted using bolts.

Sheets of VM 2000 foil

As the VM 2000 was already used in the far detector to increase the reflectivity of the buffer vessel surface, it is also possible to use it for the veto vessel. Like the steel tiles the VM 2000 sheets are mounted on bolts to the veto vessel. As the glue of the foil will dissolve in the scintillator the glue has to be removed and hence a special support structure is necessary to keep it in place.

2.2.1 Reflectivity measurements for different surface types

To test these three surface options, probes of polished stainless steel and the white paint were sent to the Max Planck Institut für Kernphysik (MPIK) in Heidelberg, where Benjamin Grämlich measured their reflectivity for several wavelength in the optical field and near ultra violet (**UV**) with a UVVis-spectrometer. A measurement of the VM 2000 foil was already done for [Kna09]. Before this measurements in the Double Chooz simulation only estimated values for the reflectivity of the paint were used, which were deduced from the reflectivity of PTFE.

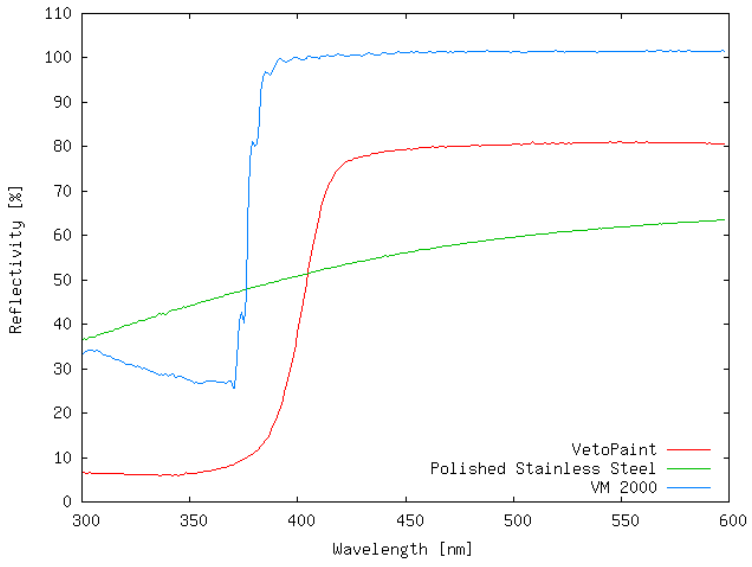

Figure IV.5: Total reflectivity of possible surface options for the Inner Veto of the near detector. The reflectivity versus the wavelength is shown. Two measurements were performed at the MPIK in Heidelberg (veto paint and polished stainless steel). The results for the VM 2000 are taken from [Kna09].

In figure IV.5 the results are shown. It is clearly visible, that VM 2000 has the highest reflectivity of the three tested surfaces in the optical field, where it is almost a perfect mirror. For wavelengths shorter than 400 nm its reflectivity is reduced severely down to about 30 %.
The paint which was used as surface cover of the veto vessel in the near detector has a nearly constant reflectivity of 80 % in the optical field and then also drops to 10 % in the near UV regime.
Polished stainless steel has the lowest reflectivity. In the optical field only values of 60 % can be obtained, yet in contrast to the both other surfaces the reflectivity is only slightly decreasing in the near UV.

2.2.2 Simulations based on the reflectivity measurements

These results were put into the Double Chooz simulation package (see section 6.5 in chapter III). To test the light distribution in the Inner Veto the light output of 100,000 electrons with 1 MeV was simulated for each surface option. The starting positions were randomly chosen in the veto volume. The energy deposition and light propagation was simulated and the amount of detected photo electrons recorded.

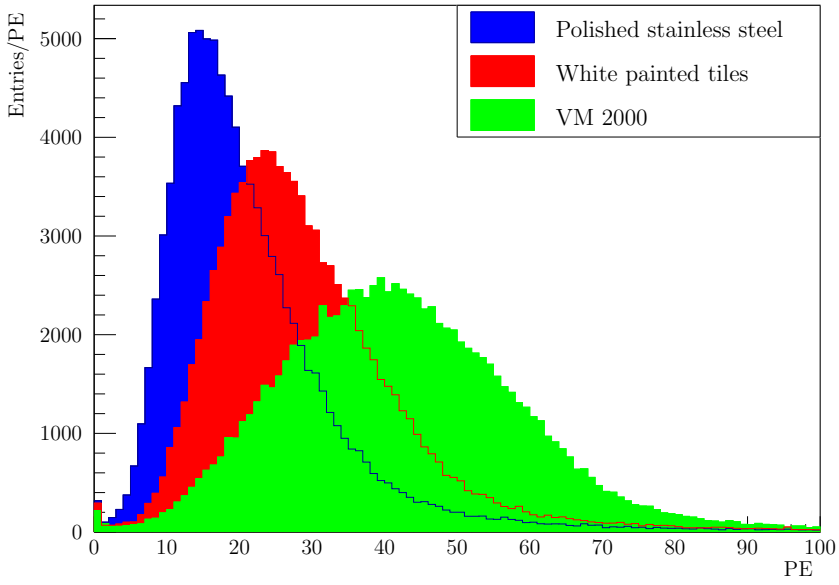

Figure IV.6: Simulated distribution of photo electrons of 100,000 electrons of 1 MeV started at random positions in the Inner Veto for each veto wall surface option.

In table IV.3 the results are expressed in numbers: The mean photo electrons per event are increasing from polished stainless steel to the VM 2000 by a almost a factor of two and the amount of events with ten or less detected photo electrons is decreasing from 13 % to

Table IV.3: Mean PE numbers and events with 10 PE or less for polished stainless steel, white painted tiles and VM 2000.

	Polished stainless steel	White tiles	VM 2000
Mean PE	22.92	30.89	44.45
events with ≤ 10 PE	13.5 %	3.0 %	1.3 %

1 % of all events.
Based on this results it was decided to use sheets of VM 2000 as surface of the veto due to its high optical reflectivity. Also the handling of the VM 2000 sheets is much easier than the stainless steel tiles as the sheets are much lighter and easier to adjust to the curved veto walls. A third argument for the sheets was their lower price in comparison to the white painted tiles.

2.3 Design changes for the Inner Veto of the near detector

A design plan was made to cover the surface most efficiently with VM 2000. The dimensions of the available rolls of the VM 2000 are a restriction to the use. Each roll contains a sheet of foil 45.7 metres long and 1.24 metres wide.

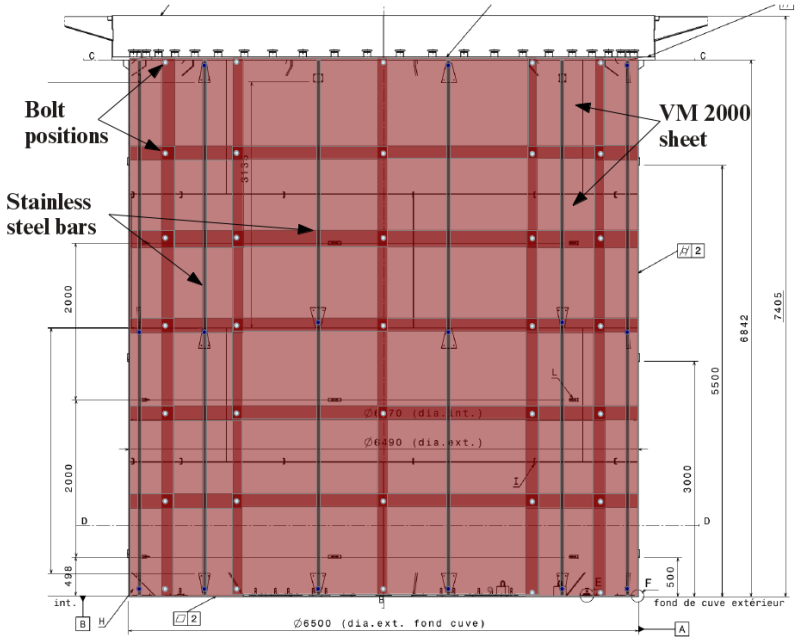

Figure IV.7: Sketch of the veto side wall with marked VM 20000 sheets, bolt positions and stainless steel bars. For details see text.

In figure IV.7 the installation plan for the side wall coverage is sketched. In total 72 sheets

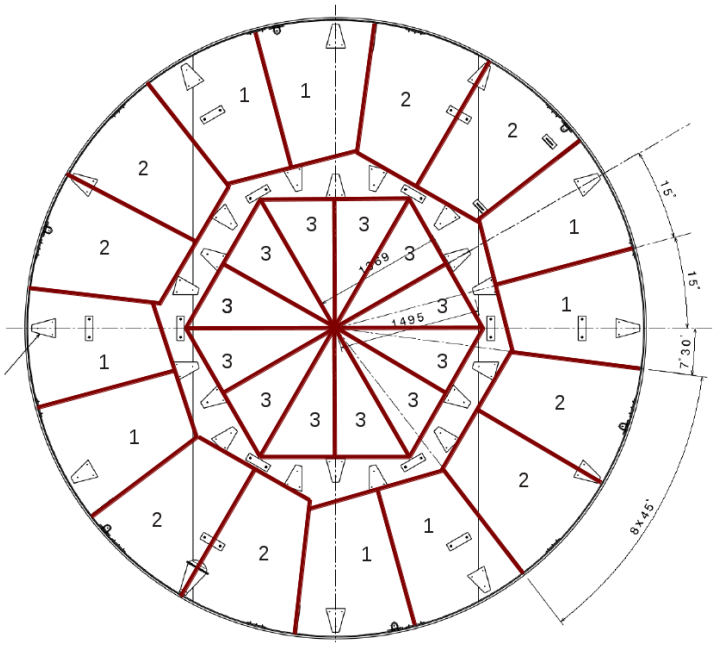

Figure IV.8: Drawing of the veto floor with marked VM 2000 sheets. The three sizes of the sheets are marked with numbers.

of VM 20000 in seven rows of twelve sheets cover the wall from top to bottom. Additional bolts were required to keep the sheets in place. The sheets have stainless steel eyelets in their corners to fix them to the bolts. The sheets overlap and share a bolt for the outermost rings and for the five inner rings four sheets are mounted on each bolt.
The bolt positions are located in the middle between to the PMT positions. To keep the sheets close to the wall, additional stainless steel bars were used. They are mounted on the bolts which also carry the PMTs.
The plan for the veto floor is shown in figure IV.8. Due to the amount of support structures on the floor, 28 VM 2000 sheets and 50 bolts are necessary. This 28 sheets can be cut using three forms, yet it is crucial that the forms can be used from both sides. Detailed drawings be found in the appendix, chapter A.

3 Installation of Inner Veto of the near detector

VM 2000 is only available with glue on its backside from the manufacture. This glue is soluble in the veto's scintillator. Therefore the glue has to be removed before the the foil is mounted. For the far detector's veto, acetone was used to remove the glue. As acetone is lightly flammable and aggressive to human skin for this work a different solvent was used for the glue. It is a dibasic ester called DBE© from the company Lemro©[DBE]. It is a

solvent like acetone, but less aggressive and has a flash point of 103 °C. Therefore it is much safer to work with compared to acetone.
The installation in Chooz took place in two periods. It began with the mounting of the 54 PMTs of the bottom and side in summer 2013. In addition the VM 2000 sheets on the veto and buffer wall were placed that year. In spring 2014 the remaining 24 PMTs of the top were installed.

V

The Inner Veto spectrum and rate

In this chapter features of the Inner Veto deposited charge spectrum of the far detector will be discussed. A detailed study of the trigger system of the Inner Veto is also presented here. With a special trigger mode a study of the low-charge region of the Inner Veto was possible. With this information the total event rate can be estimated. A comparison to muon simulations will allow to determine a rough charge-to-energy and charge-to-PE conversion factor.

1 The Inner Veto charge spectrum

The IV spectrum is conventionally given in an unit unique to Double Chooz, called *Digital Unit of Charge(Q)* or short *DUQ*. It is proportional to the flowed charge at the PMTs (see section 6.4 in chapter III). There are methods to transfer this information into the amount of detected photo electrons, but as they are not fully developed in the following the unit DUQ will be used.
Figure V.1 shows the charge spectrum of the far detector's Inner Veto for a lifetime of around 251.7 days, no cuts have been applied. All recorded energy depositions in the veto were used. A zoom into the lower charge region is shown in the upper right of the figure. After an exponential decline a first peak appears around 15 kDUQ, followed by another exponential decline. Between 30 and 40 kDUQ another peak is visible, which is more pronounced than the one before and which is again followed by a decline. At around 100 kDUQ the spectrum is almost flat, while at 200 kDUQ a step is visible. After another flat part starting at 300 kDUQ a broad and intense peak emerges. It is centred between 400 and 500 kDUQ. After this peak the spectrum is declining smoothly.
The mentioned structures have their origin in muons crossing the Inner Veto and trigger-

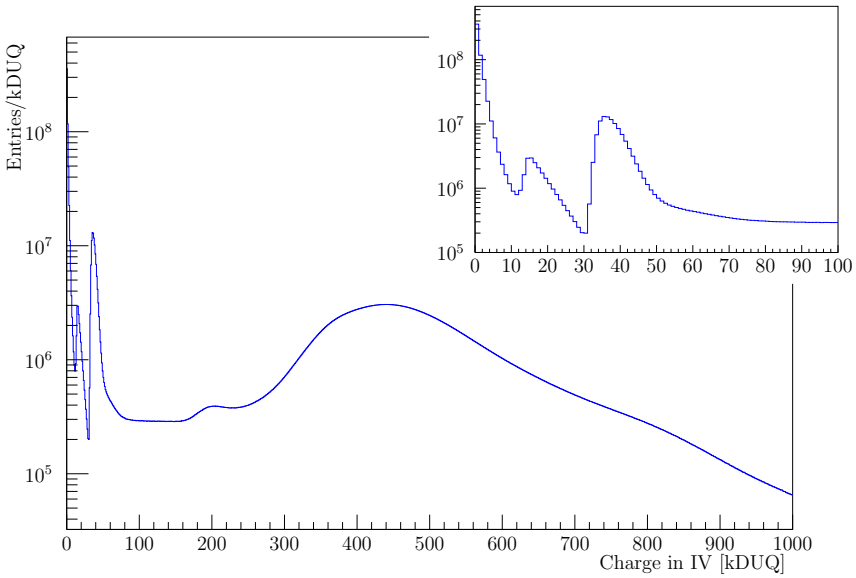

Figure V.1: Charge spectrum of the Inner Veto of the far detector. For this spectrum all triggered events have been considered. A zoom into the lower charge region is plotted in the right upper corner.

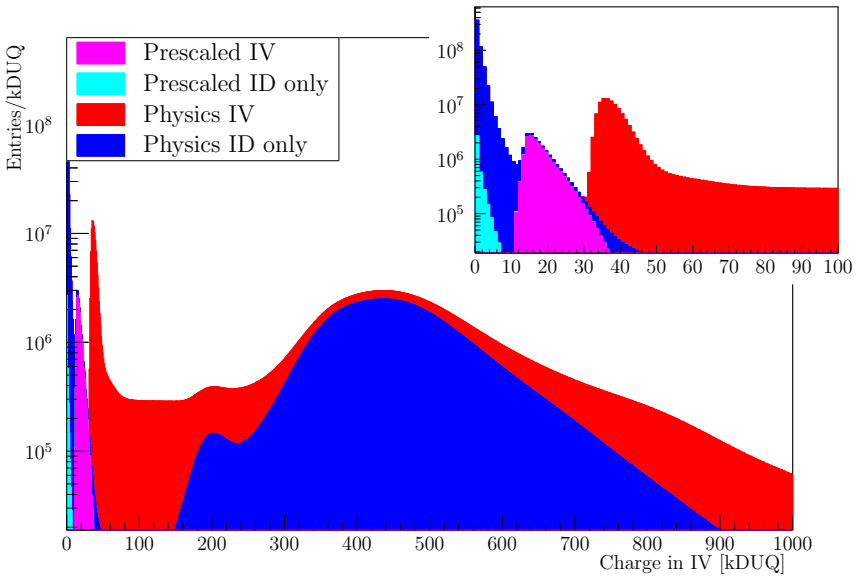

Figure V.2: The summed charge spectra separated by the recording trigger type. The low charge peaks in V.1 are thresholds of two trigger types. This will be discussed in detail in section 3.

ing effects. It is possible to separate the events by their recording trigger (see figure V.2 and section 3) In the following sections the separate structures will be explained and a comparison to Monte Carlo simulations will be discussed.

2 Muons in the Inner Veto

Muons at the Double Chooz site are mostly high energetic with a mean energy of 63 GeV for the far detector. Although most of them are minimal ionizing, they deposit large amounts of energy along their tracks as these tracks are rather long. The major fraction of the muons are not stopped inside the detector and leave it again. Due to the geometry of the Inner Veto many muons are crossing it twice, before and after their journey through the Inner Detector. Only if a muon stops inside the Inner Detector or if it enters through the chimney, it will cross the Inner Veto once. A sketch of possible muon paths is shown in figure V.3.
To study possible tracks in Inner Veto a small simulation was made, where pseudo-muons were propagated through a simplified detector which consists of two concentric cylinders: one for the IV and one for the ID. The particles were started in a circle of 10 m diameter above the detector 10 m away of the centre. Angular distribution values computed by MUSIC (see section 2.1) have been used. The particles were propagated along their tracks, no physical interaction has been considered. To study stopping effects as well, roughly four percent of the particles were started in the bottom part the Inner Detector cylinder with the same angular distribution, but propagated reversely to the top of the detector.
In the upper figure of V.4 the simulated track length are plotted. Four peaks occur: One at 60 cm, a second at 120 cm, a third at 150 cm and a fourth at 680 cm. For a further investigation the veto volume was divided into three sub-volumes: Two plain cylinder at top and bottom and a hollow cylinder in the middle. In the lower figure of V.4 the tracks are separated by the crossed sub-volumes. It is visible that the first peak appear due to stopping muons which penetrate only the top or side region (muon 3 in figure V.3). The second peak at 120 cm is caused by muons which crosses through the top and bottom region (muon 2 in figure V.3). When a muon travel through the side and either top or bottom region it will create the third peak at 150 cm (muon 4 in figure V.3). A muon which is crossing the whole Inner Veto will induce the fourth peak at 680 cm (muon 1 in figure V.3).
To understand how these peaks in the muon track length correspond to peaks in the charge spectrum a detailed muon simulation is necessary which will be discussed in the next section.

2.1 Muon simulation with MUSIC and Geant4

As a starting point for muon simulations it is necessary to know their energy spectrum and their angular distribution. In section 3 of chapter II the energy and angular distribution

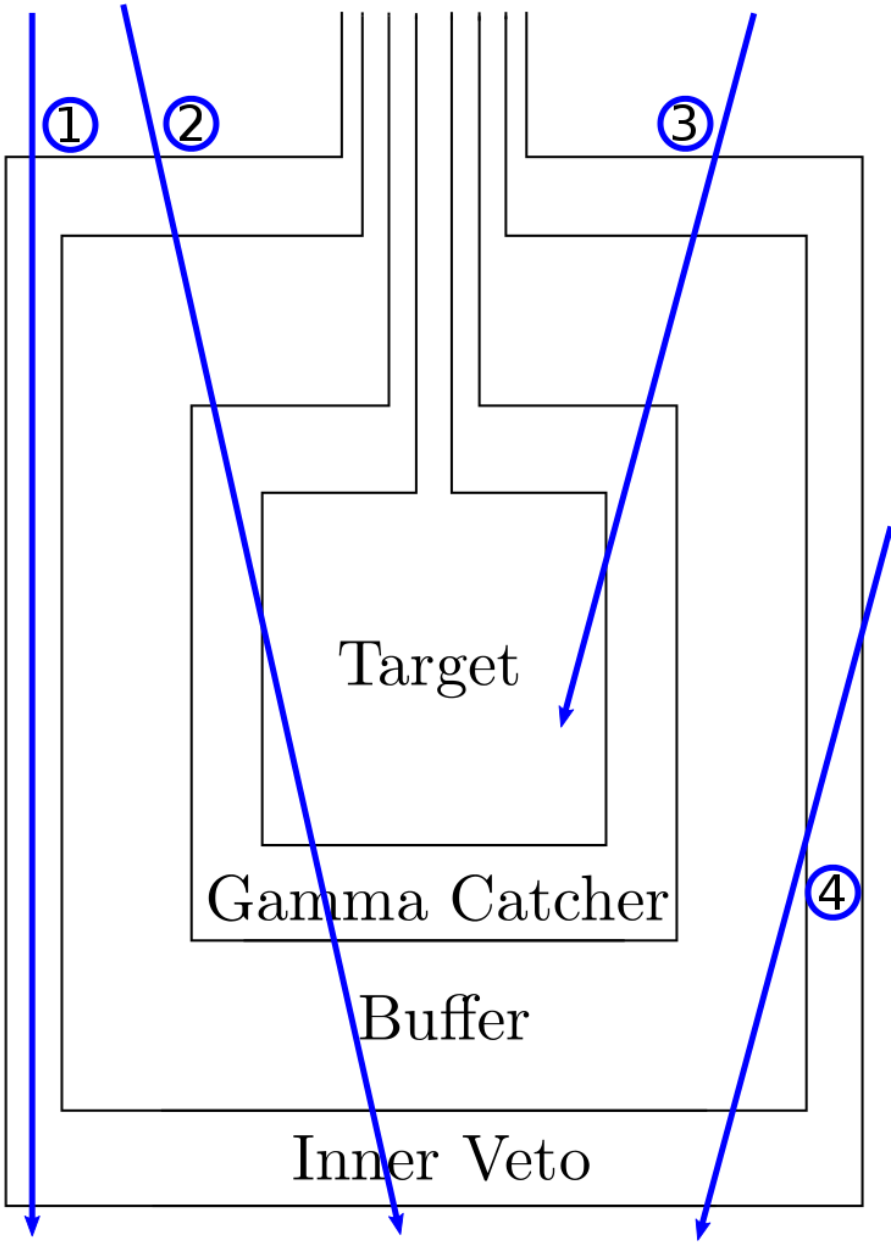

Figure V.3: Sketch of the Double Chooz detector. As example four possible muon tracks are marked. From left to right: 1. A muon which is travelling a longer distance in the IV, 2. a muon which is crossing the IV through the top and bottom region, 3. a muon which is crossing the IV once and is stopped in the Inner Detector and 4. a muon which is crossing the IV through the side and bottom region.

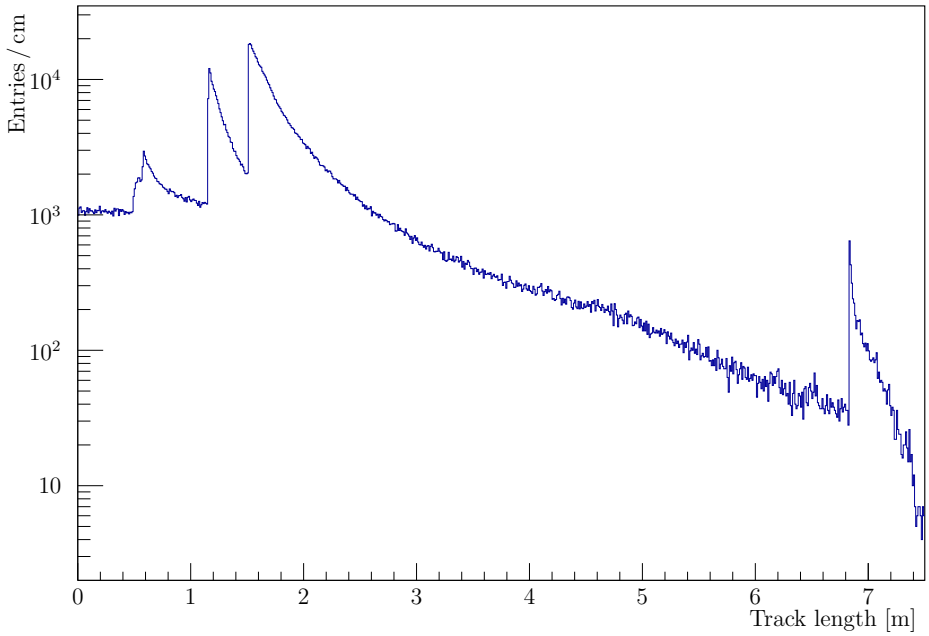

(a) Simulated track length in the Inner Veto

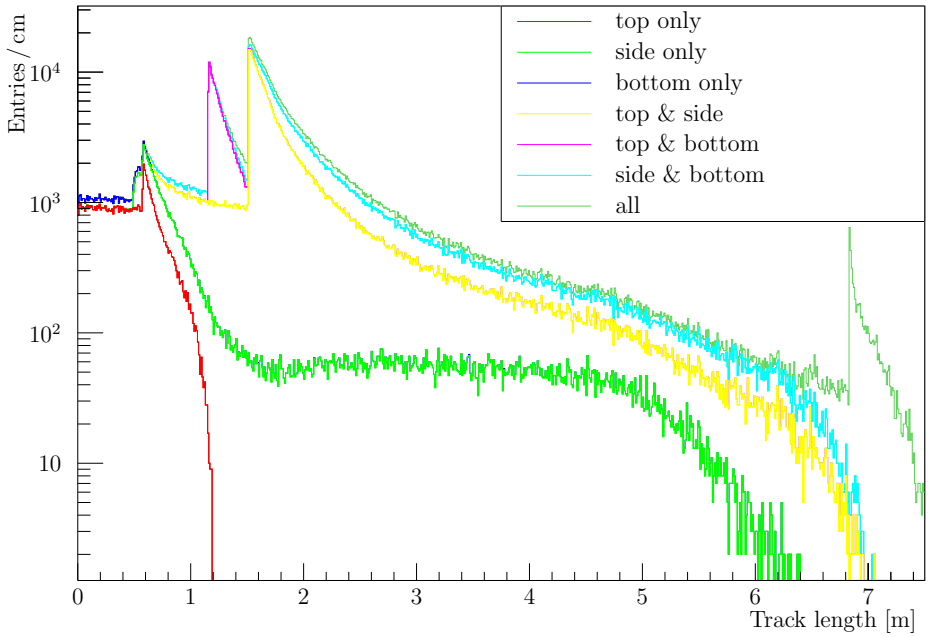

(b) Simulated track length separated by IV sub-volume

Figure V.4: Simulated track length in the Inner Veto. The upper figure shows four peaks. In the lower figure these tracks are separated by the crossed IV sub-volumes (see text for details).

for muons under open sky are described. If the muons travel through matter, this will affect the energy and angular distribution depending on the travel length and the chemical composition of the penetrated material. These effects can be simulated with MUSIC.

2.1.0.1 The MUSIC framework MUSIC stands for **MU**on **SI**mulation **C**ode and is a Monte Carlo simulation written by V. A. Kudryavtsev et al. in the programming language Fortran. It is simulating the propagation of muons through rock. With given topology and rock composition it is calculating the energy and angular distribution of muons in an underground lab[Kud08].
The topology of the Chooz site and the chemical composition of the surrounding rocks are well known [Bal95] and several muon simulations with MUSIC were performed with this data.

2.1.0.2 Geant4 The results from MUSIC are used as input for another simulation with the Geant4 tool kit.
To guarantee a homogenous flux through the whole detector as well as the production of nearby passing muons the muons are started in the following way [Gre14]:

- Energy and angle for the muon are chosen randomly out of the MUSIC results
- Beginning from the detector's centre a point ten meters away against the flight direction of the muon was selected.
- At this point a plane was defined, which is normal to the flight direction. It is quadratically shaped and has a side length of 20 m.
- A randomly chosen point on this plane is used as starting point of the muon with the initial energy and angle.

2.2 Comparison with muon simulation

To verify that the peaks between 100 and 500 kDUQ are of geometrical origin a simulation of muons in Double Chooz is used. The starting energy and angular distribution was taken from the output of the MUSIC code like it is described in the section above. For this study a Double Chooz common simulation of 686,000 muons were used, from which 548,384 hit the Inner Veto.
For all muons the track length, the deposited energy and the produced PE in the Inner Veto were analysed. In figure V.5(a) the track length of the muons are plotted. It is quite similar to V.4, thus the estimation of straight propagating muons which were used for the study in V.4 was justified. Most of the muons are minimal ionizing particles as it can be seen in figure V.6(a) where the deposited energy per track length in the IV is plotted. Thus in general the deposited energy of a muon is related to its track length in the IV. A Landau function was fitted to figure V.6(a) and resulted in a mean of $dE/dX = 1.749\,\mathrm{MeV/cm}$.
With the help of a muon reconstruction algorithm (see section 1 in chapter VI) the track

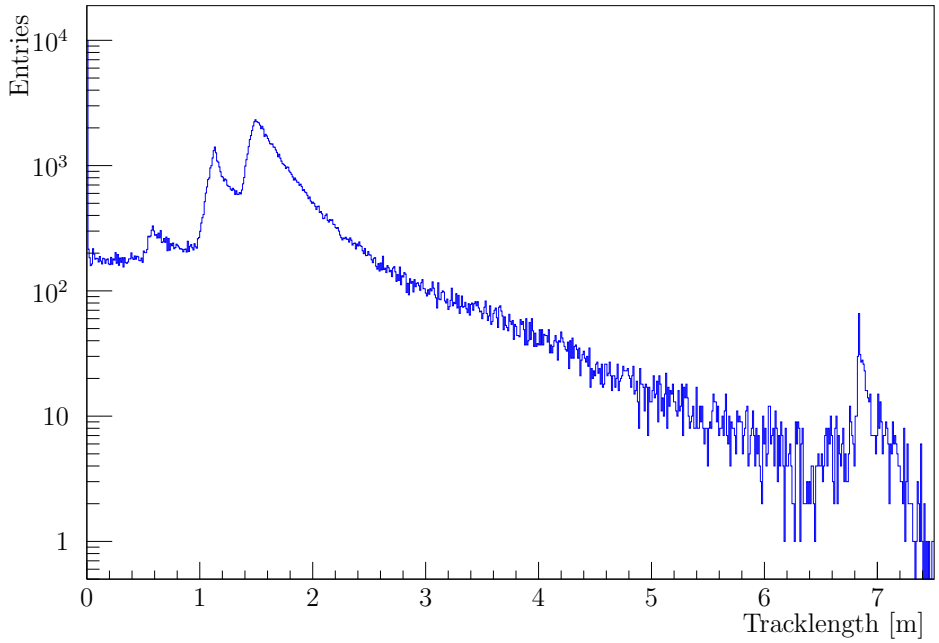

(a) Monte Carlo

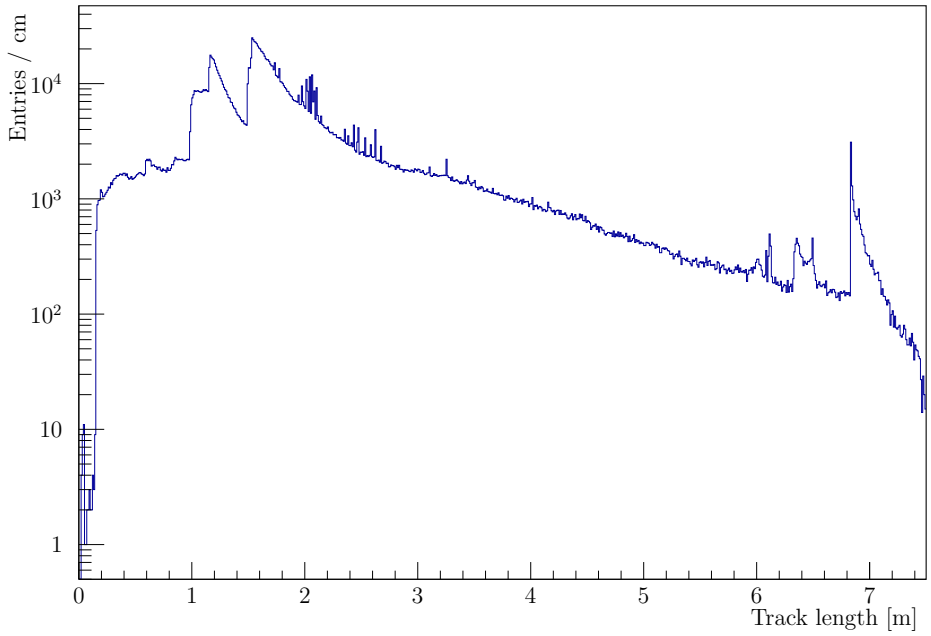

(b) Data

Figure V.5: Track length in the IV from simulation and data. The upper figure shows the track length of simulated muons, while the lower plots the reconstructed track lengths in data.

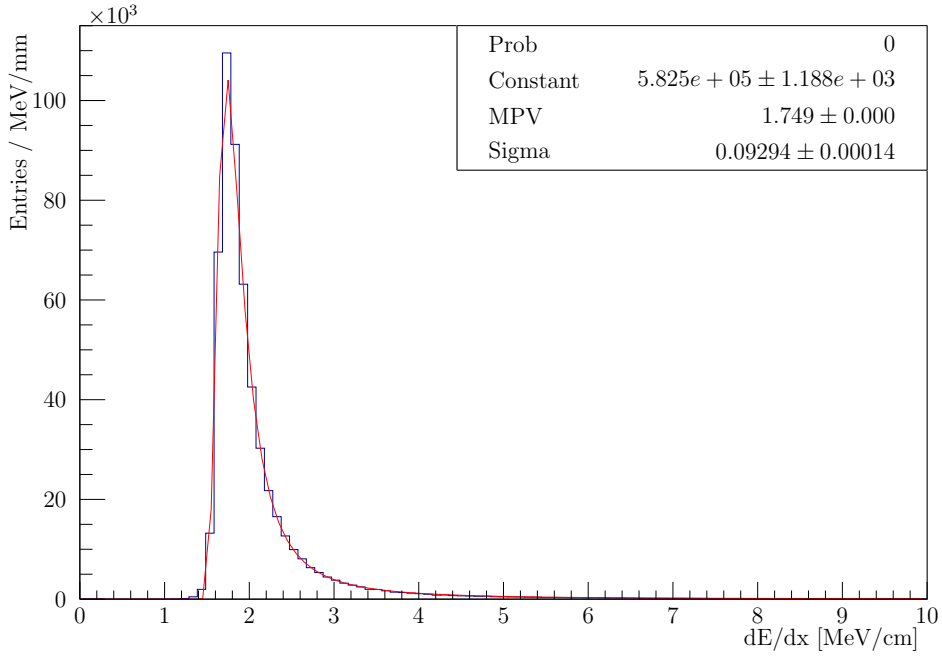

(a) Monte Carlo

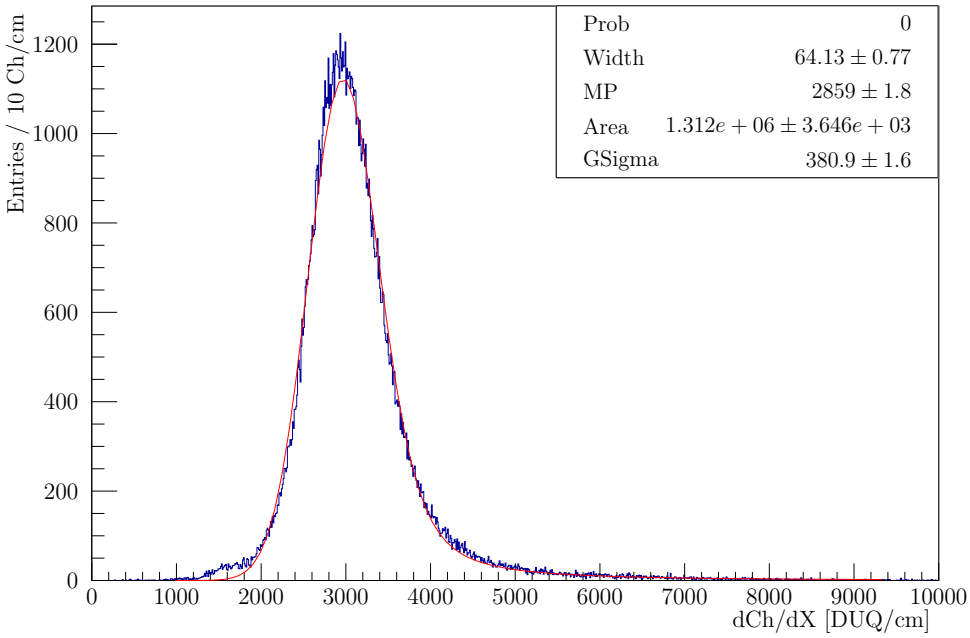

(b) Data

Figure V.6: Deposited energy/charge per the track length in simulation and data. In the upper plot the deposited energy per track length of simulated muons is plotted with a Landau function fit to the distribution. The lower figure shows the charge per reconstructed IV-track length for data. Here a convolution of a Gaussian and Landau function is necessary to fit the data.

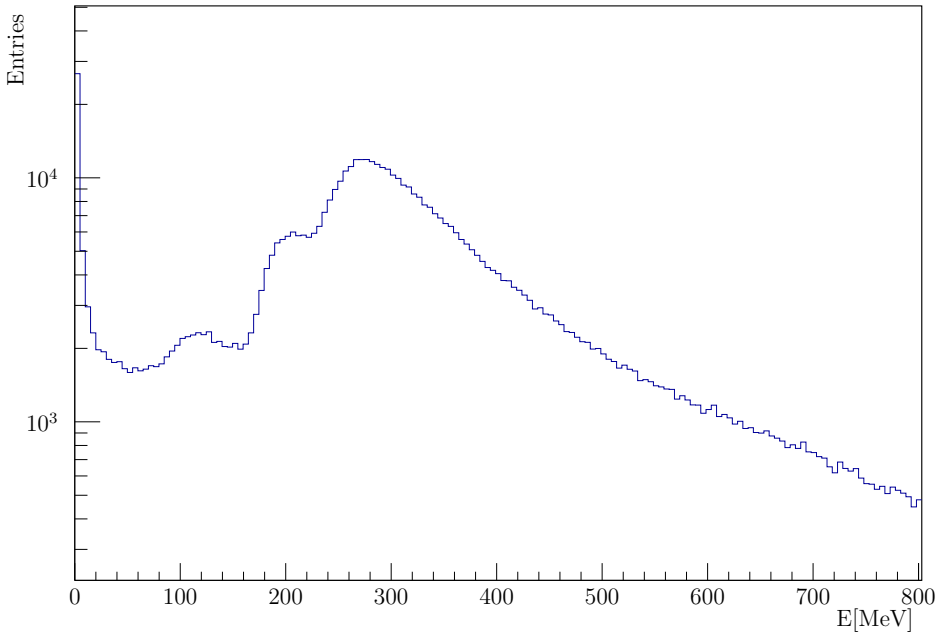

(a) Deposited energy

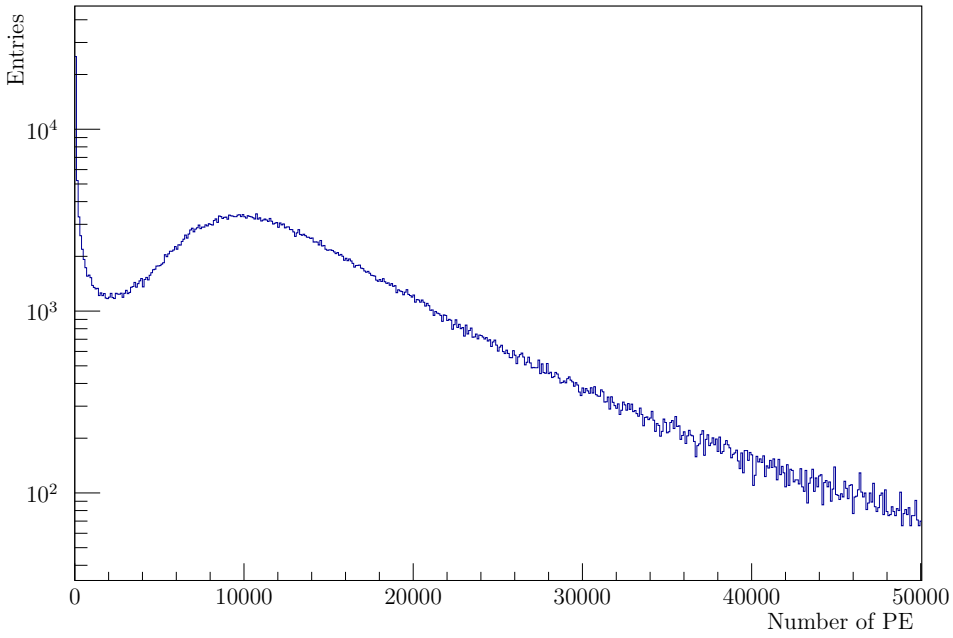

(b) Photo electrons

Figure V.7: Distributions of the energy deposition (top) and produced photo electrons (bottom) of simulated muons in the Inner Veto.

length of events in the Inner Veto can also be calculated. For this study the Fido algorithm was used. In figure V.5(b) reconstructed track length in the Inner Veto are shown. No cuts were applied, only the reconstruction needed to succeed. Therefore events with a very small track could not be reconstructed and are missing in the comparison with the simulated muon tracks in figure V.5(a). For the other lengths simulation and data agree well except for small peaks in the reconstructed data around 6.5 m. As neither V.4 nor V.5(a) show these peaks and the agreement with the other distribution is good, this peak is most likely a reconstruction failure.
To check if also the reconstructed tracks are caused by minimal ionizing particles, events which were reconstructed as going through the veto top and bottom region with a minimal charge deposition of 50 kDUQ were selected. In figure V.6(b) their charge to track length relation is plotted. It fits well to minimal ionizing particles if a broadening effect due to the geometry of the IV is taken into account. A fit with a convolution of a Landau function and a Gaussian yields a specific charge per track length loss of $dCh/dX = 2859 \pm 2\,\mathrm{DUQ/cm}$. This can be compared to the value of $2848 \pm 5\,\mathrm{DUQ/cm}$ from [Die13]. For the latter the RecoMuHam algorithm was used to calculate the track length in the IV. As both values agree well, the reconstruction algorithm deliver similar results.
With the results of the specific energy loss of muons a charge to energy conversion factor can be calculated:

$$c = \frac{dCh/dX}{dE/dX} = \frac{2859 \pm 2\,\mathrm{DUQ/cm}}{1.749\,\mathrm{MeV/cm}} = 1635 \pm 1\,\mathrm{DUQ/MeV}.$$

Figure V.7(a) shows the resulting energy spectrum. For larger amounts of deposited energy the spectrum looks quite similar to the data in figure V.1. Here, two peaks are visible, but the second peak has a step at 200 MeV. Note that the spectrum is given as a function of deposited energy. As the simulation can also account for scintillation, light propagation and detection, a photo electron spectrum can be obtained. Plotted in figure V.7(b), one peak vanish and only a single broad peak occur.
Figure V.8(a) shows the deposited energy by muons separated by the IV-track length in four categories corresponding to the four peaks in V.5(a). These are length less than one meter, between 1.0 and 1.4 m, between 1.4 m and 2.0 m and more than 2 meter in the Inner Veto. In figure V.8(b) the same was done for the PE distribution.
Consequently the peaks in the energy distribution in figure V.7(a) occur due to different track lengths. Taking into account the results of the muon track simulation in figure V.8(a) it can be concluded that the first peak corresponds to once crossing muons, while the second is a set of twice crossing muons, through top and bottom or top and side respectively side and bottom.
For the PE distribution the situation is a bit different. The peak occur due to twice crossing muons like for the energy distribution, while the PE distribution caused by once crossing muons is too broad to produce a peak.
To understand why the PE distribution in the simulation has only broad peak instead of the two peaks for deposited energy and data, another muon simulation was performed. To speedup the simulation it is possible to reduce the amount of produced photons in

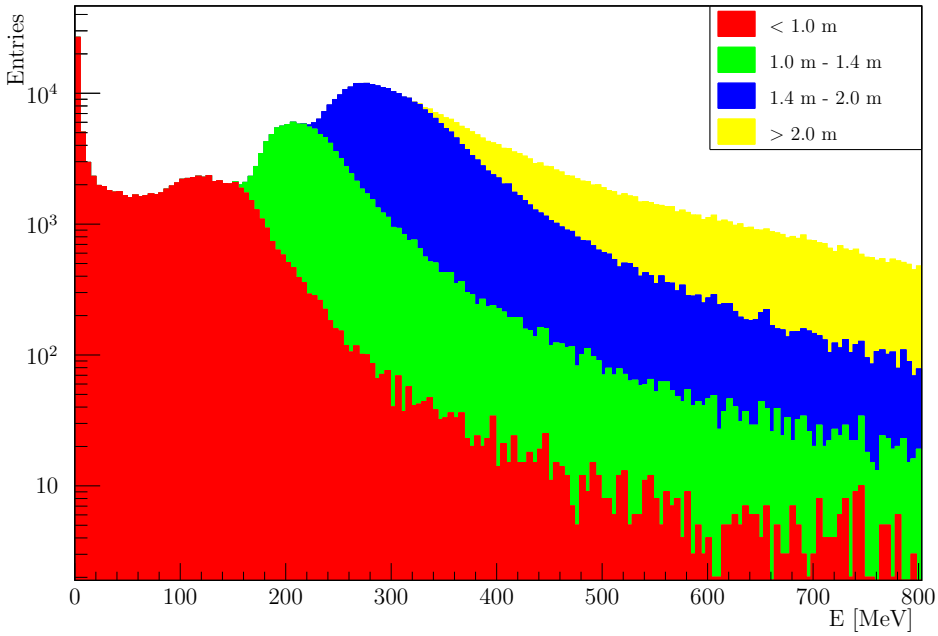

(a) Deposited energy

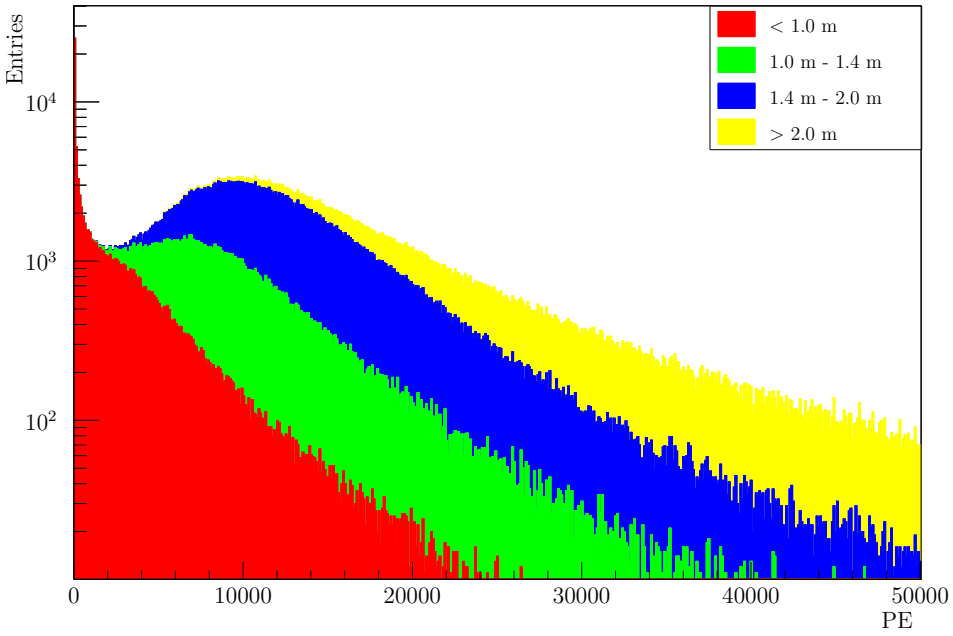

(b) Photo electrons

Figure V.8: The deposited energy (top) and PE distribution (bottom) separated by the muon track length. In red muons with track length smaller than one meter, in green track lengths between 1.0 and 1.4 m, in blue between 1.4 and 2.0 m and in yellow above 2.0 m.

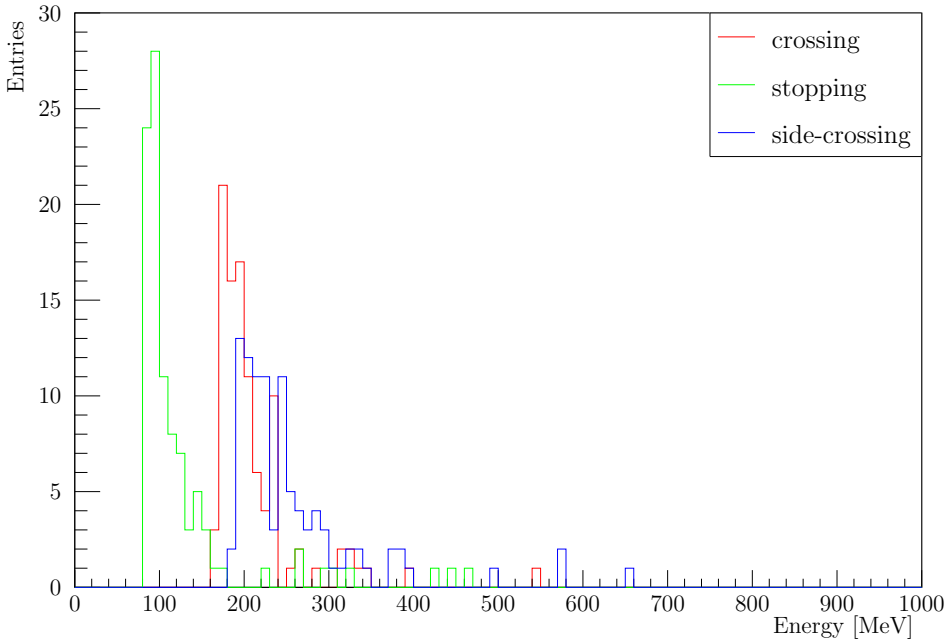

(a) Energy distribution

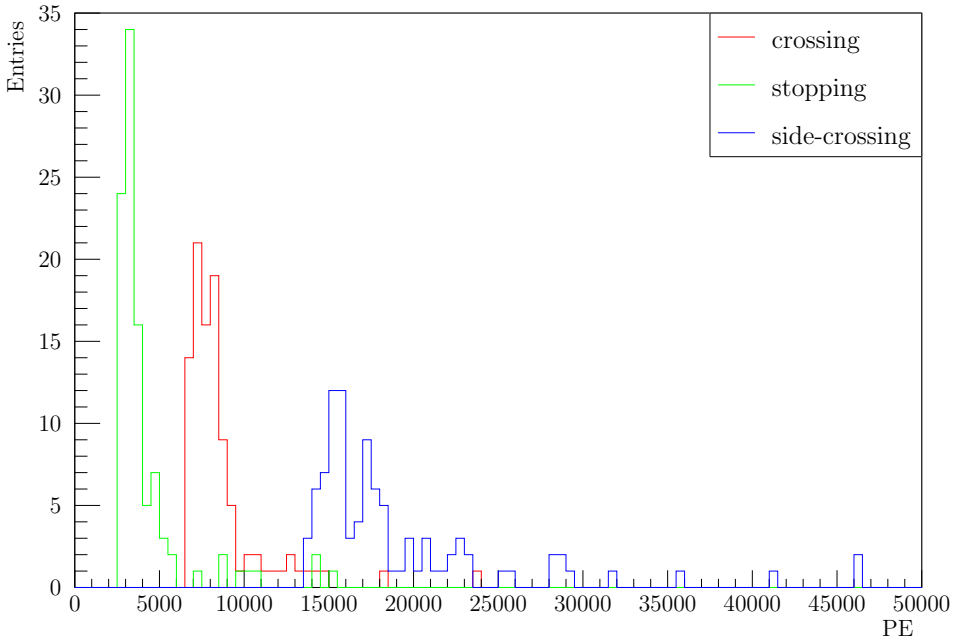

(b) Photo electrons

Figure V.9: Energy (top) and PE (bottom) distributions of simulated muons without photon weighting. Three types with 100 muons each were started: Crossing (red), stopping (green) and side-crossing (blue) muons.

the scintillator up to a given threshold. To account for the real amount of photons each simulated photon is weighted by the factor produced photons divided by simulated photons. This photon limitation was used in the muon simulation above. A simulation was started without a photon limitation. Here three types of muon events were studied and propagated 100 times through the detector:

- Crossing muons: Muons coming directly from above (starting point: (1000 mm, 0 mm, 4000 mm, propagation vector (0,0,-1)) in laboratory coordinates (see section 2 in chapter VI)) which cross the top and bottom region of the veto.
- Stopping muons: Muons which cross the IV only once. Here the muons were started in the target at (0 mm, 1000 mm, 0 mm) and propagated directly upwards (0,0,1).
- Side-crossing muons: Muons which cross top and side part of the IV. The starting point was (2000 mm, 2000 mm, 4000 mm)) and the direction diagonal downwards (-1,-1,-1).

In figure V.9(a) and V.9(b) their deposited energy respectively PE distributions are plotted. The crossing muons deposit twice the amount of energy and hence produce twice the amount of PEs in the IV than the stopping muons. The side-crossing muons are a bit different. Their energy depositions are in general a bit higher than the crossing muons, but they produce almost twice as much PEs. The origin for that behaviour is the chosen path: The side-crossing muons pass two PMTs, one in the top region, one lateral, very near to its photo cathode. Therefore more produced light can be detected.
As it is visible in figure V.9(b) stopping and crossing muons produce single, distinguishable peaks. Thus the absence of the second peak muon in the simulated PE spectrum (figure V.7(b)) occurs most likely due to the photon weighting in the muon simulation. With this knowledge it is possible to make a charge to energy and a charge to PE conversion. To the described peaks in figures V.1, V.7(a) and V.7(b) Gaussian were fit and their central values taken to determine the peak position. As the fit errors were very small (in the order of 10 DUQ, 0.5 MeV respectively 10 PE) 10 kDUQ, 10 MeV and respectively 100 PE were taken conservatively. For zero energy deposition also no charge output was assumed (see the following section 4 for details). Afterwards a linear function of the form $y = c * x$ was fit to these data points with c as the conversion factor (see figure V.10). The results are

$$\begin{aligned} c_E &= 1620 \pm 61\,\text{DUQ/MeV and} \\ c_{PE} &= 19.8 \pm 1.0\,\text{DUQ/PE.} \end{aligned}$$

Due to the geometry and the distribution of the IV PMTs, same energy depositions in different places will lead to different amounts of detected photo electrons (see [Die12]), so this conversion factors will be an estimate. Also saturation effects which can occur at high deposited energies were not taken into account.

The conversion factor c_E can be compared to the similar conversion factor which was calculated above by comparing the specific energy loss in the simulation and in data and was found to be 1635 ± 1 DUQ/MeV. Within the error bars both values match very well. The factor c_{PE} can be seen as the gain of the PMTs. The actual gain measured with the IV light injection system (presented in section 1.3 in chapter IV) is around 140 DUQ/PE. This factor 7 difference can be understand if two facts are taking into account: First, in the simulation the saturation of the PMTs was neglected. For the first PE the relation to the flowed charge on the FADC is almost linear while for more PEs the flowed charge is limited by a saturation threshold and the range of the FADC. Second, no time cut was used while the FADC have a time window of 256 ns. Thus in the simulation PEs which arrive after the 256 ns are counted, while in the data are not recognized as long as the detector is readout and is not ready to trigger a new event.

3 The Double Chooz Inner Veto triggering system

Like it is described in section 6.3.1 in chapter III, the Double Chooz data acquisition system consists of two individual subsystems: one for the Inner Detector and one for the Inner Veto. Both have several trigger types. The most common is the physics trigger. If an event deposits more charge than the particular trigger threshold in one of the two sub-detectors, the event is recorded in any case.
Additionally there is the prescaled trigger. This type has an own trigger threshold, which is lower than the normal trigger. In contrast to the normal trigger, the prescaled trigger is recorded only on each thousandth trigger to look for possible trigger failures.
The first threshold, that is reached, is logged as recording trigger except for not recorded prescaled triggers. Later reached thresholds are ignored. During the first years the readout of the Inner Veto had a time delay with respect to the one of the Inner Detector. Most events, which deposited energy in both detector volumes, were therefore logged as recorded by the Inner Detector trigger.
Trigger effects are the origin for the two peaks in the lower charge region of the charge spectrum shown in figure V.1. To show this, the spectrum needs to be divided into the trigger type, which recorded the event. This was done in the figures V.11 and V.12. The charge spectrum recorded by the Inner Detector physics trigger is shown in figure V.11(a). Due to the time delay between both sub-detectors, it contains the events which deposited energy in bot ID and IV. Here the two higher charge peaks are more prominent which is another hint that they occur due to crossing and stopping muons as discussed in the section above. The sharp decline for lower charges are mostly random coincidences with non-related energy depositions in the Inner Detector and reflects the trigger-less spectrum of the Inner Veto (see section 4 for details).
The events in the charge spectrum shown in V.11(b) are triggered by the physics trigger of the Inner Veto. The spectrum contains only few events for low charges and rises then very steeply to a very prominent peak at around 36 kDUQ with a sharp decline afterwards. This peak represents the trigger threshold. As the triggering process is more complicated

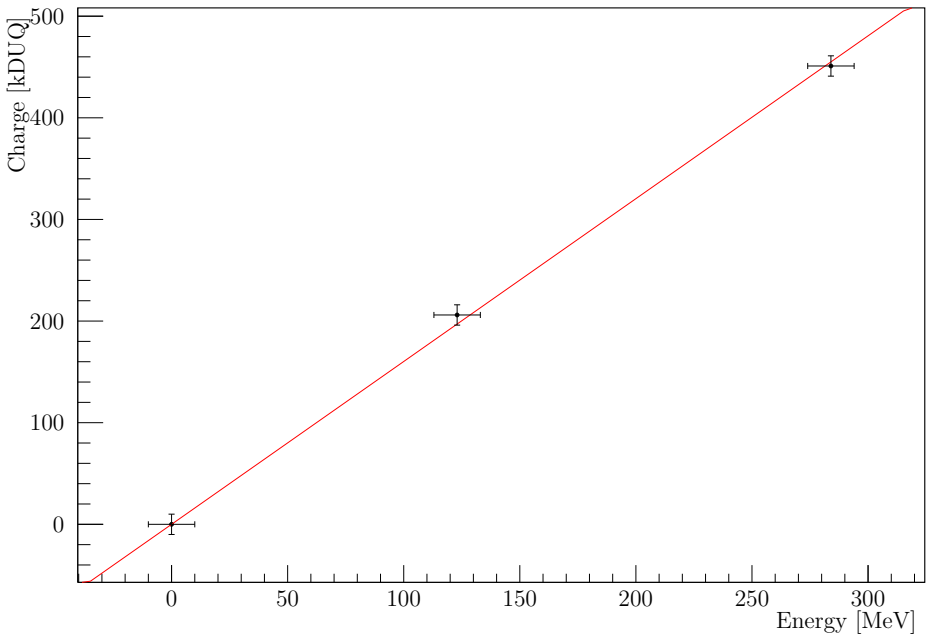

(a) Energy

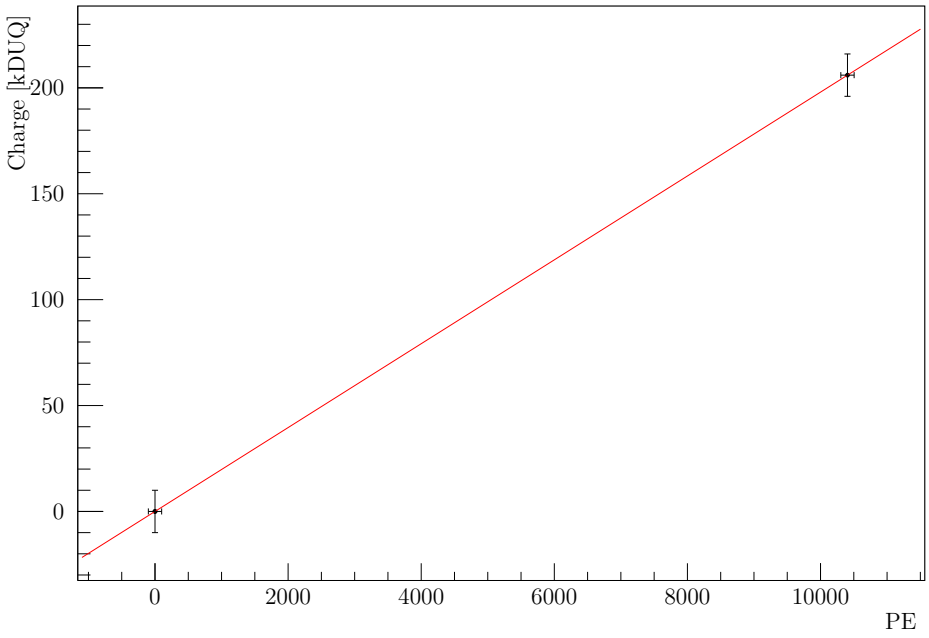

(b) Photo electrons

Figure V.10: Charge to energy (top) and charge to PE correspondence (bottom). The positions of the peaks are marked as well as the origin.

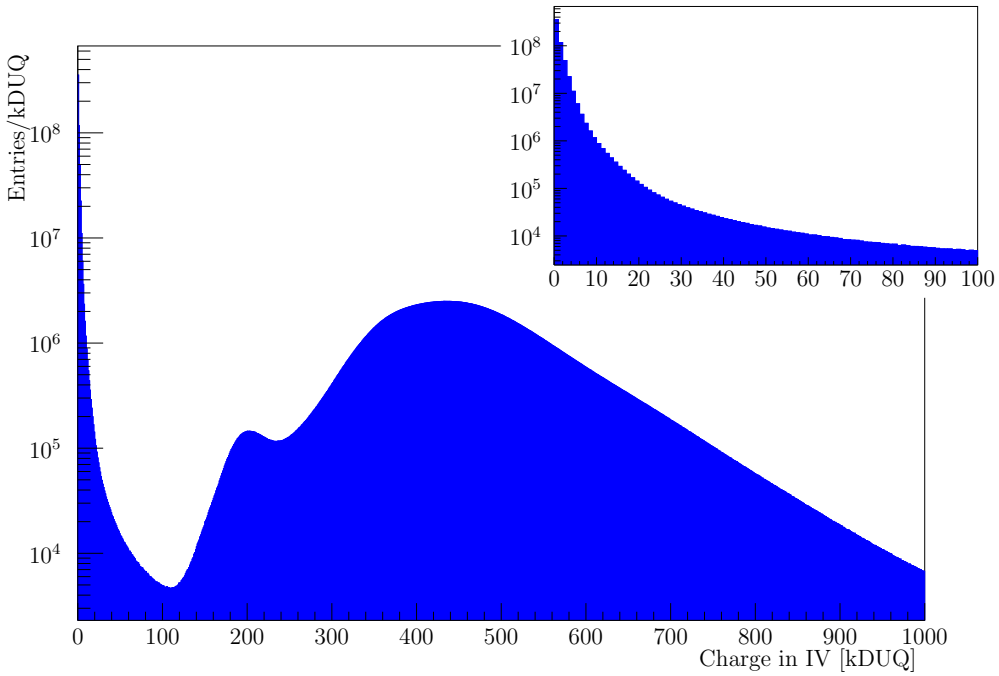

(a) Physics trigger ID

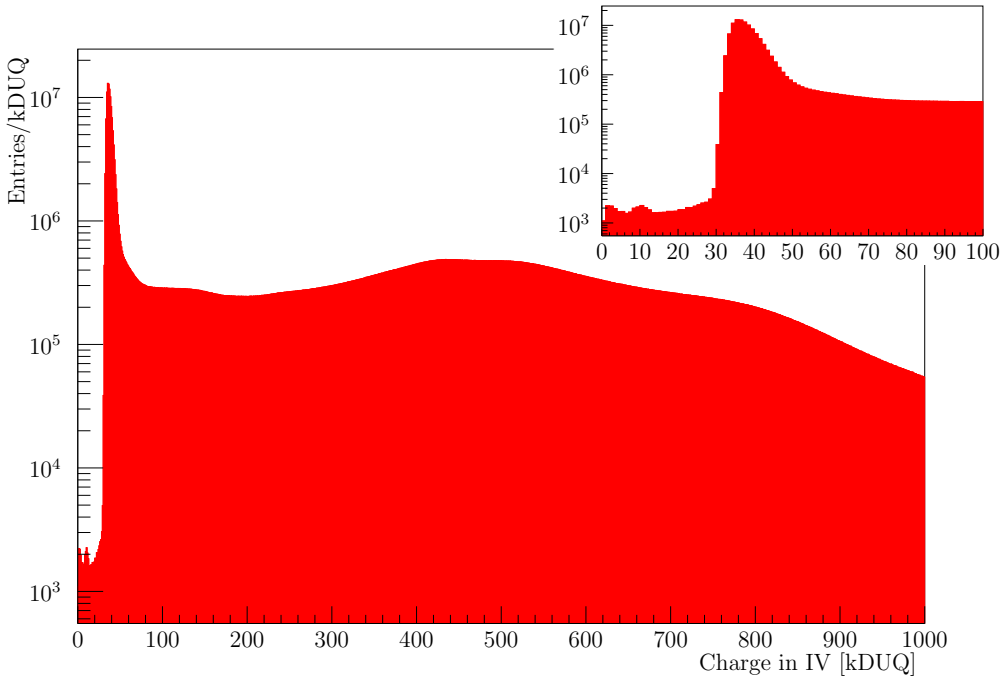

(b) Physics trigger IV

Figure V.11: Measured charge spectrum in the Inner Veto with cut on recording ID/IV physics trigger. In the upper right corner a zoom into lower charge region is shown.

than just a charge threshold (see section 6.3.1 in chapter III), there are also events below this threshold, but for most of the cases the charge threshold is a very good simplification. The charge spectrum for higher charges is almost flat, there is only a very complanate and broad peak between 400 and 500 kDUQ. This is most likely caused by muons which cross the veto, but not the Inner Detector. Otherwise they would have been recorded by the Inner Detector physics trigger, which always occurred earlier due to the mentioned time delay.
Almost the same can be found for the two prescaled trigger spectra shown in figure V.12. The peak, which occurs in the Inner Veto prescaled trigger spectrum at around 16 kDUQ, is the trigger threshold of the Inner Veto prescaled trigger. As the prescaled trigger is recording each thousandth event, regardless if other thresholds were taken, the spectrum of the prescaled Inner Detector trigger is almost identical to the Inner detector physics trigger and equal for the higher charges of the prescaled Inner Veto trigger. These trigger-separated spectra can be plotted in one common figure. This has been done in V.2. It is clearly visible that the two peaks in the lower charge spectrum occur due to the trigger thresholds of the Inner Veto physics trigger and the prescaled trigger respectively. The prescaled threshold lies at around 16 kDUQ, which translates to 10 MeV using the conversion factor derived in section 2.2, while the normal trigger threshold is at 36 kDUQ, corresponding to 22 MeV deposited energy.
This means that any energy deposition below 10 MeV is only recorded, if there is also an energy deposition in the Inner Detector above its trigger threshold. The same is true for each thousandth event, which deposits more than 10 but less than 22 MeV in the veto without triggering the Inner Detector.
It is also possible to find a threshold in the amount of fired PMTs for events triggered by the IV physics trigger. In figure V.13 the amount of fired PMTs is shown, when the event was recorded by the Inner Veto trigger. A hit means, that charge > 0 DUQ[1] was detected by the PMT. Like the charge spectrum of the Inner Veto trigger in figure V.11(b) it begins with a steep rise and a peak at around 25 PMT hits. Thus, the trigger threshold for the IV physics trigger lies at 25 PMT hits.

4 Dead Time Monitor studies

As described in section 6.3.1 of chapter III the Dead Time Monitor is a special trigger type, which is applied around twice a second and reads out the detector independently from any charge threshold. With this trigger type events with a sub-threshold charge can be investigated. In that charge regions events caused by radioactive decays of impurities in the veto and dark noise effects of the PMTs will be dominant.
For this study $\sim 8 \cdot 10^7$ events triggered by the Dead Time Monitor were analysed. This corresponds to a detector lifetime of 500 days. In 5.3 % of these events an energy deposition (> 0 DUQ) was seen in the Inner Veto. So in 95 % of the time the detector was quiet, so no charge deposition can be found.

[1]Due to the digitisation of the waveform the smallest amount of reconstructed charge is 6 DUQ.

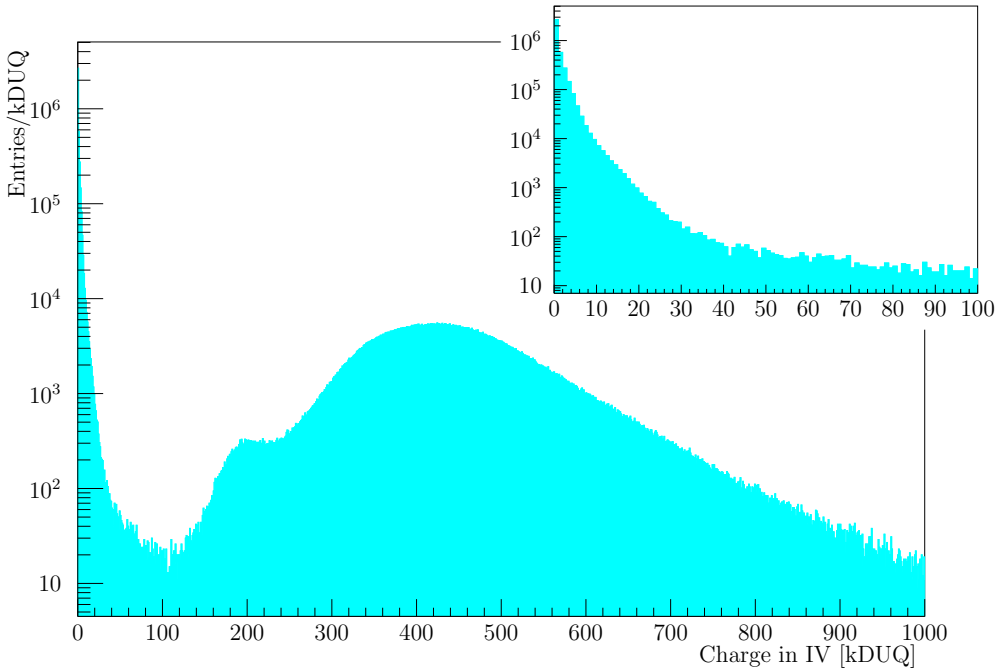

(a) Prescaled trigger ID

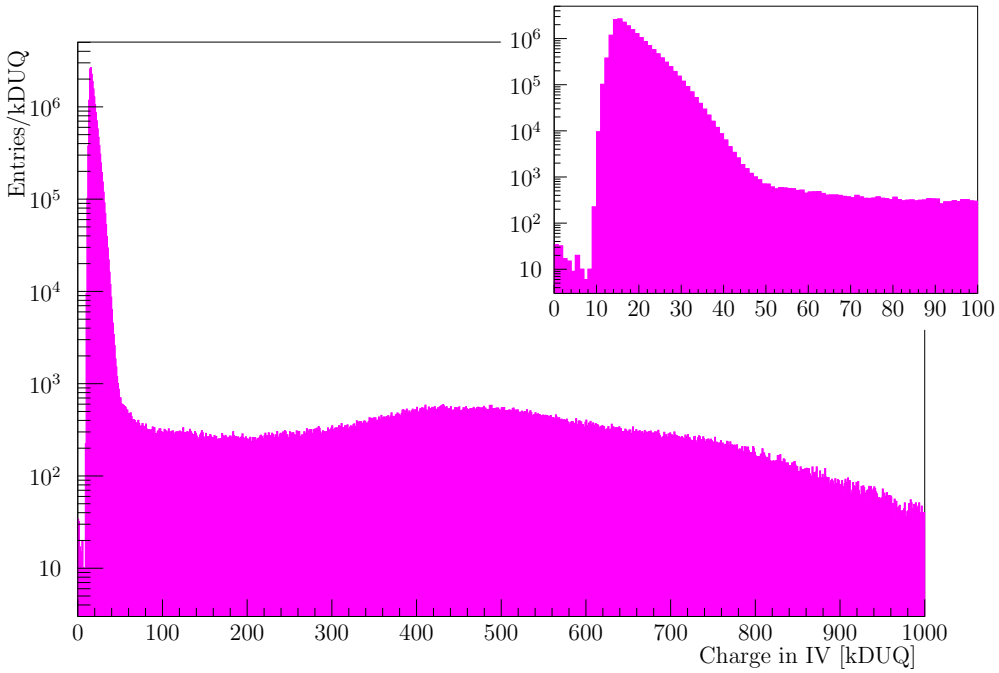

(b) Prescaled trigger IV

Figure V.12: Charge spectrum in the Inner Veto separated by recording IV prescaled trigger for the upper plot and ID prescaled for the lower. In the upper right corner of both figures a zoom into lower charge region is shown.

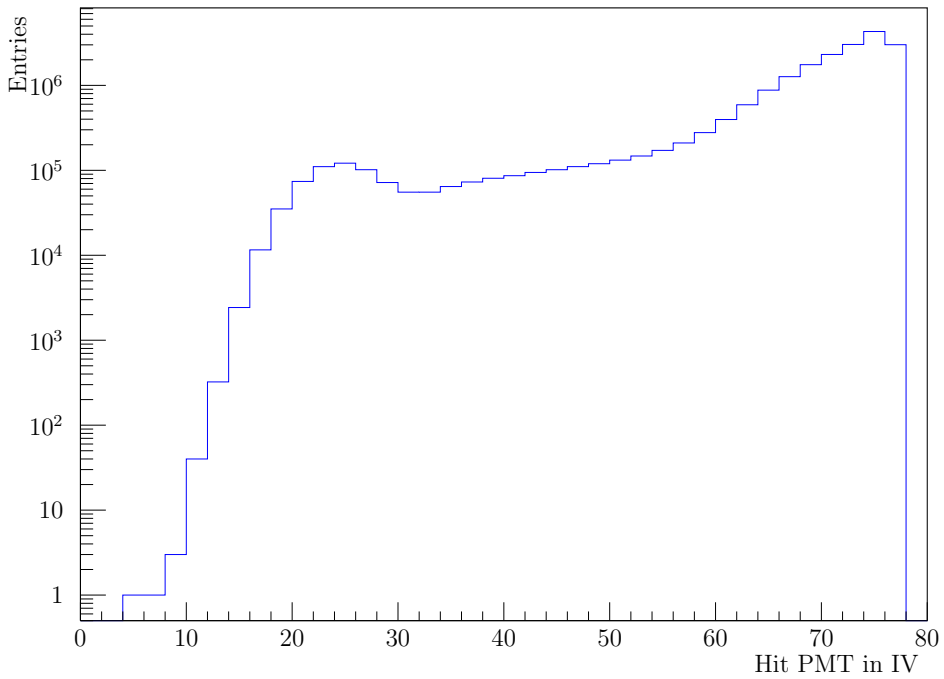

Figure V.13: Amount of hit PMTs, when the Inner Veto triggered.

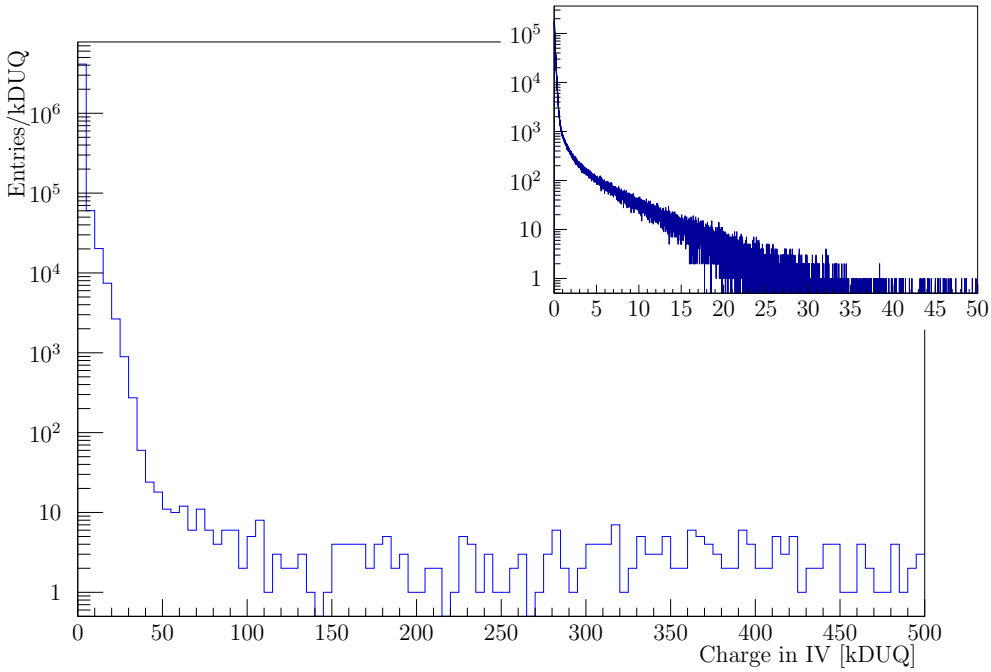

Figure V.14: Charge spectrum of the Inner Veto triggered by the Dead Time Monitor. In the upper right corner a zoom into low charge region is shown.

In figure V.14 the recorded charge spectrum is shown. Beginning from zero charge it shows a very steep decline with a kink at 1 kDUQ, where the spectrum becomes harder. At charges higher than 40 kDUQ the spectrum is flat and the statistic is very low. This can be understood as in this charge region the events are most likely muons with a track. Therefore their energy deposition is protracted in the order of 10 to 100 ns. As the Dead Time Monitor triggers randomly with a longer time of energy deposition the probability is rising that not all of it is recorded by the trigger and only a part of it is seen. Larger energy depositions are therefore suppressed to lower charge depositions.
These events can be classified by the amount of PMT hits: It is useful to consider events with only one hit PMT and events with more than one hit. In figure V.15 it is clearly visible, that the events with a single PMT hit are responsible for the peak at low charges, while beginning at the kink position events with multiple PMT hits are dominant.
Events in the scintillator are in most cases not fixed at a special location and can occur anywhere within the volume. Therefore the chance that their light is seen by just one PMT is quite low. Dark noise events happen inside the PMT and are in most cases invisible for other PMTs, with encapsulated PMTs like in the IV even more. Especially for low charges most of the signals are very likely dark noise events. So the peak for low charges can be understood as dark rate of the PMTs, while the less steep inclination arises due to events related to radioactivity in the detector volume.
This radioactivity is induced by impurities in the veto scintillator like uranium, thorium

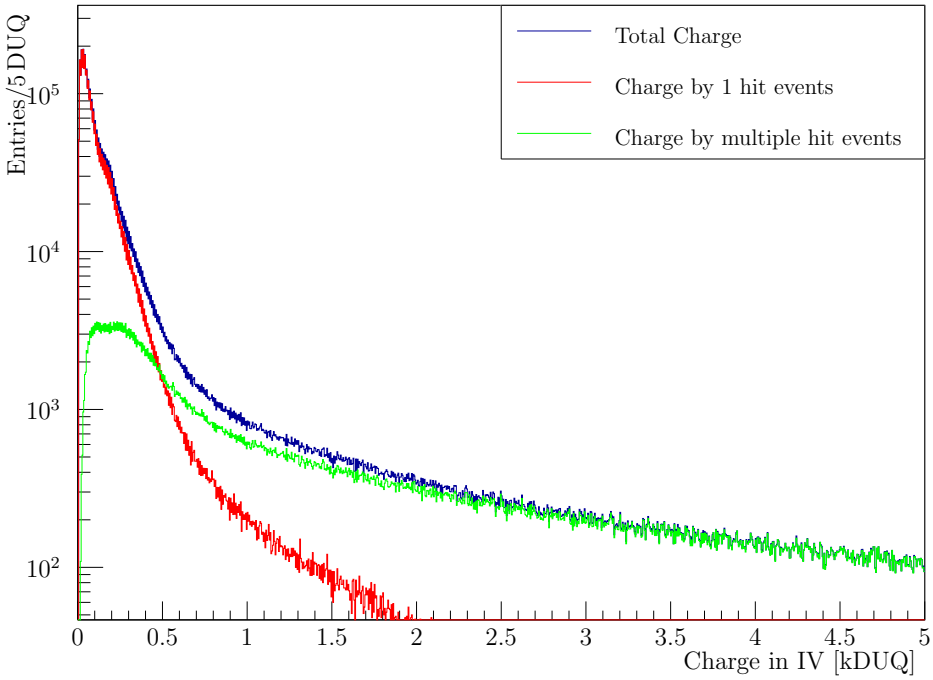

Figure V.15: Charge spectrum recorded by Dead Time Monitor classified into 1-hit and multiple-hit events.

and potassium in the glass of the PMTs as well (see [Gre14] for details).

5 The Inner Veto trigger rate

With the charge spectra discussed in the section 3 and 4 above it is trivial to compute the rate of events at a given trigger threshold. For this the events at the threshold and above must be summed and divided by the measuring time. The detector live time can be determined by counting the amount of fixed rate trigger events, which are taken once per second (see 6.3.1 in chapter III).
Figure V.16 shows the rate of events for a given threshold. In total, events with a charge deposition in the IV are recorded with a rate of 75 events per second. At the muon tagging threshold for the Inner Veto of 30 kDUQ used in [DCC14] the rate is found to be 45 muons per second.

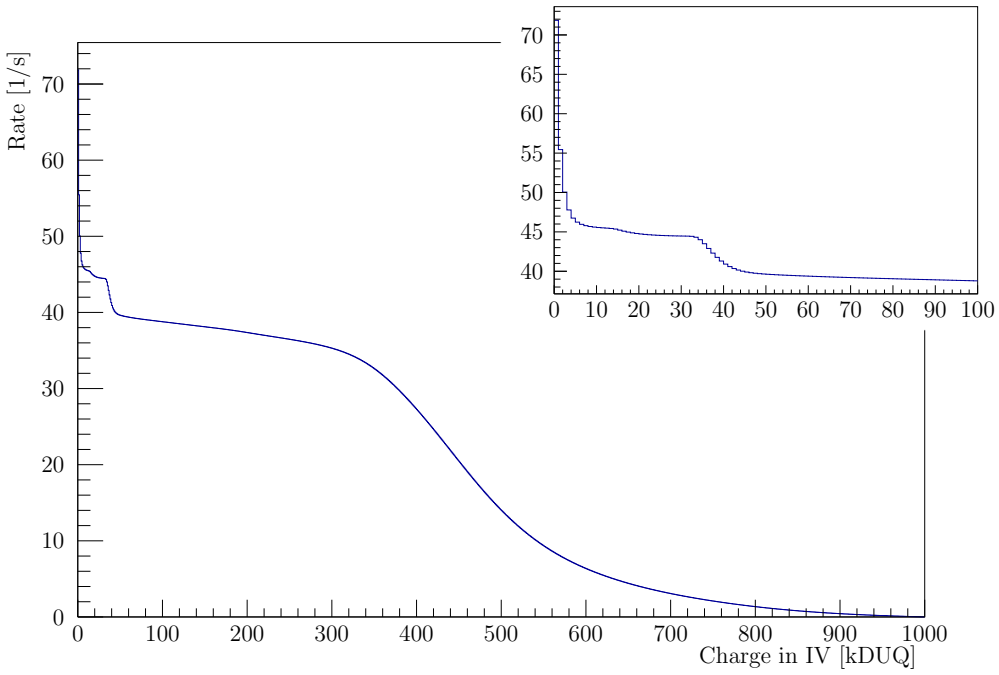

Figure V.16: Rate of events in the IV as a function of threshold in kDUQ. In the upper right corner a zoom into lower charge region is shown.

For the spectrum recorded by the Dead Time Monitor a rate calculation is possible as well. As a first step the rate is computed in the same way as for the normal spectrum. Then the rate must be scaled by the factor $1/S_{DM}$ with

$$S_{DM} = 256 \cdot 10^{-9} \cdot (DM)^{-1}[\text{s}],$$

where DM are the amount of Dead Time Monitor trigger events in the measuring time. The value of 256 ns is the recording time window of the DAQ. S_{DM} can be seen as the

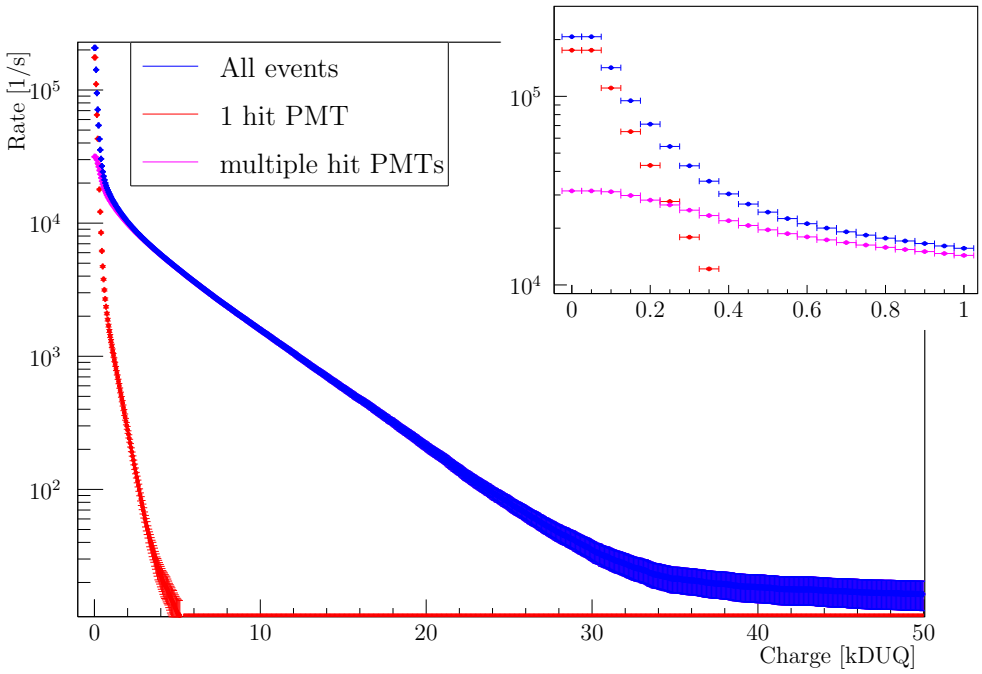

Figure V.17: Rate of Dead Time Monitor events (in blue) with error bars as a function of threshold in kDUQ and scaled to absolute numbers. Also shown are the events with one (in red) and multiple (in magenta) hit PMTs. In the upper right corner a zoom to lower charges is plotted.

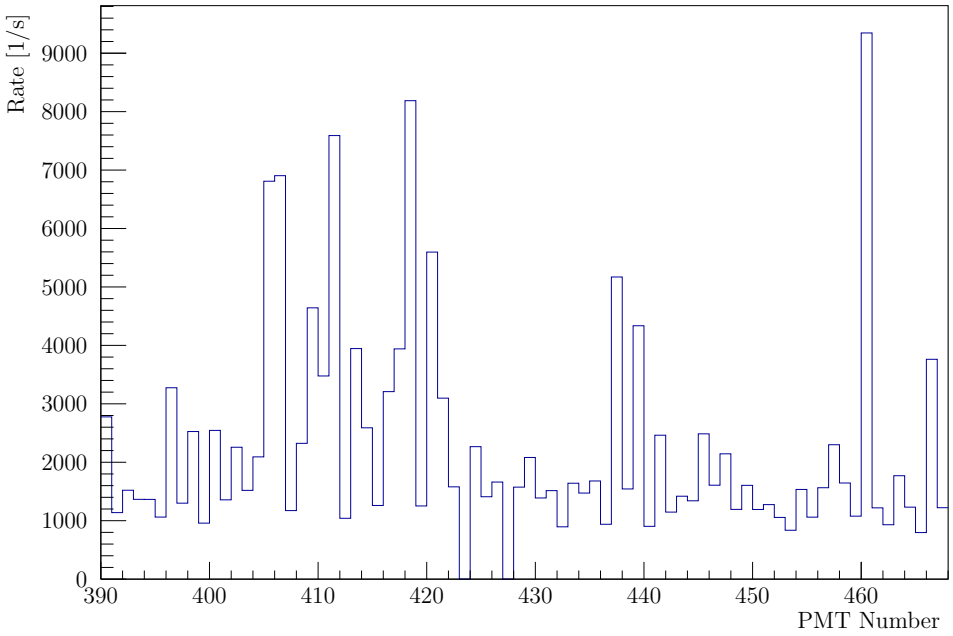

Figure V.18: Distribution of the events with just one PMT hit per PMT. In mean 2308 counts per second were measured per PMT.

time, which the Dead Time Monitor has recorded.
Figure V.17 shows the scaled rate with error bars. The assumed error is $\sqrt{N}$, where N is the amount of events scaled by S_{DM}. As can be seen in figure V.14, for events with higher charges statistics are very low. Events with 30 kDUQ or more occur at a rate of 36 ± 6 events per second, which corresponds to the rate in figure V.16.
The absolute rate of events is on the order of $2.2 \cdot 10^5$ events per second (blue line). As discussed above it is possible to divide the Dead Time Monitor events in two components: The first with 1 hit PMT, the second with multiple hit PMTs. The first results in around $1.8 \cdot 10^5$ events per second (red), the second in around $3.2 \cdot 10^4$ events per second (magenta). The rate for one hit PMT is most likely due to dark rate in the PMTs. To prove this the events were distributed to the PMT which was hit. In figure V.18 this is plotted. It is a broad distribution, but none of the PMTs has an extremely high rate. In mean each PMT has 2308 counts per second. This can be compared to measurements of the dark rate done in Tübingen before the installation. Here the mean dark rate was around 2000 events per second. Thus the majority of the one hit PMT events are PMT dark noise. A possible pile up with this dark noise rates results in around one event per second. The remaining difference of the before measured rate of dark noise and the events with one hit PMT of 300 counts per second and PMT is seen as radioactivity of the PMT glass. If the multiple hit PMT are taken as radioactivity in the veto, the total rate of radioactivity in scintillator and PMT glass is around $5.5 \cdot 10^4$ events per second with a threshold of $0 >$ DUQ. This

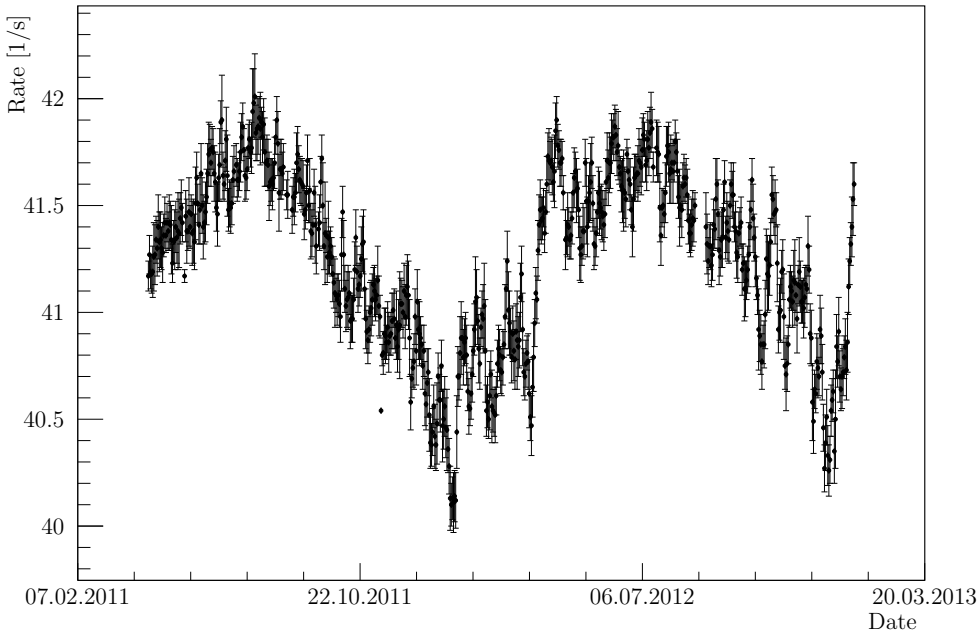

Figure V.19: Variation of the muon rate in the Inner Veto due to seasonal effects.

can be compared with [Gre14] were $1.0 \cdot 10^5$ events per second were postulated. Thus the IV is cleaner than expected.
As a last point it should be mentioned that the rate of events in the Inner Veto is also time-dependent. Depending on the season, and therefore on the mean air temperature profile the atmospheric density varies. In winter the gas atoms have less kinetic energy and the atmosphere is therefore more compact and less high than in summer. Muons which are reaching the ground are more energetic in summer. As the low energetic part of the muon spectrum does not reach the detector, more muons are observed in summer than in winter. Figure V.19 shows this variation over a period of two years. The variation is explained in detail in [Die13] and [DCMu]. As the amplitude is on the order of a few percent, this variation does not affect the rates discussed above.

6 Conclusion

In this chapter the spectrum of the Inner Veto has been discussed. It was shown, that the observed peaks in the spectrum occur due to trigger effects and due to the geometry of the veto. Selecting a special trigger the spectrum can be investigated below the standard trigger threshold. It could be shown that the total rate of events at zero threshold is around 200,000 events per second and arises mostly due to dark noise in the PMTs. The total rate

of radioactive decays could be estimated to be around 50,000 events per second. With the help of muon simulations rough conversion factors for charge and energy (c_E) and charge and photo electrons were found to be

$$\begin{aligned} c_E &= 1620 \pm 61\,\mathrm{DUQ/MeV} \\ c_{PE} &= 19.8 \pm 1.0\,\mathrm{DUQ/PE} \end{aligned}$$

VI
Muon angular distributions

In this chapter the reconstructed angular distribution of muons crossing the far detector will be compared with the angular distribution of simulated muons generated with the help of the MUSIC code.

1 Muon reconstruction algorithms

When a muon crosses the detector, it deposits energy in the scintillator. Due to the energy deposition the scintillator emits light, which will be detected by the PMTs. To reconstruct muon tracks from PMT hit information two algorithms are used within Double Chooz.

1.1 RecoHam

The RecoHam reconstruction was programmed by Michael Wurm, at this time at the university of Hamburg[Wur13]
RecoHam is a muon track reconstruction algorithm based on the timing of the PMT hits. The first hit PMT is assumed as the entry point of the muon. Based on the entry point coordinates for each hit PMT the time difference Δt is calculated by subtracting the PMT hit time t_{hit} by the time t_{tof} the muon has to travel to the PMT, thus $\Delta t = t_{hit} - t_{tof}$. The lowest time difference is chosen as exit point.
Based on this two point the most likely light arriving times for each PMT is calculated assuming a perfect cone shape of the emission. This times are compared with the measured ones. By a variation of the entry and exit point the differences between measured and predicted hit times is minimized[Wur13].

1.2 FIDO

FIDO stands for "Fused Inner Detector/veto and Outer veto muon reconstruction". It was written by Matthew Strait.
FIDO uses the information of all three sub-detectors of Double Chooz: the Inner Detector, the Inner Veto and the Outer Veto. The Outer Veto gives a position information for passing muons (see section 6.2.2.2 in chapter III for details). For the both other volumes a similar algorithm as for RecoHam is used two find the entry and exit points in the respective volumes. At the end the reconstructed track is found by a χ^2-fit minimisation. The χ is calculated from the PMT start times and their associated errors. For details see [DCM14].

2 Laboratory coordinate system

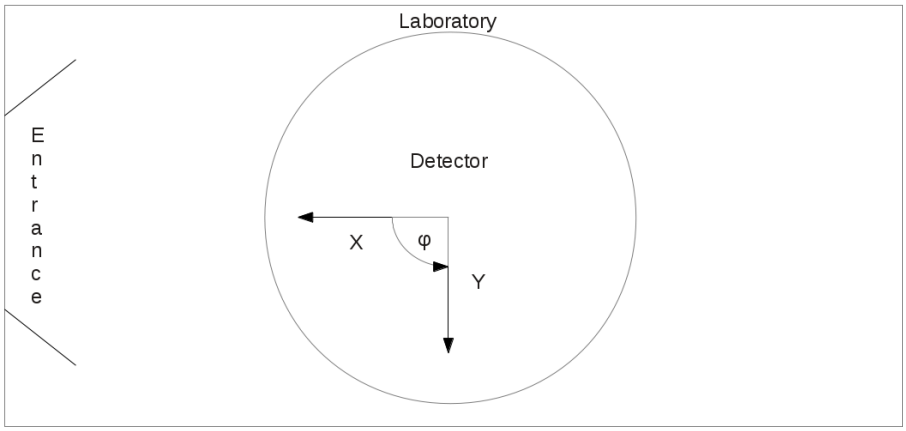

Figure VI.1: Sketch of the used coordinate systems in the two laboratories.

Both laboratories have its own coordinate system, which is based on reference points in the laboratories. The origin of the system is the central point of the detector, i.e. on half height and half diameter. The z-axis is given by the symmetry axis of the cylindrical shaped detector. Orthogonal to this axis the line from the central point into the direction of the entrance of the laboratory is defined as the positive x-axis. The y-axis is orthogonal to both other axes and orientated using the right-hand rule. Figure VI.1 shows a sketch of the coordinate system and its orientation in the laboratories.

3 Comparison between data and Monte Carlo

For this study the same data used in [DCC14] were analysed. An event was treated as a muon, if either more than 50 kDUQ were deposited in the IV or more than 200 MeV in the ID. These cuts are harder than the ones used than for the neutrino search, as for the neutrino search every potential muon should be neglected, while for this study a pure muon

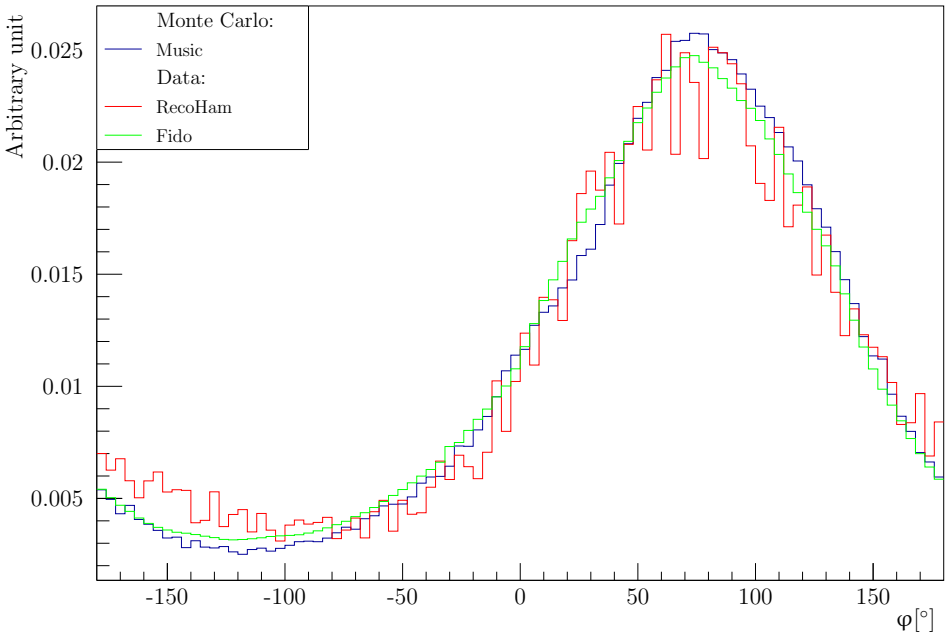

(a) Azimuth angle φ distribution

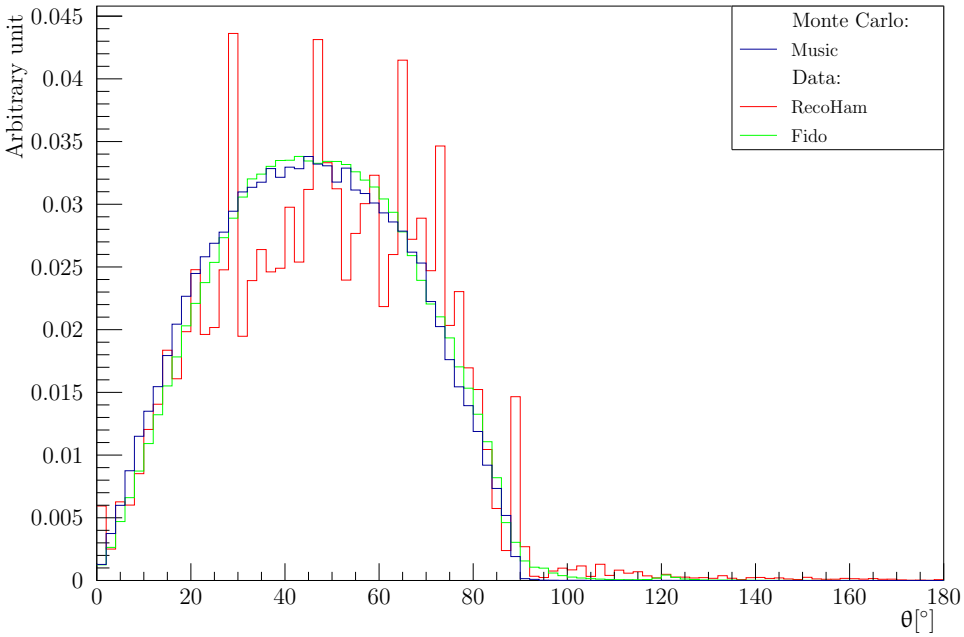

(b) Polar angle θ distribution

Figure VI.2: Distribution of the azimuth angle φ and polar angle θ simulated by MUSIC and reconstructed by RecoHam and FIDO.

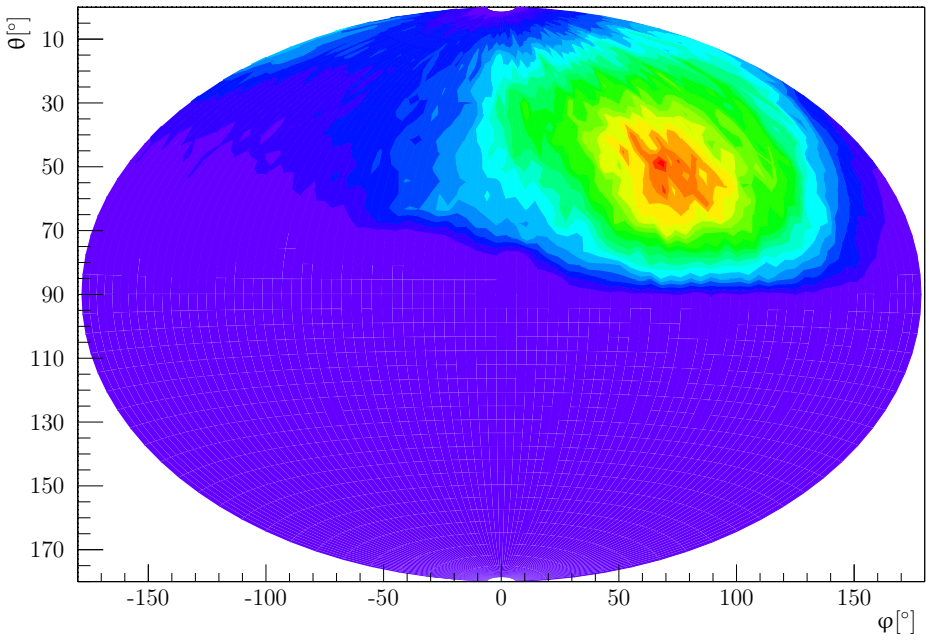

Figure VI.3: Distribution of φ and θ simulated by MUSIC.

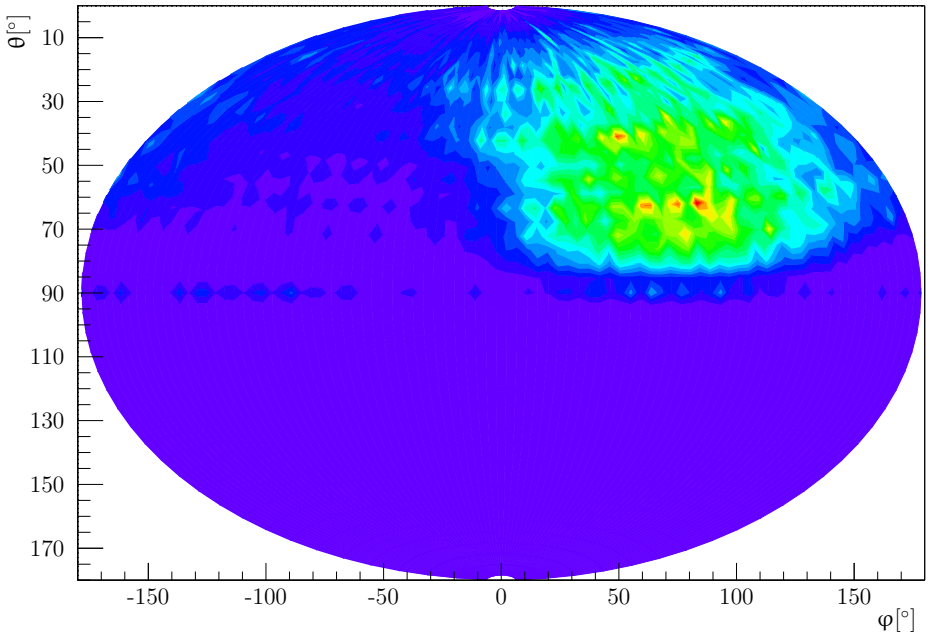

Figure VI.4: Distribution of φ and θ reconstructed by RecoHam.

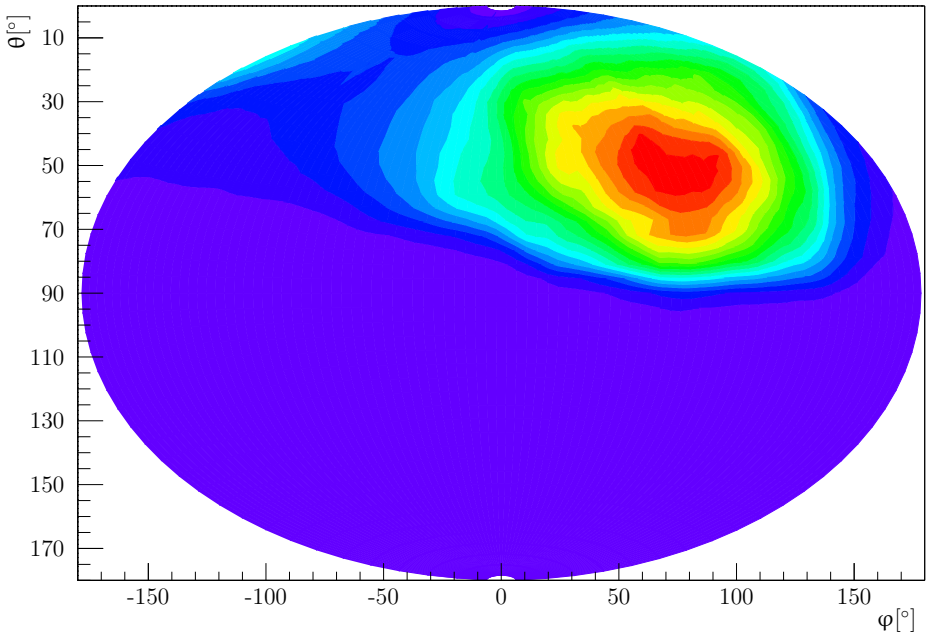

Figure VI.5: Distribution of φ and θ reconstructed by FIDO.

sample is needed. For all selected events both reconstruction algorithms were applied and the resulting angular distributions compared. The angular distribution of 200,000 muons simulated by MUSIC was studied as well. The two examined angles are the polar angle θ and the azimuth angle φ. All data was filled in histograms, which were normalized to contain the same number of entries.
Each code uses an own coordinate system. These systems share the same z-axis, but their x-y-axes are rotated to each other. Therefore the φ-angle distributions need to be corrected for the rotation. For this study the coordinate system of the RecoHam algorithm was used as reference as its utilizes the laboratory system (see section 2 for details).
Each of the distributions shows a peak. This was fitted with a Gaussian and the centre values compared. As result, the MUSIC results are rotated by +34 °, while the FIDO results have a rotation of -30 °. The origin of the rotation of the MUSIC results is that the used MUSIC coordinate system is north-orientated. This is approximately the same angle as the x-y frame is rotated in figure VI.6, which is north-orientated. The origin of the rotation of the FIDO results in comparison to the RecoHam results is not known.
In figure VI.2(a) the corrected φ distributions are plotted. With the correction the simulated results agree well with the measured ones. The RecoHam result has some reconstruction artefacts. All show a nearly identical angle distribution, in which the φ-angle distributions show a peak around 90 °. This can be understood by remembering the detector site location. Figure VI.6 shows a satellite image of the hill under which the far detector was built. The laboratory and its coordinate system is sketched into it. The positive y-axis

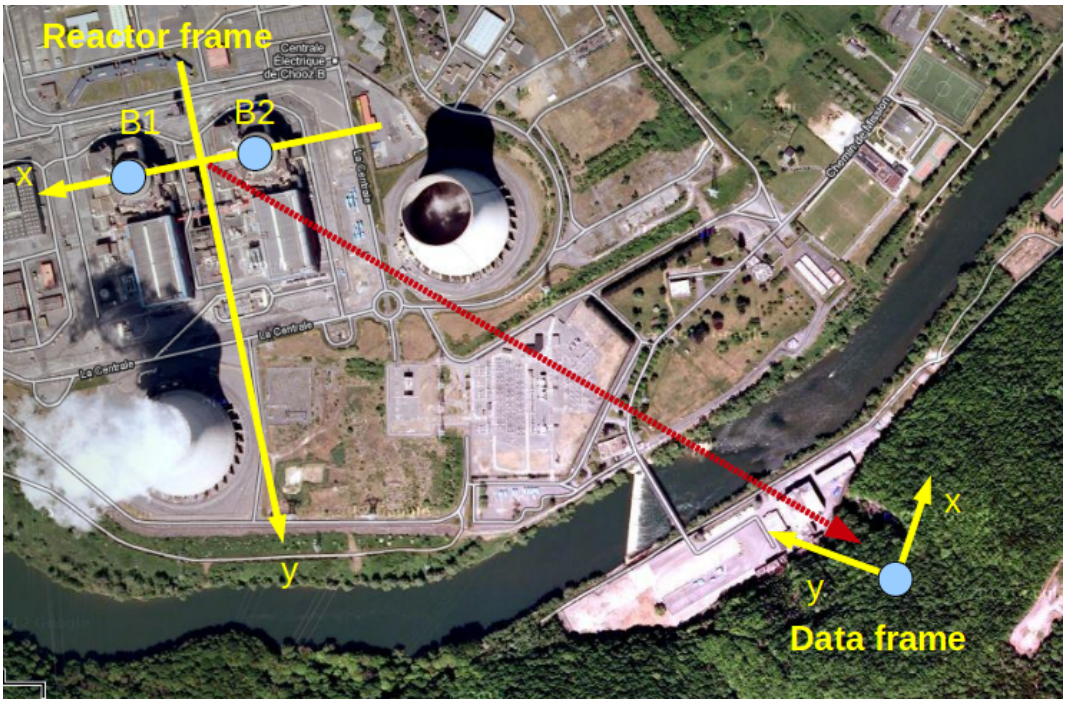

Figure VI.6: Satellite images of the far detector location with marked laboratory coordinate system. The upward direction is looking towards north[Cad13].

is pointing roughly towards the Meuse river. The φ-angle two the both reactor cores are 80° and 87°[Viv13]. As the hills at the Chooz site have typical river valley profile, the hill is in that direction flat near the river and then steeply rising. The laboratory is located beneath this increase and therefore in the direction of the positive y-axis and with it a φ-angle of 90 ° the far laboratory has the least overburden.
The distribution of θ are in good agreement as well as shown in figure VI.2(b). Most of the muons arrive from a angle of around 45 °. As in the φ-distribution the RecoHam result shows reconstruction artefacts.
It is also possible to plot φ and θ distributions in two-dimensional histograms. This was done in the figures VI.3, VI.4 and VI.5. Again all distributions agree well. It can clearly be seen in all three figures, that the majority of the muons is coming from the direction, where the overburden is the smallest.

4 Summary

The angular distribution shows, that the major part of the muons is coming from the direction with the least overburden. The reconstructed muon angular distributions agree very well with the ones simulated by MUSIC. This confirms the result in section 2.2 in chapter V, where the simulated and reconstructed muon track length were compared.

VII
Muon tagging

1 Motivation

When a muon crosses the detector, it deposits a large amount of energy. This happens in form of ionisation leading to scintillation light in target and gamma-catcher, but muons can also fission nuclei. By this so called spallation process parts of the nucleus are knocked out. This process can also lead to the release of neutrons, which is a dangerous background for Double Chooz, as those signals can mimic the signature of an inverse beta decay, if they are high energetic and deposit an amount of visible energy on the same order as the inverse beta decay induced positron in the scintillator during their thermalisation or if they occur in conjunction with an unrelated scintillator signal. Due to the large amounts of light, which is produced by a muon in the scintillator electronic artefacts like overshoots and baseline shifts can occur as the measuring instruments were built to detect small amounts of light.
Therefore the events following a muon are most probably correlated with the muon event and should be excluded from the neutrino search data. The typical time period of correlated events after a muon is determined in this chapter. It is also investigated, if there is a correlation with the deposited energy of the muons. An optimisation was necessary to find the highest background rejection efficiency for the lowest introduced dead time.

2 Basic analysis

To start the studies two samples of inverse beta decays candidates and all muons which occurred within 1 s before those events were collected for both neutron capture possibilities, thus the captures on gadolinium and hydrogen. For the inverse beta decay candidates the

same cuts were used as in [DCC12] and [DCC13], but without any muon veto and isolation cut before the prompt event to better study the influence of events preceding neutrino candidates. Table VII.1 lists the applied cuts in detail.
The minimal deposited energy / charge to treat events as muons was chosen very low. Due to the used loose cuts, all events with any amount of deposited charge in the Inner Veto were treated as muons. Thus any neutrino candidate with a simultaneous energy deposition in the IV in either prompt or delayed event was considered as muon event.
If a neutrino candidate was found, its prompt and delayed event energy and the time difference were saved into a Root-Tree. For muons, which preceded the candidate up to a time window of one second, the deposited energy respectively charge and the time difference Δt to of the neutrino candidate were saved. For Inner Veto muons additionally information on the recording trigger type was saved.

Table VII.1: Used cuts for the neutrino candidates and muon search.

Muons	Inner Detector	Inner Veto
Deposited energy/charge	20 MeV	> 0 DUQ

Neutrino candidates	Gadolinium	Hydrogen
Prompt energy window [MeV]	0.7 - 12.2	0.7 - 12.2
Delayed energy window [MeV]	4.0 - 10.0	1.8 - 2.6
ΔT [µs]	0.5 - 150	0.5 - 600
Distance between events [mm]	1000	600
Charge in IV	0	0

For this study the same list of runs was used as in [DCC14]. As some run files could not be used due to missing information the total life time was 485 days. In these runs 16,499 neutrino candidates for the capture on gadolinium and 63,261 for the capture on hydrogen were found.
In the first, basic analysis the Δt information of all muons preceding a neutrino candidate within a time window of 10 ms were filled into a histogram for all neutrino candidates.
For uncorrelated muons a flat time distribution is expected. Figure VII.1 shows the results for gadolinium neutrino candidates. A clear excess for small Δt is visible. In that time region over 90 % of the neutrino candidates are muon correlated and therefore most probably not neutrinos but rather fast neutrons or other spallation products.
Alberto Remoto has performed a similar analysis in his thesis [Rem12]: As a result of his study, a muon veto time of 1 ms was applied for the first Double Chooz general analyses[DCC11, DCC12, DCC13]. In short this means that each event following a muon within less than 1 ms is neglected in terms of the neutrino search analysis.

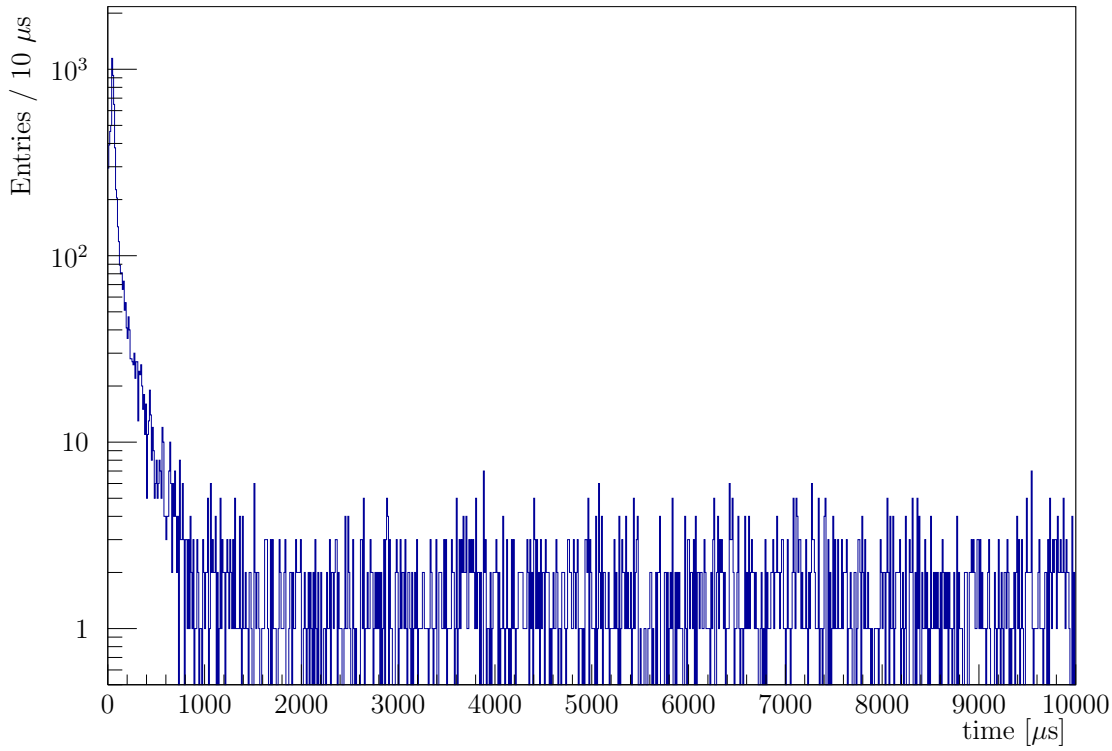

Figure VII.1: Δt distribution for all muons preceding gadolinium neutrino candidates within a time window of 10 ms.

3 Muon energy dependent analysis

To improve the study mentioned in the previous section, the muons were analysed by their deposited energy in the different detector parts.

3.1 Study of the time distribution of correlated muon events

As a first step, a possible correlation between the muon events will be investigated. Muons themselves are not correlated to each other, but due to the loose muon selection cuts, other events could be picked up, which can be correlated with a preceding muon. Correlated events can be spallation products as well as electronic effects like overshoots that conduct a retriggering. Therefore a veto time window after each muon is introduced to select the initial muon. Any event following within this dedicated time period will be excluded from the analysis.
To determine the veto time window, the time distribution of all preceding muons was investigated. Figure VII.2 shows the resulting histograms.
The upper plots showing the time distribution of muons following a muon in the same detector volume, the lower ones are for muons following in the other detector volume. The peak immediately after a muon and the following dip are caused by retriggering effects and baseline shifts. The peak for muons after an Inner Veto muon after $\sim 50\,\mu s$ (Figure VII.2(b) and VII.2(d)) are artefacts of the triggering system.
In these plots it is clearly visible, that after a muon in the ID the muon events following after $200\,\mu s$ are uncorrelated. For muons in the IV a longer veto time is needed. Here it takes $500\,\mu s$ until that the muon events are not correlated anymore.
So for the following analyses an inter-muon veto time of $200\,\mu s$ after a muon in the Inner Detector and $500\,\mu s$ after a muon in the Inner Veto was used.

3.2 Determination of the energy dependent time cut

The remaining muons after the time veto cut were sorted by deposited energy, respectively charge. The energy / charge range was split in 25 bins of equal width. Then the time distribution to the neutrino candidates were plotted for each bin and normalized to contain the same total amount of entries for a better comparison. Figure VII.3 shows exemplary the normalized time distribution of muons depositing 400 up to 440 kDUQ in the Inner Veto for neutrino candidates captured on hydrogen.
If these events are not correlated with the neutrino candidates, a flat distribution is expected. Like in figure VII.1 a clear excess for small time differences in the order of $\sim$1 ms is visible. The red line in figure VII.3 indicates the uncorrelated events and was determined by performing a fit in the window of 2 - 10 μs. In this off-time window only uncorrelated events are left. In a next step the information from the several histograms, as they were based on energy / charge bins, was combined and filled in two-dimensional histograms.

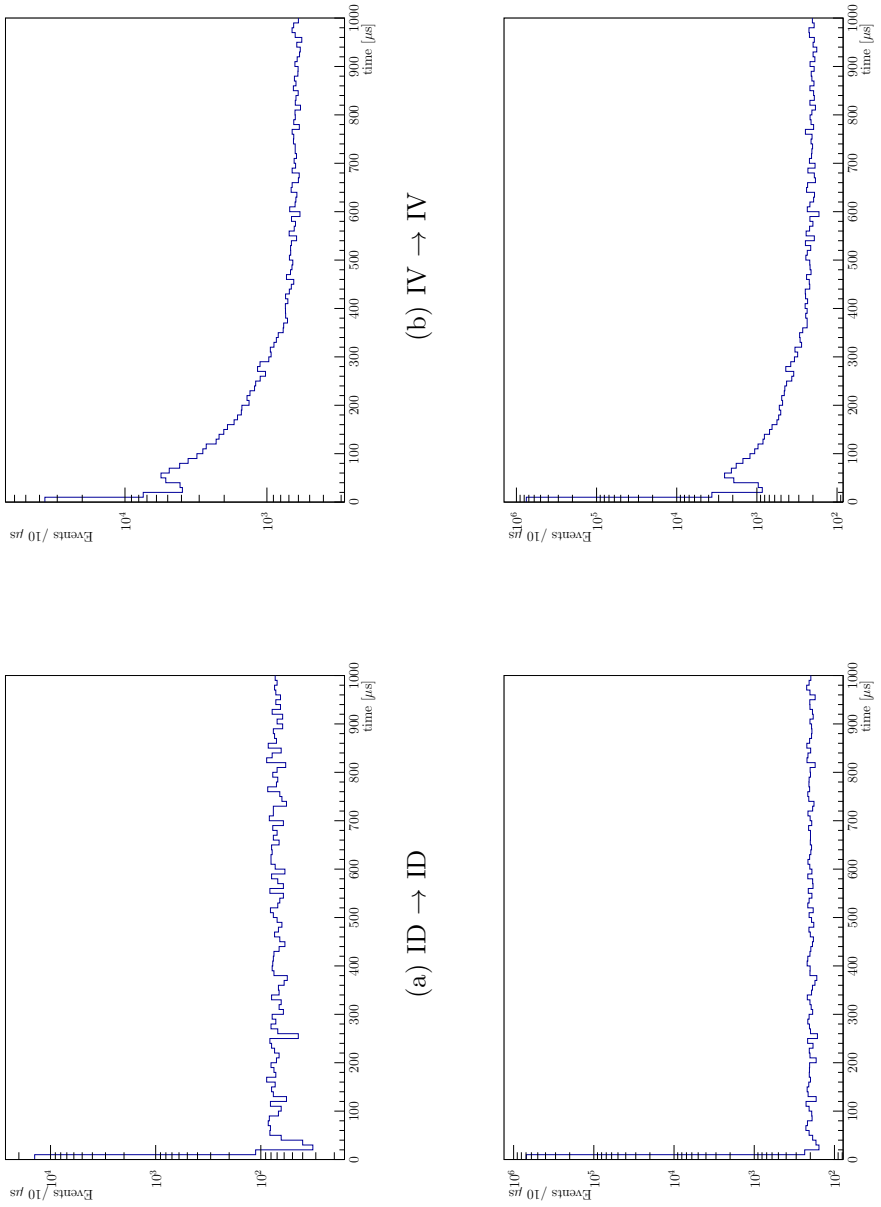

(a) ID → ID (b) IV → IV

(c) ID → IV (d) IV → ID

Figure VII.2: Time distributions of muon events in the Inner Detector / Veto following a muon event in the Inner Detector / Veto and vice versa.

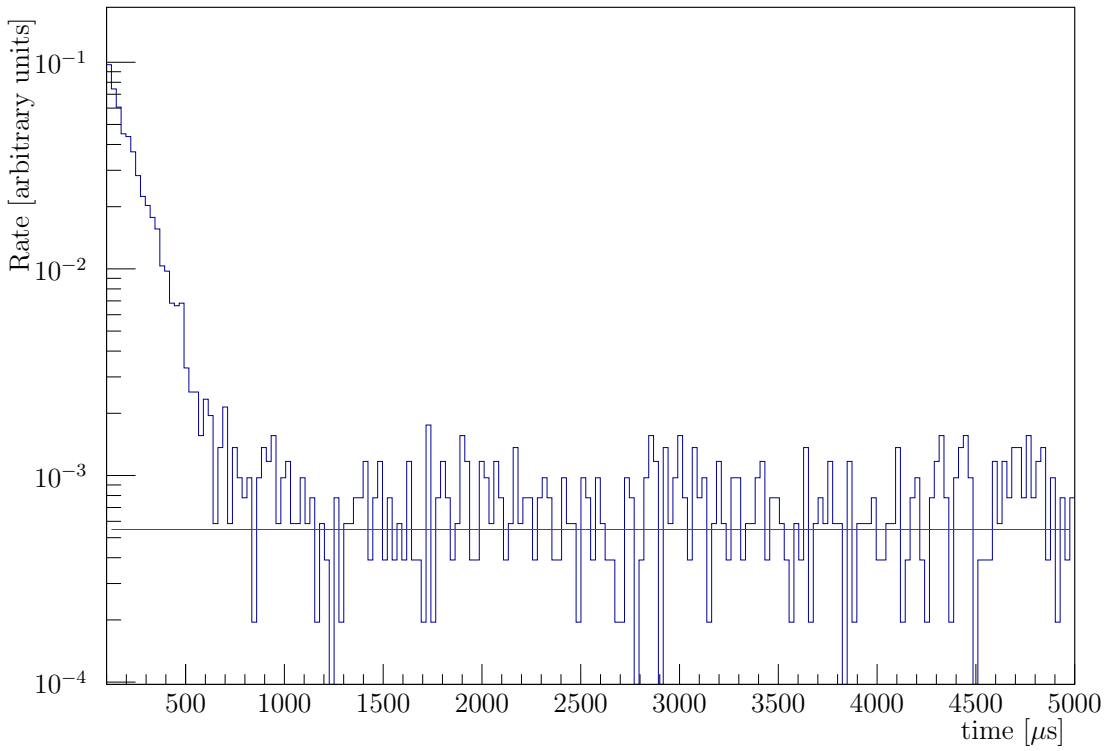

Figure VII.3: Time distribution of muons preceding neutrino candidates captured on hydrogen which deposited between 400 and 440 kDUQ in the Inner Veto (blue). The fit to the uncorrelated background is marked in red.

In figure VII.4 the results of the analysis are plotted. All four plots show a clear excess for time differences in the order of one µs to the preceding muon. This is excess is broader in time for the hydrogen than for the gadolinium analysis. Also both indicate, that muons which deposited more energy / charge, have a longer time window, in which correlated events occur. This effect is even more pronounced in the hydrogen analysis.
To further study these effects, a fit with an exponential function $f(t) = A \cdot \exp(-B \cdot t)$ was performed to the excess for each histogram. The influence of a proceeding muon is visible as long as the correlated events are higher than the uncorrelated background. To determine this, the intersection point of the exponential function with the background U gained by the fit described above was calculated as

$$A \cdot \exp(-B \cdot t) = U \longrightarrow t = \frac{\ln(A) - \ln(U)}{B}.$$

The error on the intersection point can be computed as

$$\Delta t = |\frac{\Delta U}{UB}| + |\frac{\Delta A}{AB}| + |\frac{\Delta B}{B^2}|$$

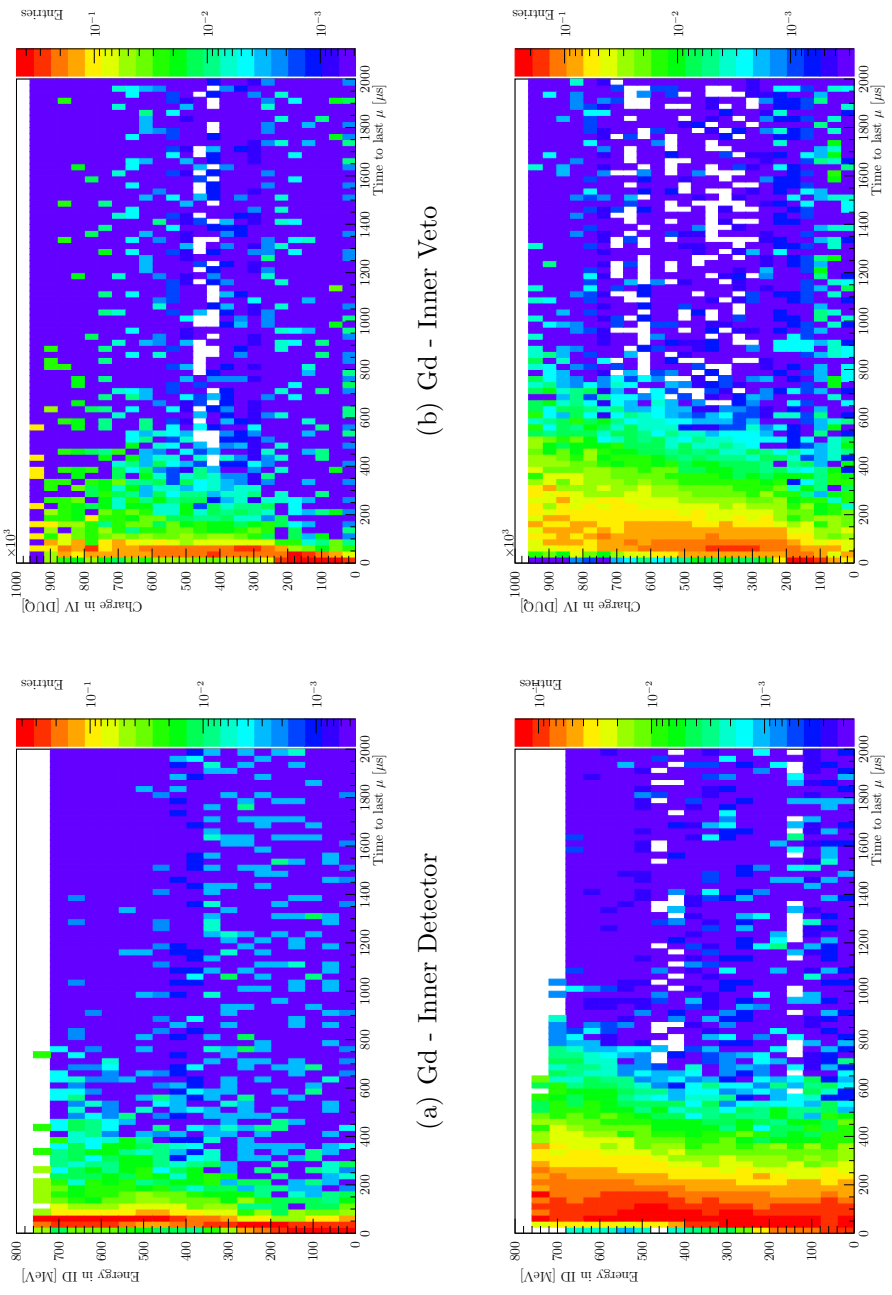

(a) Gd - Inner Detector (b) Gd - Inner Veto

(c) H - Inner Detector (d) H - Inner Veto

Figure VII.4: Two-dimensional distribution of deposited energy/charge and time after a neutrino candidate. Left for the Inner Detector, right for the Inner Veto. The upper figures for capture on gadolinium, the lower ones for capture on hydrogen.

In figure VII.5 these intersection points for the different energy / charge areas are plotted. As mentioned before these intersection points correspond to the time window in which the proceeding events are correlated with the muon. Like in figure VII.4, a general tendency to longer time windows of correlated events for more dependent energy / charge is visible. This trend reverses for lower energies, where the veto time windows are not getting smaller, but wider. This will be studied in more detail in section 3.3. The large errors especially in the gadolinium analysis are related to poor statistics in the single bins. Particular the fit of the exponential yields larger errors.
To use these results for the neutrino search calculation, specifications were introduced to compute the veto time window T for each muon by its deposited energy / charge. These specifications are:

$$
\begin{array}{lll}
\text{Gd Inner Detector:} & T = & 0.75\,\mu\text{s/MeV} + 700\,\mu\text{s} \\
\text{Gd Inner Veto:} & T = & 0.2\,\mu\text{s/kDUQ} + 800\,\mu\text{s} \\
\text{H Inner Detector:} & T = & \begin{cases} 1000\,\mu\text{s} - 0.5\,\mu\text{s/MeV} & \text{if } E_{dep} < 400\,\text{MeV} \\ 2\,\mu\text{s/MeV} & \text{if } E_{dep} >= 400\,\text{MeV} \end{cases} \\
\text{H Inner Veto:} & T = & \begin{cases} 1000\,\mu\text{s} - 2\,\mu\text{s/kDUQ} & \text{if } E_{dep} < 200\,\text{kDUQ} \\ 300\,\mu\text{s} + 1.5\,\mu\text{s/kDUQ} & \text{if } E_{dep} >= 200\,\text{kDUQ} \end{cases}
\end{array}
$$

It is also possible to express them graphically: In figure VII.5 they are marked as red lines. The specifications were chosen conservatively, in particular for the gadolinium analysis due to the large errors.

3.3 Studies of lower muon energy thresholds

Another part of this study was to determine the energy / charge threshold for muon identification. This is an important issue, since - like discussed in section 3 - all events following within a 1 ms time window after at tagged muon are discarded from the neutrino analysis. This will be studied in the next sections for Inner Detector and Inner Veto separately.

3.3.1 Inner Detector muon threshold

As it can be seen in figure VII.4 no lower threshold is visible for Inner Detector muons where events are not to be correlated with the neutrino candidates. Therefore the threshold to flag an event as a muon and discard every event following it inside the muon veto time, should be set as low as possible. As the energy region between the end of prompt event energy region up to 20 MeV is necessary for the fast neutron determination, a threshold of 20 MeV is favoured by this study.

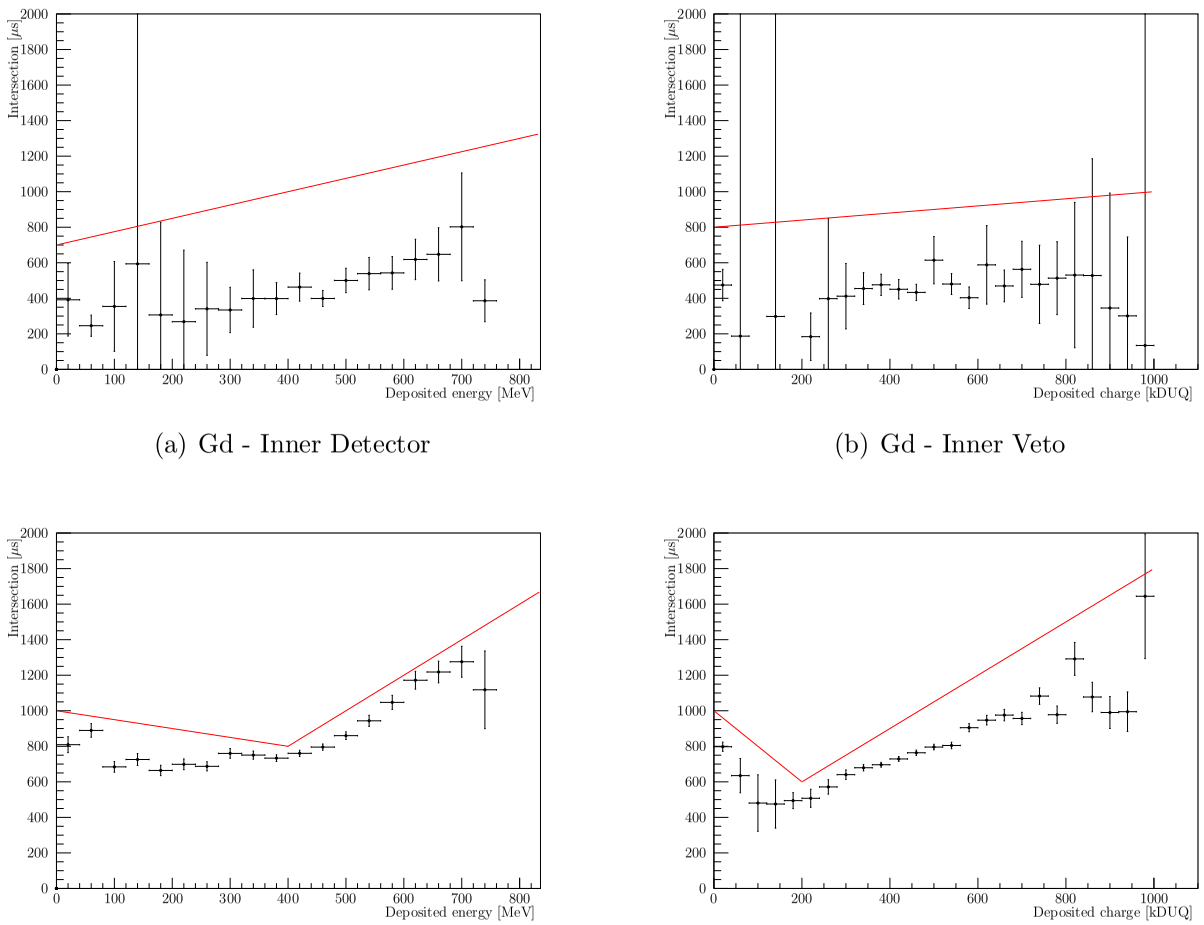

(a) Gd - Inner Detector

(b) Gd - Inner Veto

(c) H - Inner Detector

(d) H - Inner Veto

Figure VII.5: Intersection points of an exponential fit to the excess and a background fit. This corresponds to the veto time windows in which subsequent events are considered correlated with the preceding muon. Results for both n-capture analyses and both detector types are plotted. In red the proposed veto time window is plotted.

3.3.2 Inner Veto muon threshold

For the Inner Veto study any charge deposition in the veto was taken as a muon candidate. As the veto has a trigger threshold at around 36 kDUQ (see section 6 in chapter V), the selected events below the threshold had to be analysed by trigger type.

In figure VII.6 events with charge depositions smaller than the Inner Veto trigger threshold are plotted, sorted by their recording trigger type. It is clearly visible, that the events recorded by the prescaled trigger and the Inner Veto physics trigger do not show a correlation with the neutrino candidates, but the events recorded by the physics Inner Detector trigger are correlated.
So this study suggests to reject all events following in the muon veto time period after a charge deposition in the Inner Veto, if the deposited charge is higher as the IV-trigger threshold of 36 kDUQ or was triggered by the Inner Detector physics trigger.

3.4 Introduced dead time

The vetoing of muon events results in a time, which is excluded from the search for neutrino candidates, the so called dead time. Table VII.2 lists the introduced dead times in percent of the data taking time for different veto time windows.
For the veto time window of 1 ms after a muon, which was used in [DCC11, DCC12, DCC13, DCC14] the overall dead time is 4.0 %. With the new veto time window, which is proposed in this chapter, the overall dead time can be reduced by 3.5 % to 3.9 % of the data taking time for the gadolinium analysis. For the used 485 days in this study this corresponds to a gain of 16 hours of life time.
Looking at the hydrogen analysis, the new veto time leads to an increase of 16 % with respect to 1 ms veto time. For the new hydrogen analysis which will be published soon a veto time of 1.25 ms was proposed. This corresponds to an increase of 23 % with respect to the 1 ms veto time to 4.9 % of the total data taking time. In comparison to this veto time of 1.25 ms, the dead time introduced by the veto procedure proposed in this chapter the dead time reduces by 5.7 %, resulting in 4.7 % of the total data taking time. This corresponds to a gain of 32 hours for a life time of 485 days.

Table VII.2: Introduced dead time in percent of the data taking time for different muon veto times.

	gadolinium	hydrogen
1 ms	4.0 %	4.0 %
1.25 ms	4.9 %	4.9 %
New time window	3.9 %	4.7 %

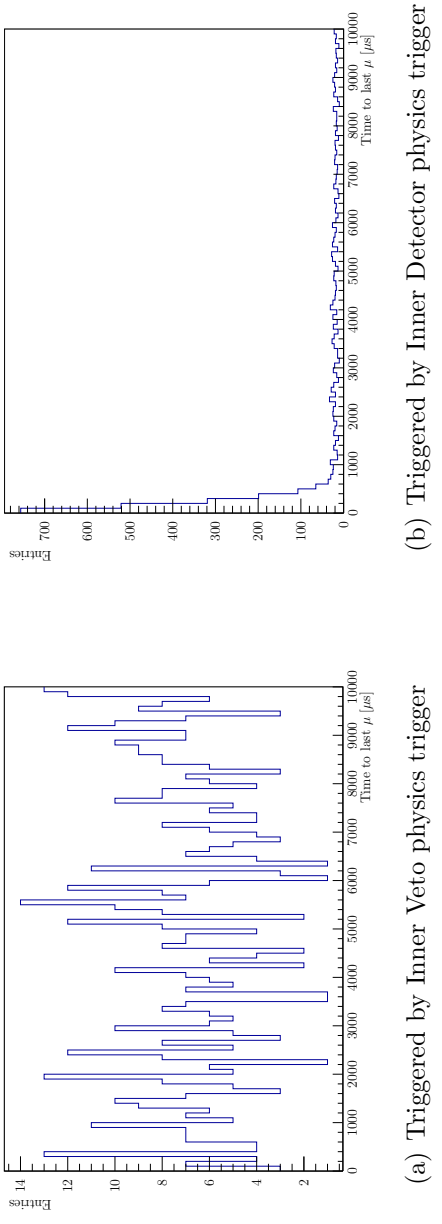

(a) Triggered by Inner Veto physics trigger

(b) Triggered by Inner Detector physics trigger

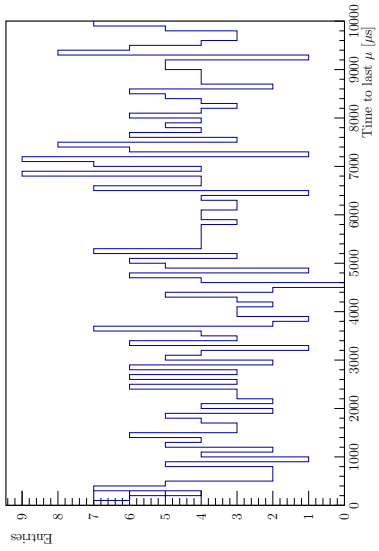

(c) Triggered by Inner Veto prescaled trigger

Figure VII.6: Time differences to neutrino candidates captured on hydrogen sorted by trigger types.

4 Conclusions

In this chapter new muon veto time windows, which are dependent on the deposited energy (respectively charge), were proposed and motivated. This new set of cut is:

$$
\begin{array}{lll}
\text{Gd Inner Detector:} & T = & 0.75\,\mu\text{s/MeV} + 700\,\mu\text{s} \\
\text{Gd Inner Veto:} & T = & 0.2\,\mu\text{s/kDUQ} + 800\,\mu\text{s} \\
\text{H Inner Detector:} & T = & \begin{cases} 1000\,\mu\text{s} - 0.5\,\mu\text{s/MeV} & \text{if } E_{dep} < 400\,\text{MeV} \\ 2\,\mu\text{s/MeV} & \text{if } E_{dep} >= 400\,\text{MeV} \end{cases} \\
\text{H Inner Veto:} & T = & \begin{cases} 1000\,\mu\text{s} - 2\,\mu\text{s/kDUQ} & \text{if } E_{dep} < 200\,\text{kDUQ} \\ 300\,\mu\text{s} + 1.5\,\mu\text{s/kDUQ} & \text{if } E_{dep} >= 200\,\text{kDUQ} \end{cases}
\end{array}
$$

One of the following conditions should be met for events that are flagged as muons:

- Deposition of more than 20 MeV in the Inner Detector
- Non-zero charge deposition in the Inner Veto triggered by the Inner Detector physics trigger or more than 36 kDUQ

With these cuts the introduced dead time, which is neglected for the neutrino candidate search is reduced to 3.9 % of the data taking time for the gadolinium analysis and lies at 4.7 % for the hydrogen analysis.

VIII
Detector stability

In this chapter a quick and easy method to monitor the scintillator light output will be introduced. For each run the position which means the deposited charge of two muon induced peaks is fitted, one for each detector volume. The temporal development of these position is then used to monitor the scintillators.

1 Method

As shown in section 2.2 in chapter V, there is a peak in the Inner Veto charge spectrum, which corresponds to muons, which cross the veto volume twice. A similar peak exists in the Inner Detector charge spectrum. Here the height of the gamma catcher is the limiting factor as most of the crossing muons are minimal ionizing particles and therefore have a specific energy loss per traveled track length.
Thus both peaks occur due to geometrical reasons. The position of the peak in the Inner Veto is between 400 and 500 kDUQ and the one of the Inner Detector is located at around 7,000 kDUQ.
To determine the scintillator stability the charge spectrum of each run was taken and a Gaussian fitted the both peaks (see figure VIII.1). The peak position and its uncertainty were saved. For each day the results of all runs of this day were averaged. The mean error ΔP was computed with $\Delta P = \sqrt{\sum_i \Delta P_i^2}$, where ΔP_i is the error of the determined peak position of run i.
As in this study the peak position and not the rate at the position is under investigation, it is therefore independent from the rate variation of the muon flux discussed in section 5 of chapter V.

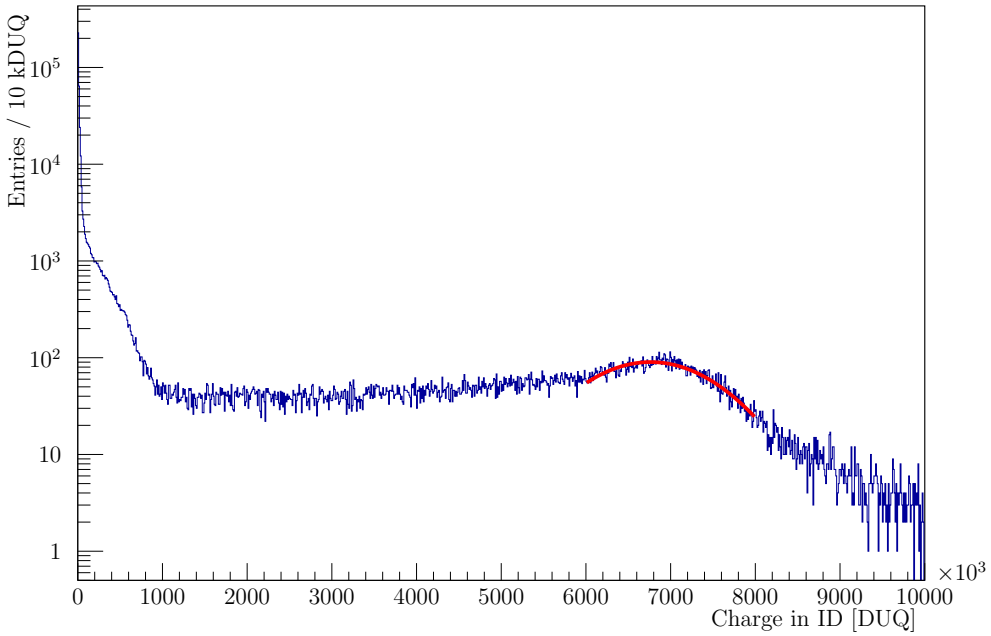

(a) ID energy spectrum

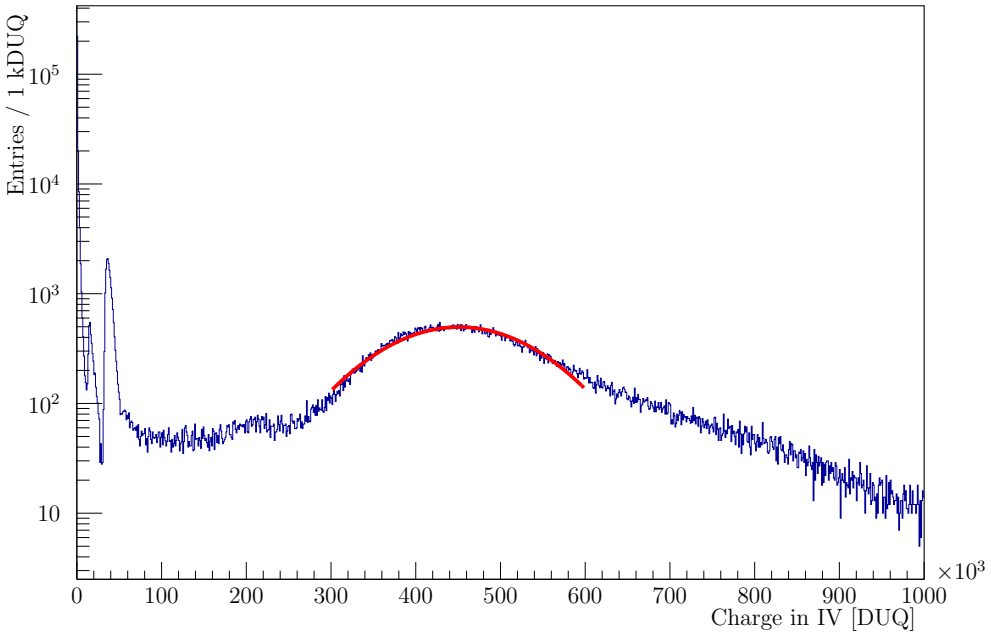

(b) IV charge spectrum

Figure VIII.1: Example of the charge/energy spectrum of the Inner Detector (top)/Inner Veto (bottom) in blue. Marked in red are the Gaussian fits, which position is read out for each run.

2 Result

For this study the data of all runs in [DCC14] were analysed, which correspond to a time period of almost two years. Figure VIII.2 shows the evolution of the fitted mean peak position of each day for this time.
In both figures trends are visible. The peak position in the Inner Veto is decreasing from 450 kDUQ to 445 kDUQ, which is a reduction of 1 %. For the ID the situation is reverse: Here the peak position is increasing from 6750 kDUQ to 6850 kDUQ, which corresponds to an enhancement of 1.5 %. Two possible influences on the peak positions were investigated: the gain of the PMTs and the temperatures of the liquids.
A change in the gain of the PMTs will yield in a different amount of charge per detected photon. The gains of the ID and IV PMTs are checked weekly with the intrinsic light injection systems. The resulting gains of all PMTs in the respective detector for each calibration were averaged and plotted in figure VIII.3. Except of some fluctuations both gains of ID and IV PMTs are stable and show no behaviour like the shifts of the peak positions. In Double Chooz it is hard to test the PMT gain itself as the PMTs are readout by the data acquisition electronics. Thus the values shown here are influenced by the electronics, but act therefore as a test of the whole readout chain.
The temperature of a scintillator has an influence on its light output as well. In the Inner Veto and the Gamma Catcher thermometers are installed. In figure VIII.4 the chronological sequence of the temperatures in IV and ID are plotted. As expected they show a seasonal trend, yet with a maximum variation of around two degrees. The extrema are far less pronounced compared to the air temperature values. The maximum variation is two degrees. Thus also the temperatures show no corresponding behaviour than the peak positions.
Summing up a variation of the muon induced peak positions in the energy / charge position in the energy / charge spectra of the ID / IV in time can be observed, which results in a increase / decrease of the peak positions of less than 1 % per year, respectively. Two possible explanation for this behaviour were studied, but neither the gain of the PMTs nor the temperature of the liquids in ID / IV shows a time variation in line with the shift of the peak positions with time, so both can be excluded as a reason of this feature.

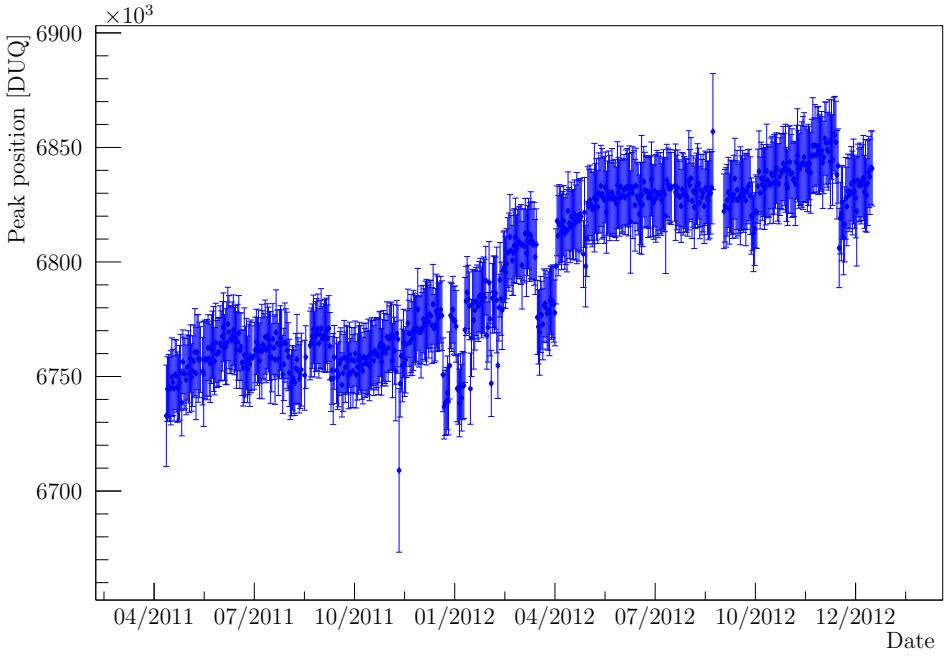

(a) ID

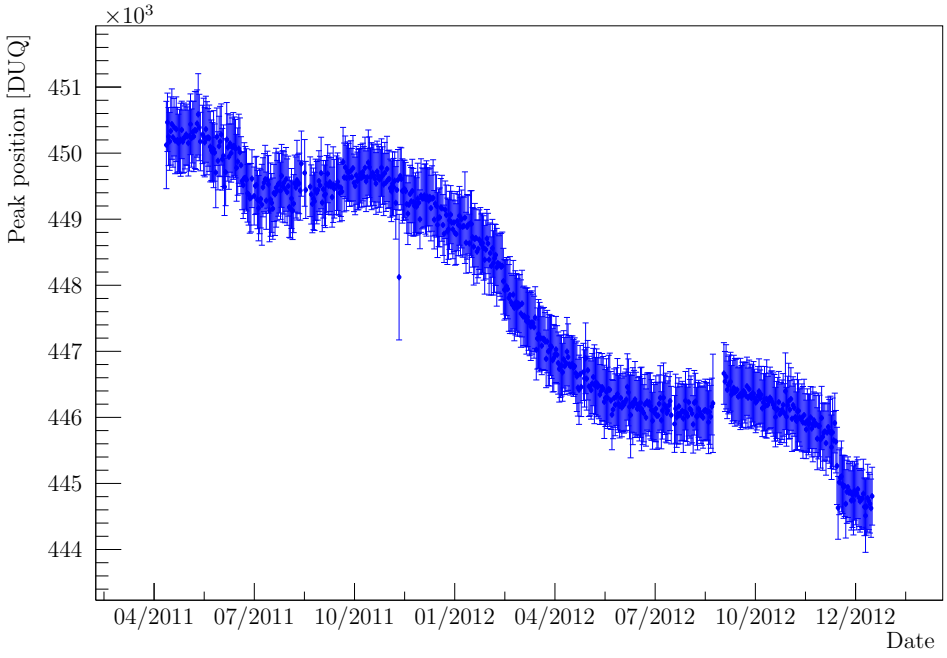

(b) IV

Figure VIII.2: Time variation of the muon induced peak in the ID and IV.

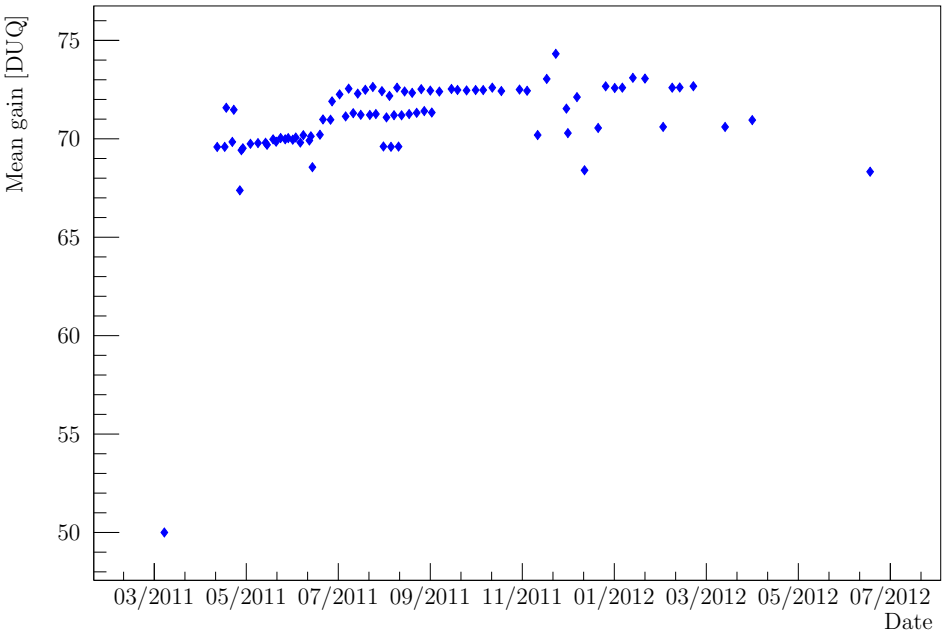

(a) ID

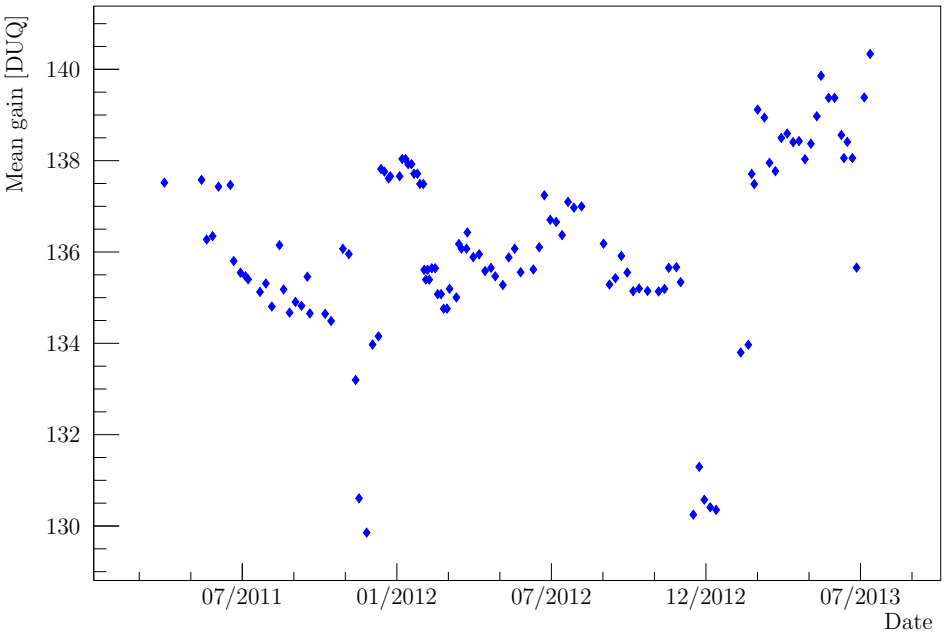

(b) IV

Figure VIII.3: Time variation of the mean PMT gains in ID (top) and IV (bottom). The mean gain in the ID is 71 DUQ/PE, while the mean gain in the IV lies at 136 DUQ/PE.

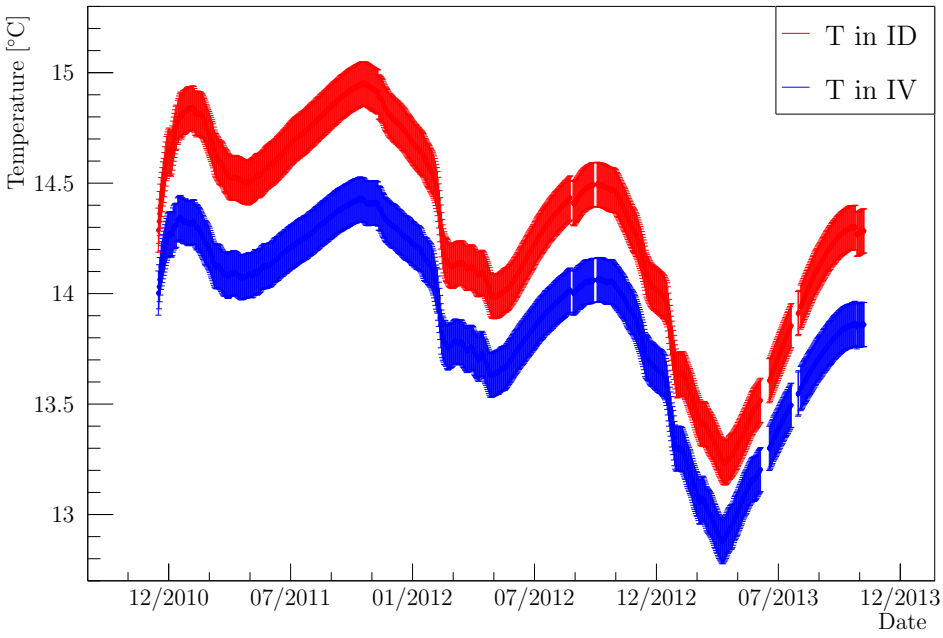

Figure VIII.4: Time variation of the temperature in the Inner Veto (blue) and the Inner Detector (red).

IX

Fast neutron background in the JUNO experiment

The JUNO experiment aims for a sub-percent measurement of the neutrino mixing parameters, to solve the neutrino mass hierarchy problem and to detect the Diffuse Supernova Neutrino Background (DSNB). Like in Double Chooz muon induced neutrons are a major background component for the neutrino detection in JUNO, especially for the investigation of reactor neutrinos and the DSNB.
JUNO is currently in its design phase. Its planned design and detection technique are quite similar to Double Chooz and other so called LAND (Liquid scintillator Anti Neutrino Detector) experiments like LENA. In this chapter, building on the experience from Double Chooz, the rate of coincidences caused by muon induced neutrons in dependence of the water shielding thickness was studied to give an input for the dimensions of an effective water shielding.

1 The JUNO experiment

The name JUNO stands for **J**iangmen **U**nderground **N**eutrino **O**bservatory. It is a planned experiment and should be settled in the administrative area of Jiangmen, a city in southeast China, 100 km west of Hong Kong.
JUNO will be a liquid scintillator based detector. One of its main purposes is to solve the neutrino mass hierarchy problem and to measure the neutrino oscillations parameters Δm^2_{12}, Δm^2_{23} and $\sin^2(\theta_{12})$ with sub-percent precision (for details see section 2.2.2 and 2.3 in chapter II) by the detection of reactor neutrinos. In addition it will be possible to investigate atmospheric, geo and solar neutrinos. Furthermore there is the goal to detect

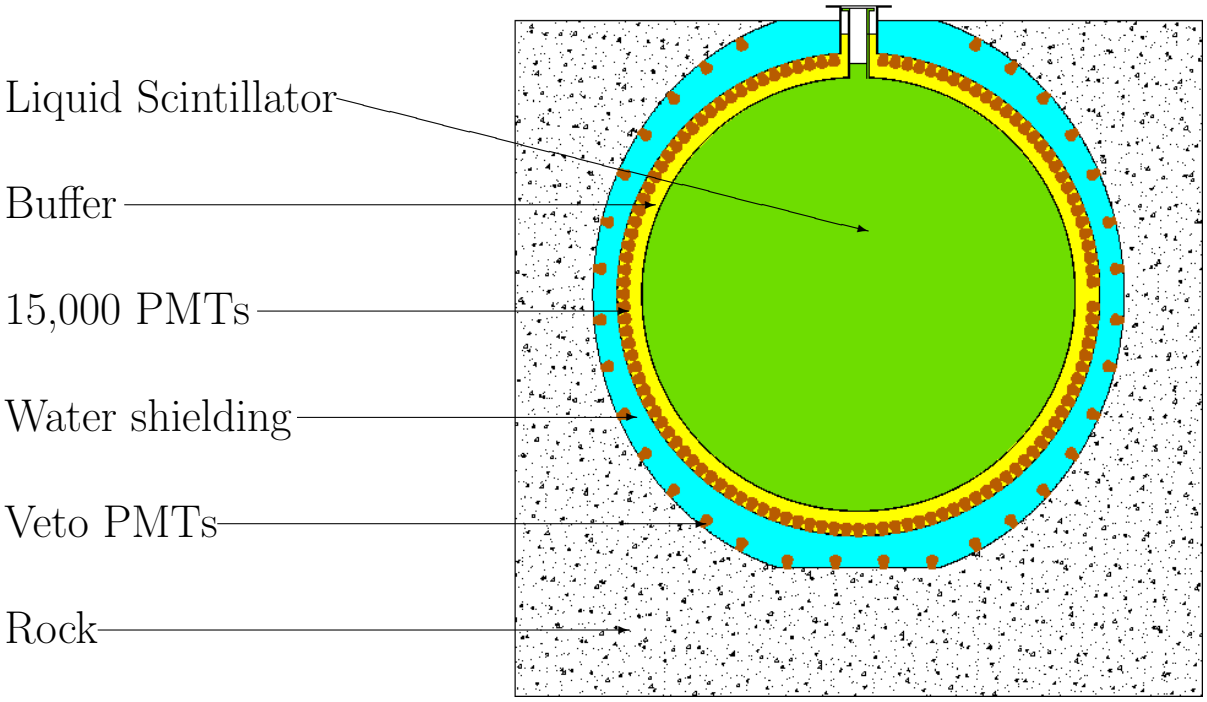

Figure IX.1: Schematic drawing of the JUNO detector with marked components[He13].

the DSNB and to survey a possible supernova in our galaxy.
The detector will have a spherical shape with an onion like composition. The target region will be located in the centre with a radius of 17.7 m filled with 20 kilotons (ktons) of liquid scintillator. It will be surrounded by a buffer volume with a thickness of 1.5 m that will be loaded with non-scintillating mineral oil. Both volumes will be separated by a nylon balloon and contained in a stainless steel vessel of 19.3 m radius and a thickness of 10 cm. 15,000 PMTs of 20 inch diameter will be mounted on the inner wall of this vessel, which will result in an optical coverage of 77 %[He13, Gra13]. This stainless steel vessel will be place in a cavern, which will be filled with water. A sketch of the detector is shown in figure IX.1.
A special underground laboratory will be constructed for JUNO, so that it will be covered by 700 m of rock. The start of data taking is planned in 2020.
There are two nuclear facilities at a distance of 53 km each, whose neutrino spectra JUNO will analyse. Like Double Chooz, Juno will detect neutrino via the inverse beta decay reaction $\bar{\nu}_e + p \rightarrow e^+ + n$. The estimated positron spectrum for normal and inverted neutrino mass hierarchy is plotted in figure IX.2. Due to the longer distances to the reactors compared to Double Chooz more neutrinos are already oscillated into another flavour. The big dip from 2 to 4 MeV is caused by the mixing angle θ_{12}, while the smaller oscillations are a result of θ_{13}. The two lines in IX.2 indicate the positron spectra for the two possible mass hierarchies. With a foreseen measurement time of five years a distinction between both hierarchies will be feasible on a 3 σ level.

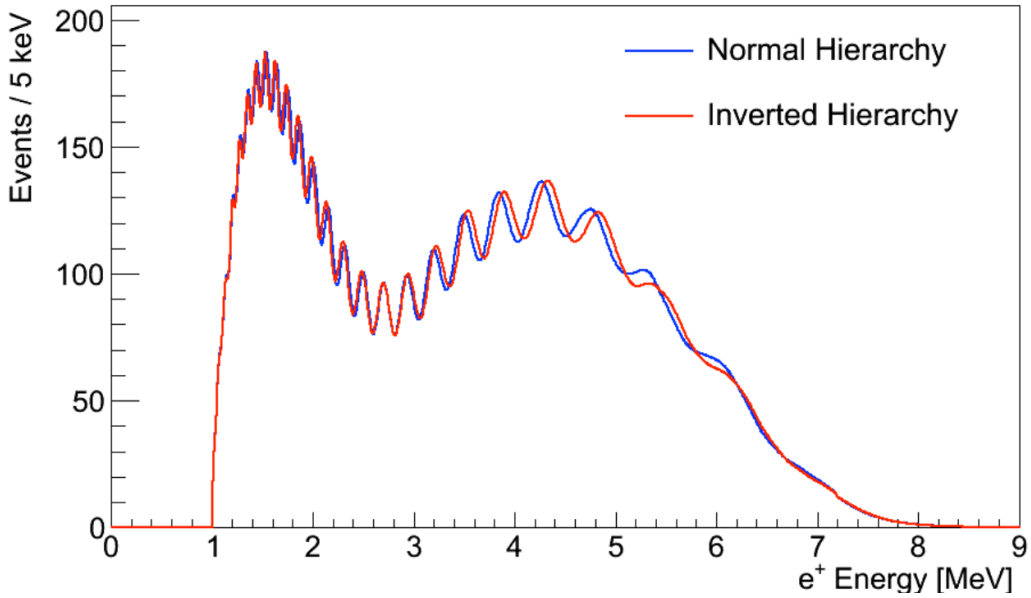

Figure IX.2: Estimated positron spectrum for JUNO for normal and inverted neutrino mass hierarchy[Cah13].

As in Double Chooz, muon induced neutrons are a dangerous background for the neutrino search. A neutron produced by a muon, which passed the detector without hitting it, can enter the detector, recoil on a proton resulting in an energy deposition in the positron energy window, thermalise and get captured (see section 6.1.1 in chapter III).
The probability for a neutron to enter the detector depends on the distance which it has to travel before with a decreasing probability for increasing distances. Moreover the material which it has to penetrate plays an important role. As the most energy is lost by hits with partners of the same mass, a hydrogen rich material is useful to reduce the neutron flux.

2 JUNO simulation

To perform a simulation many details like detector composition have to be given to the simulation program (see section 6.5 in chapter III for details). As an official package was not yet available for the JUNO experiment at the time of this study, the one of the experiment LENA with some modifications was used to perform the simulation. The **L**ow **E**nergy **N**eutrino **A**stronomy experiment is till in its design phase. Like JUNO it is a large scale scintillator experiment with similar physical goals. Therefore it suggests itself to use the existing simulation package of LENA.

2.1 The LENASim package and modifications for JUNO

Like the Double Chooz simulation software (see section 6.5 in chapter III) also the LENA simulation software is based on Geant4. For the simulations the Geant4-own physics list "QGSP_BERT_HP" was used (for details see [GPL]). Major parts of this simulation were written by Randolph Möllenberg and are described in his PhD thesis[Möl13].
To adapt the existing LENA simulation to the JUNO experiment some modifications were necessary. For simplicity all PMTs were discarded and only the energy depositions simulated. Also the geometry was adapted to JUNO, which means to move from the cylindrical volumes of LENA to the spherical geometry of JUNO with the corresponding dimensions. Table IX.1 list all simulated volumes and their dimensions.

Table IX.1: Simulated JUNO volumes. Water shielding was simulated twice: first as sphere, second as cylinder.

name	radius [m]	content	geometry
Target	17.7	liquid scintillator	sphere
Inner Buffer	18.75	mineral oil	sphere
Outer Buffer	19.2	mineral oil	sphere
Tank	19.30	stainless steel	sphere
Water shielding	variable	water	sphere & cylinder

The distinction of the buffer between inner and outer volume and the separation by a 1 mm thick stainless steel wall are relics of the LENA detector geometry, where the PMTs are not mounted directly to the tank walls, but to a stainless steel construction in the buffer volume. In the simulation it can also be used as a photo sensitive area instead of simulating single PMTs. As it does not influence the inner detector behaviour, it was decided not to remove it from the simulation.
Muons are started in the surrounding of the detector. Most of the neutrons are not produced by the muon itself, but by hadronic showers initialized by the muon[Möl13]. To allow these showers to grow, only neutrons were used, which were produced after three meter of muon track length. As output the energy spectrum of the produced neutrons is stored in a file.
The surrounding rock of the LENA site is limestone, so calcium-carbonate ($CaCO_3$) with a density of $2.73\,g/cm^3$, where it is granite (SiO_2) for JUNO with a density of $2.80\,g/cm^3$. As the overburden of JUNO is smaller than that of LENA, the corresponding mean muon energy is also lower, namely 211 GeV instead of 300 GeV[Gra13].

2.2 Fast neutron simulation

As described before the recorded energy spectrum was used to simulate neutrons in JUNO. To find the optimal parameters to minimise the neutron flux in the target the water shield-

ing thickness was varied from one to ten meters in one meter steps, so in total ten simulations were performed. Like in the LENA simulation neutrons were started in a hollow sphere around the outermost volume, the water shielding. This sphere has a width of 4 meters. The neutrons were given a random direction and a randomly chosen energy corresponding to the spectrum obtained by the previous simulation. Only neutrons, which were facing towards the detector, were propagated to save computing time.
The deposited energy by the muons in the inner detector was saved. In case they were captured, also the time delay between energy deposition and the emission of the gamma photons due to the capture was stored. The neutrons were started one by one, there was a chance, that they could produce additional neutrons, thus the amount of captured neutrons in the inner detector was saved, too. In total for each thickness 1,000,000 neutrons were simulated.
In a further step the design of the water shielding was changed to test another veto geometry. For this test the sphere was replaced by a cylinder with the same diameter and height. Here not a hollow cylinder but a hollow sphere was used as starting points of the simulated neutrons.

2.3 Results

Like for Double Chooz (for details see section 6.1.1 in chapter III) the most dangerous backgrounds for JUNO are events, which can mimic the neutrino signal. Muon induced neutrons can do so by first depositing energy in the positron energy width and a delayed neutron capture.
JUNO will use the inverse beta decay with the positron annihilation as prompt and the gammas of the following neutron capture as delayed signal as it is also utilized for the Double Chooz hydrogen analysis. Unlike Double Chooz, JUNO will be able to detect neutrinos from three different sources: reactor neutrinos, neutrinos from the DSNB and single supernova events. In the energy range from 0.7 to 11 MeV positron energy the reactor neutrinos are the dominant source, in the range from 11 to 28 the DSNB neutrinos will take over. Neutrinos from a near supernova will have a broad energy distribution, but could be detected as they will produce multiple inverse beta decays at the same time due to the high neutrino flux (for details see [IMB]).
For the time difference between the positron and the capture event the same time cut of 0.5 to 600 µs was used as for the Double Chooz hydrogen analysis. As in the simulation only the information about the total energy deposition in the inner detector was used and not the capture itself, no corresponding cut was applied here. Only events with one neutron captured were analysed.
Applying these cuts, coincidences can be found in the simulation data. As these are fractions of the total simulated events, it is necessary to determine the simulated exposure time. With the exposure time, rates can be computed from the number of events, which can be used for comparison with the assumed signal rates.
The first step is to calculate the rate of neutrons R_n, which are produced in the vicinity of the detector. Therefore the muon rate and the number of neutrons per muon is needed.

The muon rate is 0.004 $(\mathrm{s\,m^2})^{-1}$ [Gra13], the amount of neutrons can be taken from the first simulation, where muons were propagated through the surrounding rock and the produced neutrons counted.
The muons were simulated for a length of 15 m. As the hadronic showers, where most of the neutrons are produced, need space to develop, the first three meters were neglected for the analysis. For this study 100,000 muons were simulated, which produced 150,041 neutrons. After the rejection of the first 3 m of path, 125,498 neutrons remained. This means each muon induced in average 1.25 neutrons on its 12 m path, which corresponds to a neutron yield Y_n of 0.10 neutrons per muon and travelled meter in rock.
For this rate estimation all muons were expected to come directly from above, so with a zenith angle θ of zero. This a conservative assumption as the muons can travel a long path along the detector without be seen by the veto mechanism. So the rate of neutrons can be calculated by

$$R_n = Y_n \cdot R_\mu \cdot V$$

with V as the starting volume of the neutrons. For the spherical and the cylindrical geometry option the volume is computed differently. For the spherical water shielding, V can be expressed by

$$V = \frac{4}{3}\pi((d_{start} + r_{water})^3 - r_{water}^3),$$

with d_{start} as the thickness of the neutron starting area, which is 4 m for this study.
For the cylindrical water shielding it can be calculated by

$$V = \pi \cdot ((d_{start} + r_{water})^2 - r_{water}^2) \cdot TL,$$

with TL as the muon track length, which is $TL = r_{water} + 2 \cdot d_{start}$ as the neutrons are also started above and below the detector.
With this information the simulated neutron exposure time can be calculated. Table IX.2 shows the results.

Table IX.2: Simulated exposure time in dependence from the water shielding thickness.

Thickness shielding [m]	1	2	3	4	5	6	7	8	9	10
Cylinder [d]	1.82	1.69	1.56	1.45	1.36	1.27	1.19	1.11	1.05	0.99
Sphere [d]	1.15	1.06	0.97	0.90	0.83	0.77	0.72	0.67	0.63	0.58

Using this results, the found neutron captures can be translated into rates of neutrino like coincidences. Table IX.3 lists all found coincidences and the corresponding rate.
It is also possible to extract the spatial position of the neutron capture from the simulation. In figure IX.3 the deposited energy is plotted against the minimal distance to the centre of the detector, the stopping radius for a spherical water shielding of 3 m. It is clearly

Table IX.3: Found neutron generated coincidences and corresponding rates in dependence upon the water shielding thickness and veto design for both detection energy windows. The error is the square-root of the respective entries.

Thickness water shielding	1	2	3	4	5	6	7	8	9	10
Sphere reactor ν bkg	95	33	7	7	3	0	0	0	0	0
Sphere reactor ν bkg/d	82	31	8	8	3	0	0	0	0	0
Sphere DSNB ν bkg	123	41	10	4	0	0	0	0	0	0
Sphere DSNB ν bkg/d	107	39	10	5	0	0	0	0	0	0
Cylinder reactor ν bkg	33	7	4	4	0	0	0	0	0	0
Cylinder reactor ν bkg/d	18	4	3	3	0	0	0	0	0	0
Cylinder DSNB ν bkg	42	6	3	1	0	0	0	0	0	0
Cylinder DSNB ν bkg/d	23	4	2	1	0	0	0	0	0	0

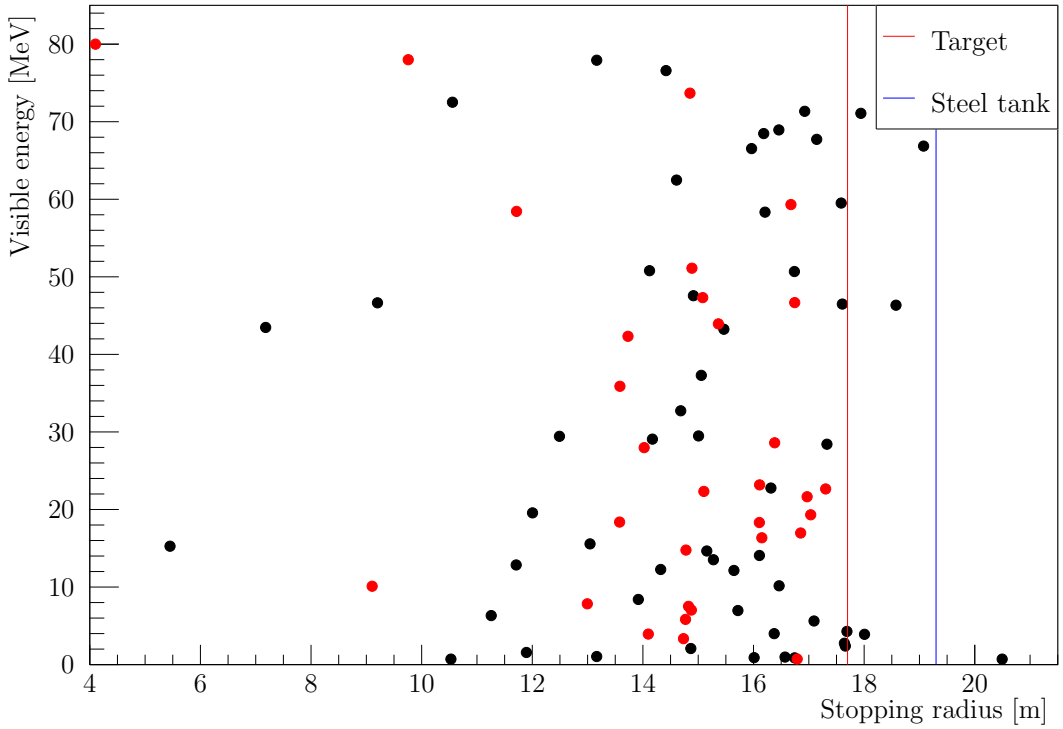

Figure IX.3: Stopping radii, thus the minimal distance to the detector centre, of neutrons with a spherical shielding of 3 m thickness. In blue and green the borders of the inner detector and steel tank are shown. The red dots signify events with one neutron capture, while the black dots are events with multiple neutron captures in the detector, where the shortest radius is plotted.

visible, that most of the energy depositions took place in the outer detector volumes, so for higher values of the stopping radius. Therefore a restriction of the used target mass is a possibility to reduce the background. Of course the available target mass, the fiducial volume is decreasing and with it the rate of detected neutrinos (see table IX.4). So for example with a volume cut of 14 m, only 49 % of the target mass is available and from expected 50 neutrinos per day only 25 will interact in the inner reduced volume.

Table IX.4: Total fiducial volume and percentage of the target mass for different volume cuts. The expected rate of detectable neutrinos is mentioned as well for an assumption of 50 neutrinos per day in the total detector. As an example the expected rate of reactor neutrino like background events for a spherical water shielding of 3 m is added.

Radius fiducial volume	10	11	12	13	14	15	16	17	17.7
Fiducial volume [m^3]	4189	5575	7238	9203	11494	14137	17157	20580	23228
% of full target	18	24	31	40	49	61	74	89	100
ν-rate per day	9	12	16	20	25	30	37	44	50
Bkg 3 m sphere reactor ν	1	1	1	2	2	6	6	7	7

In figure IX.4 the amount of coincidences in dependence upon the used target radius cut is plotted. Like it was shown in table IX.3 the amount of coincidences is decreasing with wider water shielding. Also the cylindrical water shielding leads to less coincidences in comparison to the spherical option due to the larger amount of water in the edges.

3 Conclusions

In this chapter the coincidence rate of muon induced neutrons in dependence to the water shielding thickness was studied for the JUNO experiment. As a result a cylindrical water shielding is favoured with a thickness of four to five meters and target radius cut of 16 to 17 m. This will reduce the rate of coincidences down to one per day for both neutrino detection channels.

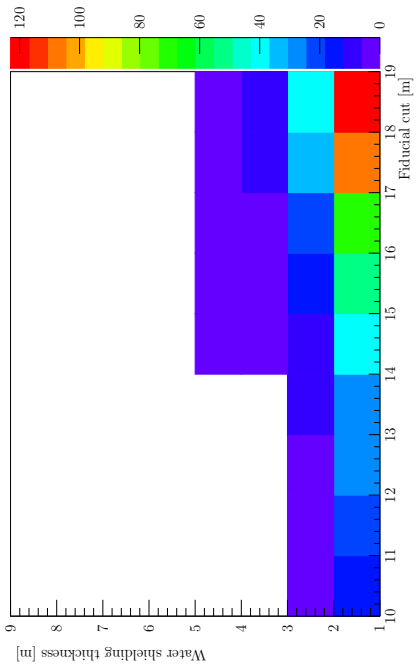

(b) Spherical shielding - DSNB neutrinos

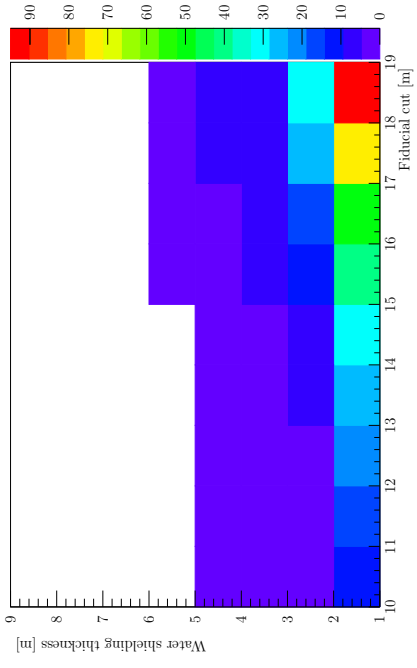

(a) Spherical shielding - reactor neutrinos

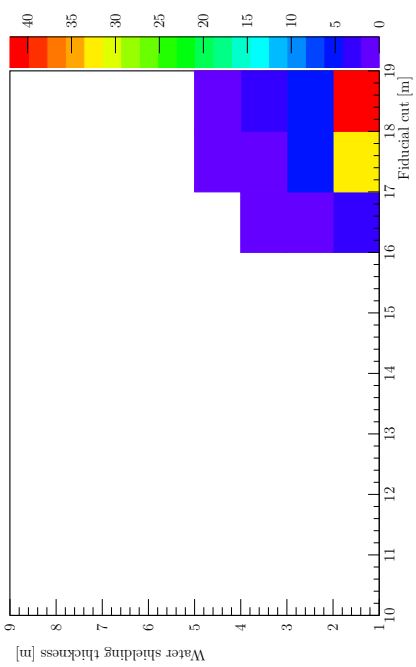

(d) Cylindrical shielding - DSNB neutrinos

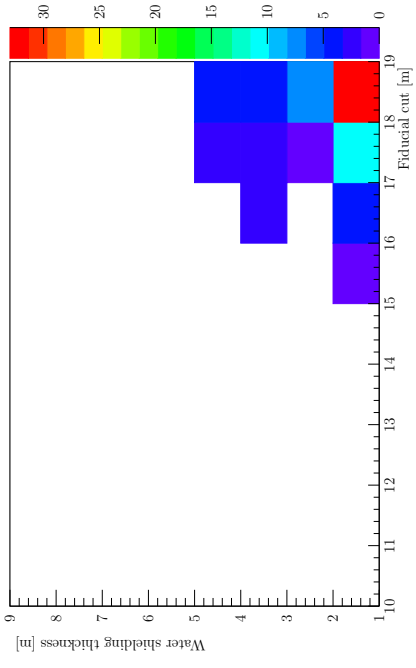

(c) Cylindrical shielding - reactor neutrinos

Figure IX.4: Rate of coincidences for spherical and cylindrical water shielding in dependence of the used target radius cut.

X

Summary & Outlook

Several studies were performed in this thesis:
Possible improvements on the near detector Inner Veto were tested with the aid of a Monte Carlo simulation. It could be showed that an increase in the number of PMT in the Inner Veto to 90 PMTs would lead to more detected light on average. Yet the number of events near the detection threshold of 5 PE is not decreasing. Due to the necessity of a new surface of the inner walls of the Inner Veto a further Monte Carlo study was performed. As result VM 2000 was chosen as surface of the Inner Veto of the near detector. The preparation of the foil for the installation and the assembly in the detector were presented.
The charge spectrum of the Inner Veto of the far detector was compared to a muon simulation and two characteristic peaks in the spectrum could be identified as muon induced. From this, a charge to energy conversion could be estimated. The trigger thresholds in the Inner Veto were determined as well. With the aid of the Dead Time Monitor the total rate of events in the Inner Veto was measured to 220,000 events/s. This rate corresponds to the estimated rate of dark noise from the PMTs and radioactive impurities.
The angular distributions of muons in the far detector reconstructed by two individual muon reconstruction algorithms were compared to Monte Carlo simulations and a good agreement found. The time distribution of events that were identified as muons before neutrino candidates was analysed and a new veto time window for muons introduced which decreases the dead time due to the veto to 3.9 % of the data taking time for the gadolinium and 4.7 % for the hydrogen analysis.
The stability of the scintillator in the Inner Detector and Inner Veto was studied by observing the temporal development of the position of two muon induced peaks in the charge spectra. A slight shift for both positions in the sub-percent level per year was determined. Changes in the gain of the used PMTs and temperature effects could be excluded.
Neutrons from muons are background to all liquid scintillator-based experiments. There-

fore a neutron simulations for the JUNO experiment were performed to find an optimal thickness of the surrounding water shielding. As result a cylindrical water shielding with a thickness of four to five meters is favoured.
During the writing of this thesis several changes on the far detector Inner Veto were performed. The time delay between Inner Veto and Inner Detector signals has been corrected and the amplification of the signals has been changed. The latter leads to new calibration constants. They can be determine in future by applying the methods developed in this thesis.
The near detector is currently in its commissioning phase and data taking will start soon. The same study presented in this thesis for the far detectors Inner Veto can be applied to the new veto as well and performance the introduced changes be determined.
The results of the JUNO neutron simulation need to be confirmed with the JUNO simulation package developed in the meanwhile.

A

Drawings of the near Inner Veto

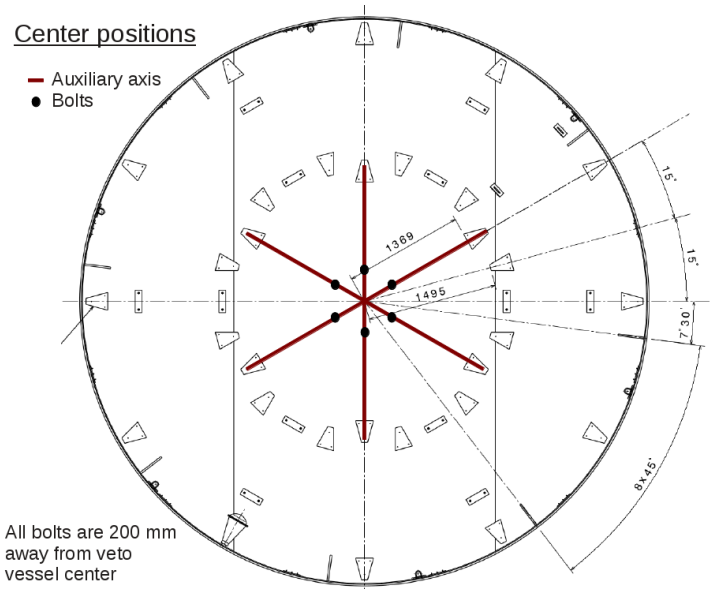

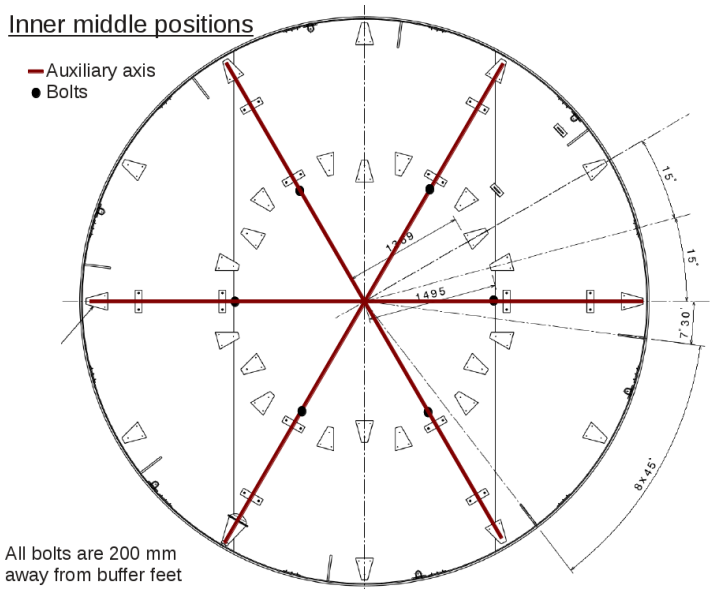
Inner middle positions
Auxiliary axis
Bolts
1369
1495
15'
15'
7'30'
8x45'
All bolts are 200 mm
away from buffer feet

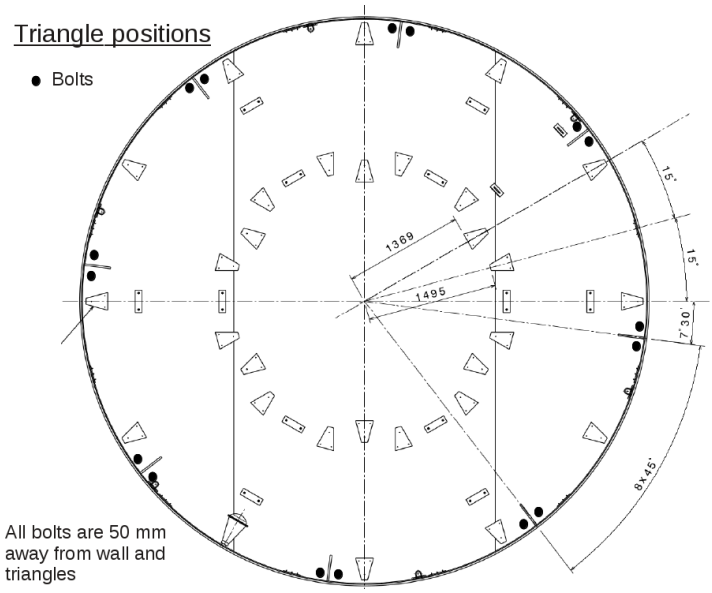
Triangle positions
Bolts
1369
1495
15'
15'
7'30'
8x45'
All bolts are 50 mm
away from wall and
triangles

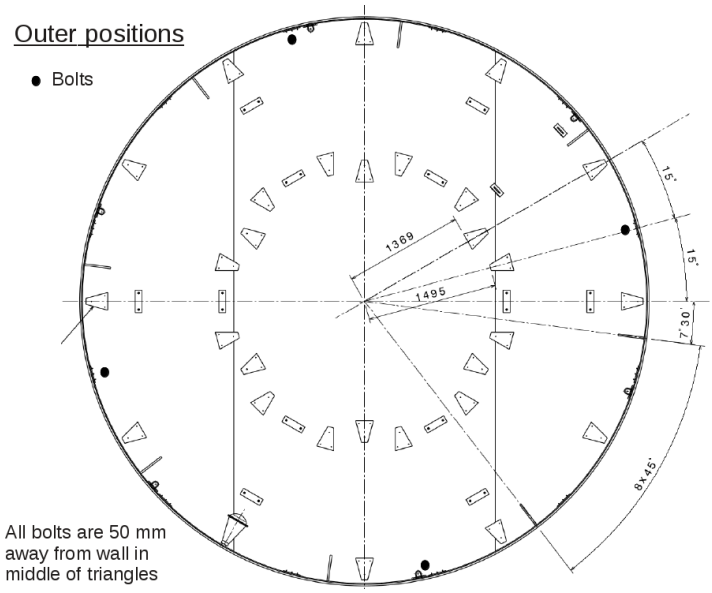
Outer positions
Bolts
1369
1495
15'
15'
7'30'
8x45'
All bolts are 50 mm away from wall in middle of triangles

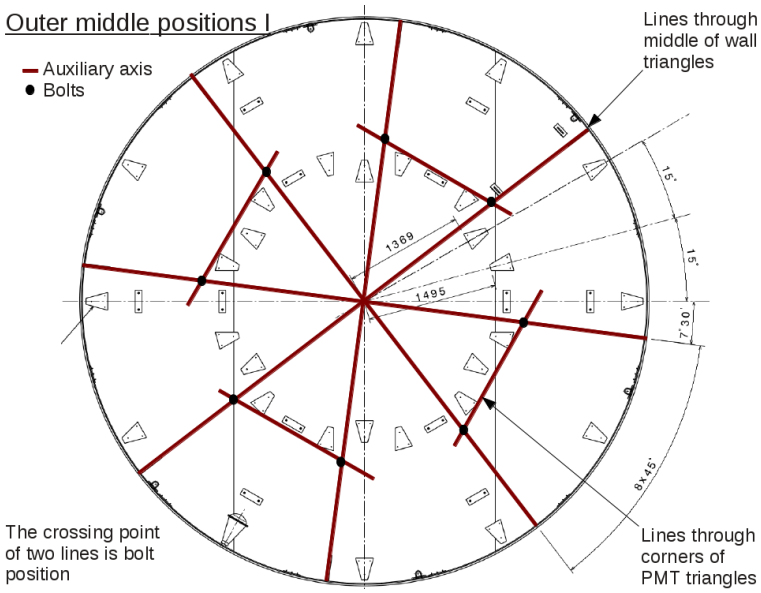
Outer middle positions I
Auxiliary axis
Bolts
Lines through middle of wall triangles
1369
1495
15'
15'
7'30'
8x45'
The crossing point of two lines is bolt position
Lines through corners of PMT triangles

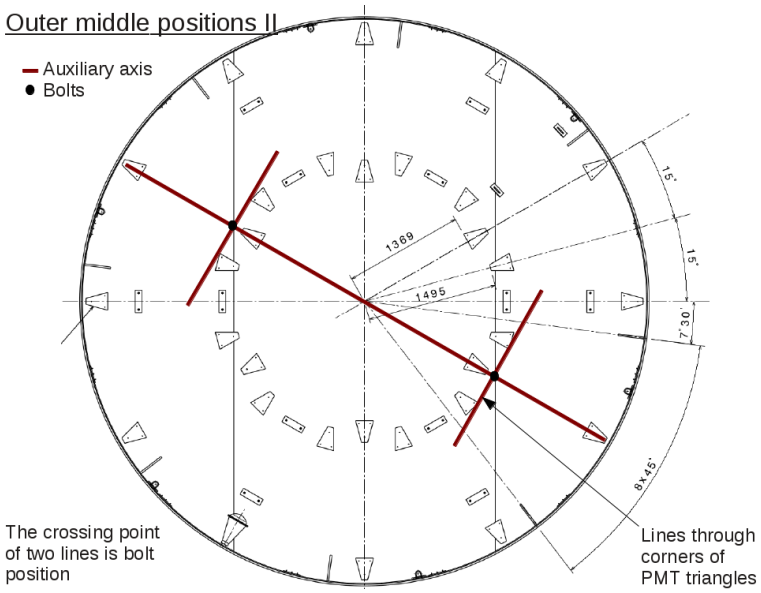
Outer middle positions II
Auxiliary axis
Bolts
1369
1495
15'
15'
7'30'
8x45'
The crossing point of two lines is bolt position
Lines through corners of PMT triangles

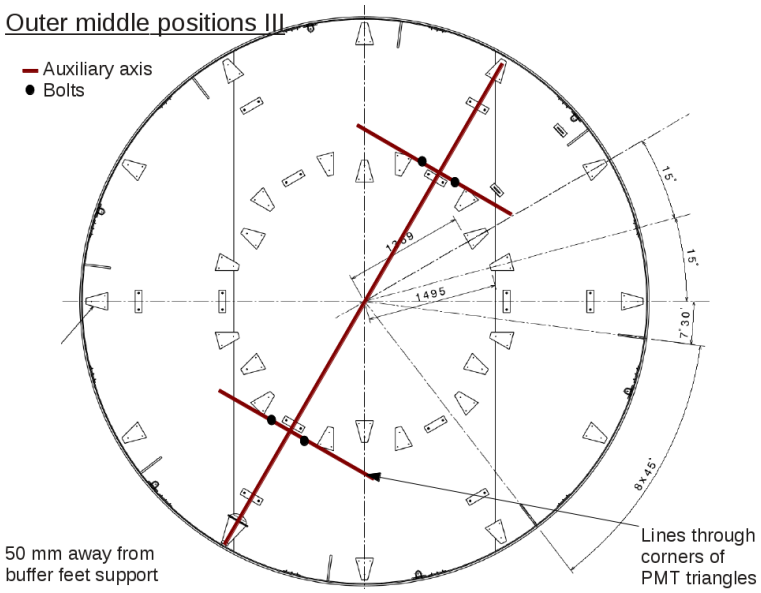
Outer middle positions III
Auxiliary axis
Bolts
1369
1495
15'
15'
7'30'
8x45'
50 mm away from buffer feet support
Lines through corners of PMT triangles

Wall positions

in φ: Just in middle of PMT positions

in z: 50 mm distance to bottom and top, rest equally distributed (~1120 mm distance between bolts)

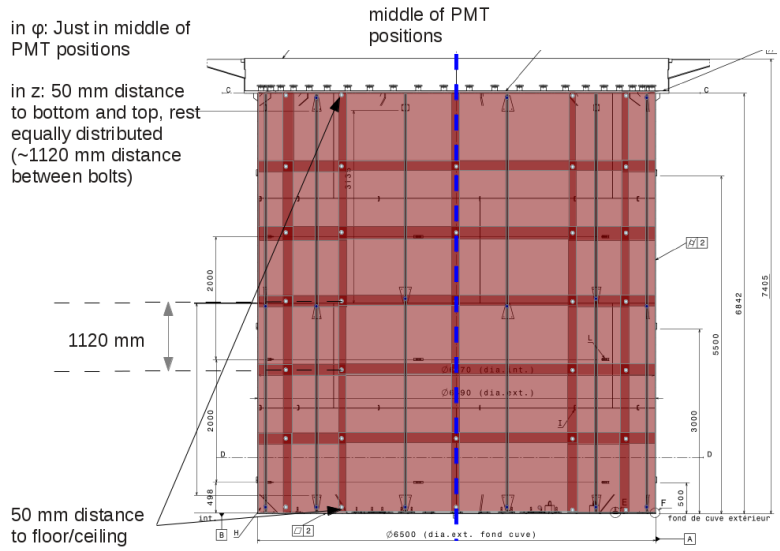

Acknowledgment / Danksagung

Acknowledgment

First of all I want to thank the Double Chooz collaboration for the opportunity to be part of it. It was a pleasure and I enjoyed the multicultural work.
A special thanks is going to Patrick Perrin, Olivier Corpace, Hervé de Kerret, Christian Veyssiere and Emmanuel Chauveau for their help during the installation of the two Inner Vetos and the replacement of the far Inner Veto PMTs. I want to thank Alain and Maurice as well for their assistance during the planing of the bolt positions for the VM 2000 mounting.
Thanks also to Bayarto Lubsandorzhiev for his fruitful advices and Marta Meloni Meloni and Nima Lubsandorzhiev for their support during the near IV installation.

Danksagung

Zuerst möchte ich mich bei Tobias Lachenmaier und Josef Jochum bedanken für die Möglichkeit an ihrem Lehrstuhl die Arbeit zu schreiben und das in mich gesetzte Vertrauen.
Ein besonderer Dank gilt natürlich auch meiner Familie, die mich auf all meinen Wegen immer unterstützt hat und so all dies überhaupt möglich gemacht hat.
Meinem ehemaligen Lehrer Peter Strakeljahn möchte ich auch meinen Dank aussprechen. Er hat mich für die Physik begeistert und ohne ihn hätte ich wohl nicht Physik studiert.
Als ich 2008 nach Tübingen gekommen bin, wurde ich sehr herzlich aufgenommen und schnell integriert. Aus vielen (ehemaligen) Kollegen sind gute Freunde geworden. Deshalb mein Dank an die Arbeitsgruppe, also Michael Bauer, Büsra Cebeci, Paula Denner, Gerhard Deuter, Sebastian Diebold, Dennis Dietrich, Raphael Falkenstein, Kai Freund, Eduard Friske, Daniel Greiner, Elena Großmann, Michael Gschwender, Andrea Hagen, Alexander Hegai, Tobias Jammer, Marcel Kimmerle, Markus Knapp, Jurek Loebell, Georg Meierhofer, Marc Pfeiffer, Florian Ritter, Klemens Rottler, Christof Sailer, Christopher Schmidt, Rainer Schmidt, Stephan Scholl, Ann-Kathrin Schütz, Lee Stokes, Christian Strandhagen, Katharina von Sturm, Alexander Tietzsch, Lisa Tomm, Martin Uffinger, Igor Usherov-Marshak, Oliver Wandel, Michael Wurm, Josef Jochum, Tobias Lachenmaier, Peter Grabmayr, Torsten Hehl, Heinz Clement, Gerhard Wagner, Günter Lang, Annette Pricking, Mikhail Bashkanov, Tatjana Skorodko, Anton Lymanets, Evgeny Lavrik, Jens Wiechula, Benjamin Hess, sowie den beiden Sekretärinnen Gaby Behring und Sonja Hierlemann.

Letzteren beiden und Brunhilde Eiskant, Anja Walz und Günter Lang auch vielen Dank für das Erledigen der vielen Verwaltungsaufgaben, die mit der Arbeit einhergingen.
Ebenso möchte ich Arthur Erhardt, Marcel Kimmerle und Roland Speith für ihre Hilfe bei den Computerfragen danken.
Ein besonderer Dank gilt Daniel Greiner, ich habe sehr viel von ihm lernen können und schätze seinen Rat sehr.
Während der Anfertigung dieser Arbeit sind viele größere und kleinere Aufgaben zu leisten gewesen. Dabei habe ich immer auf die Hilfe aus der Arbeitsgruppe bauen können. Hervorheben möchte ich:
Die Helfer beim Einbau des nahen Detektors in Chooz: Stefan Schoppmann, Ilya Bekmann, Michael Sorin, Alexander Tietzsch, Lees Stokes, Michael Wurm, Tobias Lachenmaier, Martin Uffinger, Kai Freund, Christopher Schmidt, Philip Reiber, Dominic Mache, Alexander Hegai, Susanne Kaska, Jurek Loebell und Paula Denner.
Die Helfer beim Einkapseln der PMTs: Andreas Zimmermann, Felix Blendinger, Manuela Linke, Elias Iwotschkin, Simon Weimer, Christoph Wenzel, Stephan Riedel, Matthias Riedel, Eduard Friske, Jenny Bayer, Martin Schmidt und natürlich Dennis Dietrich, Daniel Greiner und Lee Stokes.
Die Helfer beim Einbau des fernen Detektors und Austausch der PMTs: Daniel Greiner, Andrea & Norbert Hagen, Markus Knapp, Florian Ritter, Rainer Schmidt, Dennis Dietrich und Claudia Greiner.
Unsere Werkstätten für die rasche und sehr gute Erledigung der mitunter nicht angenehmen, aber leider notwendigen Arbeiten.
Den Korrekturleser dieser Arbeit: Martin Uffinger Christof Sailer, Kai Freund, Christopher Schmidt und Raphael Falkenstein.
Nicht vergessen möchte ich Benjamin Grämlich vom MPIK aus Heidelberg, der die Messungen am UVVis-Spektrometer vorgenommen hat.
Dank auch an meine alte Arbeitsgruppe in Hamburg, wo ich meine Diplomarbeit geschrieben habe.
Sehr dankbar bin ich auch unserer DSA-Spielegruppe um Claudia und Daniel Greiner, Annette und Sebastian Pricking, Gerhard Deuter und Markus Knapp, die mich in die Welt von Dere aufgenommen haben und mit denen ich nun schon oft ebendiese retten durfte.
Viel Freude bereitet mir auch die dienstägliche Quizrunde, wenn ich mit Pia Lachenmaier, Florian Ritter, Büsra Cebeci, Annika Schönsiegel, Stephan Scholl, Roland Speith, Michael Wurm und gelegentlichen Gästen neuen Fragen stellen kann.
Zuletzt möchte ich noch meinen Freunden aus der Schulzeit und der Zeit in Hamburg danken. Auch wenn man sich lange nicht mehr gesehen hat, so ist man doch immer wieder so vertraut, als hätte man sich erst gestern das letzte Mal getroffen.

B
List of abbreviations

B	
BisMSB	1,4-Bis(2-methylstyryl)benzene
BKG	Background
C	
CKM	Cabibbo, Kobayashi, Maskawa
D	
DAQ	Data Acquisition system
DC	Double Chooz
DSNB	Diffuse Supernova Neutrino Background
F	
FADC	Flash Analog to Digital Converter
FD	Far Detector
H	
HV	High Voltage

I	
IBD	Inverse Beta Decay
ID	Inner Detector
IV	Inner Veto
J	
JUNO	Jiangmen Underground Neutrino Observatory
L	
LAB	Linear Alkylbenzene
LAND	Liquid scintillator anti neutrino detector
LENA	Low Energy Neutrino Astronomy
LEP	Large Electron Positron collider
LHC	Large Hadron Collider
M	
MC	Monte Carlo
mwe	meter water equivalent
N	
ND	Near Detector
P	
PE	Photo Electron
PMNS	Pontecorvo, Maki, Nakagawa, Sakata
PMT	Photo Multiplier Tube
PPO	2,5-Diphenyloxazole
PTFE	Polytetrafluoroethylene
O	
OV	Outer Veto
S	
SM	Standard Model of particle physics

List of Figures

List of Tables

Bibliography

[Aba12] K. N. Abazajian, M. A. Acero, S. K. Agarwalla, A. A. Aguilar-Arevalo, C. H. Albright, S. Antusch, C. A. Arguelles and A. B. Balantekin *et al.*, "Light Sterile Neutrinos: A White Paper", arXiv:1204.5379 [hep-ph]

[Atl12] ATLAS Collaboration: "Combined search for the Standard Model Higgs boson using up to 4.9 fb^{-1} of pp collision data at $\sqrt{s} = 7$ TeV with the ATLAS detector at the LHC", Phys. Lett. B **710** (2012) 49 [arXiv:1202.1408 [hep-ex]]

[Bal95] Baldini, et all: Geology at the CHOOZ site. 1995. – CHOOZ collaboration internal report, preliminary partial data

[Cad13] E. Caden, V. Fischer, R. Roncin: "Neutrino directionality measurement", DocDB 5212 (2013) `http://www.dchooz.org/DocDB/cgi-bin/private/ShowDocument?docid=5212` (password secured)

[Cah13] R. N. Cahn, et al: "White Paper: Measuring the Neutrino Mass Hierarchy", arXiv:1307.5487 [hep-ex] (2013)

[Cho98] CHOOZ Collaboration: "Initial results from the CHOOZ long baseline reactor neutrino oscillation experiment", Phys. Lett. B **420** (1998) 397 [hep-ex/9711002]

[Cho03] Chooz Collaboration: "Search for neutrino oscillations on a long base-line at the CHOOZ nuclear power station", Eur. Phys. J. C **27** (2003) 331 [hep-ex/0301017]

[CMS12] CMS Collaboration: "Combined results of searches for the standard model Higgs boson in pp collisions at $\sqrt{s} = 7$ TeV", Phys. Lett. B **710** (2012) 26 [arXiv:1202.1488 [hep-ex]]

[Cow56] C. L. Cowan Jr., F. Reines, F. B. Harrison, H. W. Kruse und A. D. McGuire: "Detection of the Free Neutrino: A Confirmation", Science 124, 103 (1956)

[DAY12] DAYA-BAY Collaboration: "Observation of electron-antineutrino disappearance at Daya Bay", Phys. Rev. Lett. **108** (2012) 171803 [arXiv:1203.1669 [hep-ex]]

[DBE] `http://www.lemro.de/en/products/solvents.html?detail=46`, last visited 1.3.2015

[DCC04] Double Chooz Collaboration: "Letter of Intent for Double-CHOOZ: a Search for the Mixing Angle Theta13", hep-ex/0405032 (2004)

[DCC11] Double Chooz Collaboration: "Indication for the disappearance of reactor electron antineutrinos in the Double Chooz experiment", Phys. Rev. Lett. **108** (2012) 131801 [arXiv:1112.6353 [hep-ex]]

[DCC12] Double Chooz Collaboration: "Reactor electron antineutrino disappearance in the Double Chooz experiment",Phys. Rev. D **86** (2012) 052008 [arXiv:1207.6632 [hep-ex]].

[DCC13] Double Chooz Collaboration: "First Measurement of θ_{13} from Delayed Neutron Capture on Hydrogen in the Double Chooz Experiment", Phys. Lett. B **723** (2013) 66 [arXiv:1301.2948 [hep-ex]]

[DCC14] Double Chooz Collaboration: "Improved measurements of the neutrino mixing angle θ_{13} with the Double Chooz detector", JHEP **1410** (2014) 86 [arXiv:1406.7763 [hep-ex]]

[DCM14] Double Chooz Collaboration: "Precision Muon Reconstruction in Double Chooz", Nuclear Inst. and Methods in Physics Research, A (2014), pp. 330-339 [arXiv:1405.6227 [physics.ins-det]]

[DCMu] Double Chooz Collaboration: "Muons in Double Chooz" to be published

[Die12] D. Dietrich, D. Greiner, J. Jochum, T. Lachenmaier, M. Röhling and L. Stokes: "Monte Carlo aided design of the inner muon veto detectors for the Double Chooz experiment", JINST **7** (2012) P08012 [arXiv:1207.1623].

[Die13] D. Dietrich: "Studying the muon background component in the Double Chooz experiment", PhD thesis, Universität Tübingen, 2013

[Don00] DONUT collaboration: "Observation of tau neutrino interactions", Phys. Lett. B **504** (2001) 218 [hep-ex/0012035]

[D0] `http://www-d0.fnal.gov/public/pubs/topmass_prl_sum.html`, last visited 1.3.2015

[Gai04] T. K. Gaisser and T. Stanev, "Cosmic Rays:" Review of Particle Physics, edited by L. Alvarez-Gaumé et al., Physics Letters, B592, 228 (2004).

[GPL] `http://geant4.cern.ch/support/proc_mod_catalog/physics_lists/referencePL.shtml`, last visited 1.3.2015

[Gra13] M. Grassi: "Detector Design Status", internal JUNO talk, given in December 2013

[Gre14] D. Greiner: "Design und Aufbau des Double Chooz Myon-Vetos", PhD thesis, Universität Tübingen, 2014

[Goo06] M. Goodman, T. Lasserre: "Double-CHOOZ: A Search for the Mixing Angle Theta13", hep-ex/0606025 v4 (2006)

[He13] M. He: "Future Reactor Experiments", arXiv:1310.7343 (2013)

[IMB] R. M. Bionta et al.: "Angular distribution of events from SN1987A", Physical Review D37 3361(1988)

[Kam08] KamLAND Collaboration: "Precision Measurement of Neutrino Oscillation Parameters with KamLAND", Phys. Rev. Lett. 100, 221803 (2008) [arXiv:0801.4589 [hep-ex]]

[KamL] `http://kamland.lbl.gov/Pictures/pictures/KamLAND-detector-ill.jpg`, last visited 1.3.2015

[Kna09] M. Knapp: "Design, Simulation und Aufbau des GERDA-Myonvetos", PhD thesis, Universität Tübingen, 2009

[Kud08] V. A. Kudryavtsev: "Muon simulation codes MUSIC and MUSUN for underground physics", Comput. Phys. Commun. 180 (2009), p. 339–346 [arXiv:0810.4635]

[LEP05] The ALEPH, DELPHI, L3, OPAL, SLD Collaborations: "Precision Electroweak Measurements on the Z Resonance" Phys. Rept. **427** (2006) 257 [hep-ex/0509008]

[Möl13] R. Möllenberg: "Monte Carlo Study of Solar ^{8}B Neutrinos and the Diffuse Supernova Neutrino Background in LENA", PhD thesis, Technische Universität München, 2013

[Mül11] T. A. Müller, D. Lhuillier, M. Fallot, A. Letourneau, S. Cormon, M. Fechner, L. Giot and T. Lasserre *et al.*: "Improved Predictions of Reactor Antineutrino Spectra", Phys. Rev. C **83** (2011) 054615 [arXiv:1101.2663 [hep-ex]]

[PDG12] Particle Data Group: "Particle Physics Booklet" 2012

[Pau77] W. Pauli: "Fünf Arbeiten zum Ausschließungsprinzip und zum Neutrino" Texte zur Forschung Vol. 27 (Wissenschaftliche Buchgesellschaft Darmstadt, 1977)

[Pen14] J. Peng: "Daya Bay: Results and perspectives", talk given at the NOW conference 2014

[Pfa12] P. Pfahler: "Realization of the low background neutrino detector Double Chooz: From the development of a high-purity liquid & gas handling concept to first neutrino data", PhD thesis, Technische Universität München, 2012

[Rei09] B. Reinhold: "Development of a Level-1 Trigger and Timing System for the Double Chooz Neutrino Experiment", PhD thesis, RWTH Aachen, 2009

[Rem12] A. Remoto: "Correlated background and impact on the measurement of θ_{13} with the Double Chooz detector", PhD thesis, Nantes University, 2012

[Ren12] RENO Collaboration: "Observation of Reactor Electron Antineutrino Disappearance in the RENO Experiment", Phys. Rev. Lett. **108** (2012) 191802 [arXiv:1204.0626 [hep-ex]]

[ROOT] `root.cern.ch`, last visited 1.3.2015

[Tan06] A. Tang, G. Horton-Smith, V. A. Kudryavtsev and A. Tonazzo: "Muon simulations for Super-Kamiokande, KamLAND and CHOOZ", Phys. Rev. D **74** (2006) 053007 [hep-ph/0604078]

[Sch97] N. Schmitz: "Neutrinophysik", Teubner Stuttgart 1997

[Seo14] S.-H. Seo: "Results from RENO", talk given at the Neutrino 2014 conference

[Stü13] D. A. Stücken: "Estimation of the systematic uncertainties of the measurement of the neutrino mixing angle θ_{13} related to the trigger system of the Double Chooz Experiment", PhD thesis, RWTH Aachen, 2013

[Sup98] Super-Kamiokande Collaboration: "Evidence for oscillation of atmospheric neutrinos", Phys. Rev. Lett. **81** (1998) 1562 [hep-ex/9807003]

[Viv13] M. Vivier: "Double Chooz geodetic surve", `http://www.dchooz.org/DocDB/cgi-bin/private/ShowDocument?docid=4753` (password secured)

[Wur13] M. Wurm: "Status update on RecoMuHamID", DocDB 4578 (2014), `http://www.dchooz.org/DocDB/cgi-bin/private/ShowDocument?docid=4578` (password secured)

[Zub12] K. Zuber: "Neutrino Physics", Routledge Chapman & Hall, 2012